UNIVERSITÀ DEGLI STUDI DI PADOVA

Dipartimento di Ingegneria Industriale

Corso di Laurea Magistrale in Materials Engineering

Performance evaluation of handheld laser-based sensor: analysis of shutter-speed effects on different surface types

Relatrice:

Dott. Ric.
Sofia Catalucci

Laureando:

Matteo Moretto
Matricola: 2129683

Anno Accademico 2025/2026

Abstract

As handheld laser-based sensors are relatively recent there are no dedicated international standards for their performance evaluation at present. For this reason, to assess the performance of such sensors, manufacturers often refer to current ISO 10360-13:2021 for the acceptance and reverification tests of coordinate measuring systems (CMS), which is built on VDI/VDE 2634 part 3 now withdrawn. The proposed work presented in this thesis aims at addressing the challenges related to the evaluation of the metrological performances of handheld laser-based sensors when used in industrial conditions, more specifically when employed for the inspection of workpieces of varying material and surface finish. This thesis work has two main objectives:

(i) defining a rigorous protocol to evaluate the metrological performances of handheld laser scanners using the ISO 10360-13 framework as foundational reference and adapting this procedure to a Creaform HANDYScan 3D Silver handheld multi-line laser-based sensor;

(ii) investigating the effects of different shutter speed levels (i.e. a setting that can be controlled in the sensor’s software interface) when measuring both cooperative and non-cooperative materials. Using calibrated spheres as tests artefacts (e.g. matte and shiny metallic spheres), the instrument performance is quantified through key quality metrics, both metrological and point-based: probing errors (size and form), surface coverage, and point cloud density. The results show how the correct selection of shutter speed can improve measurement accuracy and data completeness.

This work provides valuable insight for a future standardization protocol for the performance verification of handheld laser scanners. In addition, it provides a practical framework for achieving highly accurate 3D inspections performed in challenging industrial environments.

Declaration of usage of generative AI and AI-assisted technologies

During the preparation of this thesis, the author used generative AI and AI-assisted tools to support the revision and linguistic refinement of the draft, ensuring grammatical accuracy and consistency of academic terminology in English. In addition, AI-assisted tools were consulted for assisting with scripts debugging for data processing. All outputs were critically reviewed, verified, and integrated by the candidate.

The author reviewed and edited the Thesis as needed and takes full responsibility for its content.

Table of Contents

Chapter 1: Background and Related Work

Handheld laser scanners are portable devices used for the acquisition of 3D geometry of an object simply by moving the instrument by hand around the surface to be measured. This is a relatively new technology, which has become increasingly widespread in industrial metrology in recent years due to its speed and versatility, useful especially in dimensional inspection processes for components with complex geometry or large dimensions. These sensors, despite their widespread use, still present limitations that impact their metrological reliability. Their performance depends heavily on operating conditions, such as the optical properties of the measured surface or the acquisition parameters set by the operator (e.g., shutter speed). Furthermore, there is currently no dedicated standard for evaluating the metrological performance of these scanners. This thesis aims at addressing this gap through normative adaptation, alongside a separate experimental study to optimize acquisition parameters across different surface types.

This chapter introduces the theoretical and normative background, foundation of the presented thesis. The first section presents the fundamental concepts of metrology, including measurement error, uncertainty, and traceability. The second section instead addresses the definition and classifications of Coordinate Measuring Systems (CMSs), focusing on optical CMSs, and further on the laser triangulation principle, as it is exploited by the Creaform HandySCAN 3D Silver sensor investigated in this work. The third section presents the influence of surface optical properties on measurement quality, distinguishing between cooperative and non-cooperative surfaces, an important distinction the shutter speed optimization objective of this project. The fourth section introduces the current normative framework for performance verification of CMSs, focusing specifically on the VDI/VDE 2634 part 3 [1] technical guidelines and on ISO 10360-13:2021 standard [2], whose adaptation to handheld laser-based sensors constitutes the methodological foundation of Chapter 2. Finally, the fifth section reviews the literature on handheld optical scanner performance, highlighting the research gap that motivates this work.

1.1 Metrology

Metrology is defined in the Vocabulary of International Metrology (VIM) [3] as the "science of measurement and its applications". This field encompasses the study of measurement units, measurement uncertainty, and the various techniques and technologies required to perform measurements; this framework provides the theoretical and practical infrastructure necessary to ensure the reliability and global comparability of results.

The VIM serves as the reference guidance document, which establishes a common, harmonized language for measurement science worldwide. It was produced and promoted by the Joint Committee for Guides in Metrology (JCGM), an organization made up of eight international bodies, including the International Bureau of Weights and Measures (BIPM) and the International Organization for Standardization (ISO). Within this document, the rigorous terminology described serves as the foundation of this study. Quantity is defined as "the property of a phenomenon, body, or substance, where the property has a magnitude that can be expressed as a number and a reference", while with measurement we indicate the "process of experimentally obtaining one or more quantity values that can reasonably be attributed to a quantity", known as the measurand.

The scope of metrology extends across all areas of measurement science related to the seven base quantities (i.e. length, mass, time, electric current, temperature, amount of substance, and luminous intensity) defined by the International System of Units (SI) [4] and the quantities derived from them.

Geometrical Metrology (or also called Industrial Metrology, Manufacturing Metrology) is the branch of metrology that focuses specifically on dimensions and shapes, and which can be in turn divided into two sub-branches:

- **Dimensional and Form Metrology:** it concerns the measurement of macroscopic dimensions (e.g. lengths, distances, diameters, angles) and the evaluation of form deviations from mathematically ideal shapes (assessing parameters such as planarity, cylindricity and circularity).
- **Surface Metrology:** it focuses on the micro-geometrical analysis of the surface topography of a part, particularly the analysis of surface texture.

1.1.1 Geometrical metrology in Industry

Historically, the primary focus of geometrical metrology was to verify product uniformity and ensure the interchangeability of manufactured parts and the product's conformity verification at the end of the production cycle [5,6]. However, with the advance of technologies, the advent of Industry 4.0 and digital manufacturing, its role has undergone a significant evolution, transforming metrology from a passive verification stage into a fundamental enabling technology that permits the development of modern advanced products (characterized by high-performance requirements, high complexity and miniaturization) which previously were not possible. In the context of digital manufacturing, it is not relegated anymore to an isolated operation but is now seamlessly integrated across multiple levels of the modern production line, connecting design, production and quality control (Figure 1).

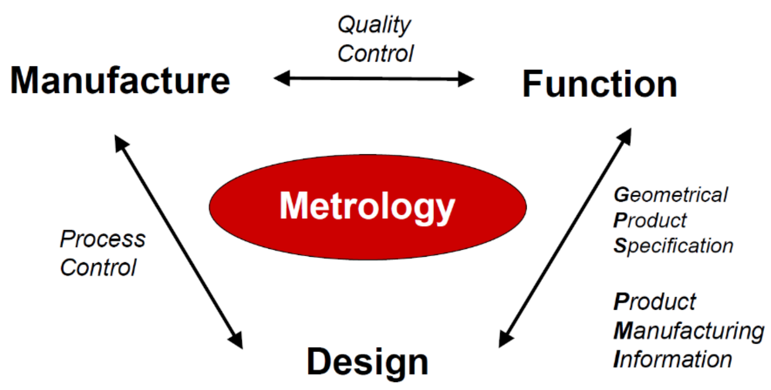

Figure 1. Synthetic scheme on the roles of metrology. Source: from [7]

In this landscape, it provides the decisional basis to control the design, optimize and develop manufacturing processes, and guarantee the overall performance of the final product, ultimately contributing to quality improvement and cost reduction.

The functions that metrology provides are:

1. **Quality Control of the Product:** It ensures that components comply with the Geometrical Product Specifications (GPS) defined during the design phase, guaranteeing both dimensional accuracy and operational functionality.
2. **Statistical Process Control (SPC):** Through continuous monitoring, it allows manufacturers to rapidly distinguish when the process is "under control", i.e. the measurements show normal process variability attributed just to random factors, and

when the process is "out of control" when a systematic drift is individuated (e.g. malfunctions, tools wear or breakage). This feedback enables the rapid implementation of corrective actions before defective parts are produced and allows the manufacturer also to improve and optimize the process reducing the number of scraps.

3. **Support to the design:** metrology creates a closed-loop system where measurement data iteratively feeds back into the engineering phase, allowing for the continuous optimization of product design and manufacturing parameters (Figure 2).
4. **Reverse Engineering:** It enables the reconstruction of a nominal 3D CAD model or the extraction of key geometrical information from a physical component. It is useful when design data are unavailable, incomplete, or need to be updated.

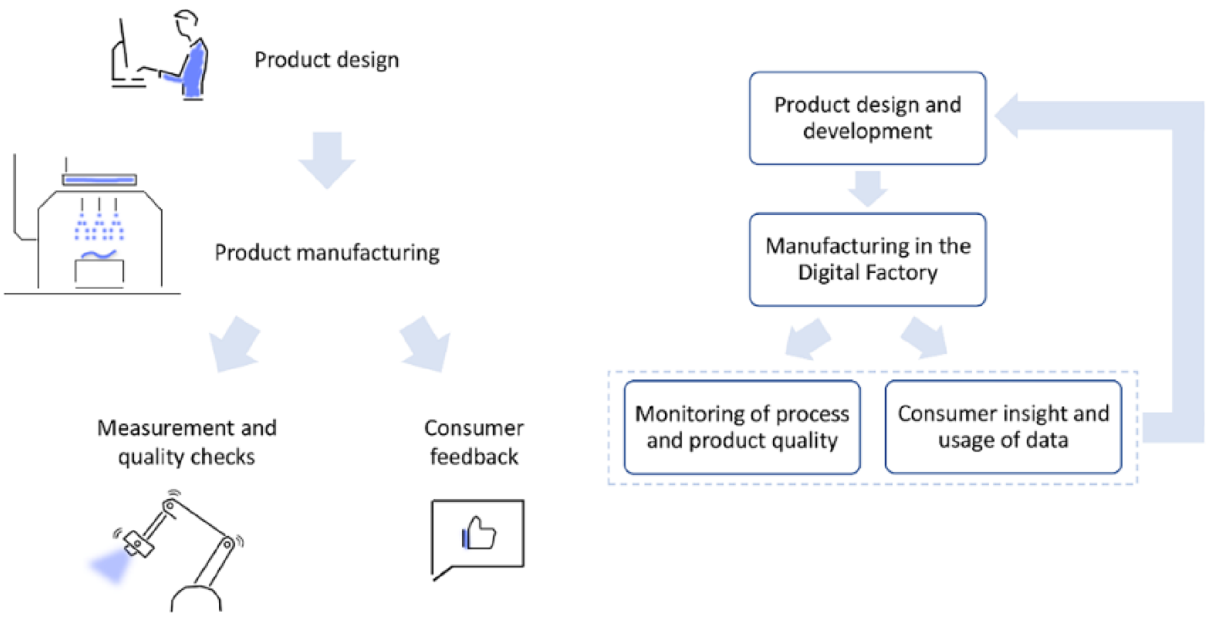

Figure 2. Enhancing of a product design thanks to the feedback of consumers and measurements or quality checks. Source: from [5]

The strength of Industry 4.0 revolution lies in the synergy between digitalization and connectivity; the transition to digital measuring systems allows the process to continuously collect data and share them throughout the different stages of production. In this environment data is turned into usable information to promote fast and reliable actions towards the ultimate goal of zero-defects manufacturing, in which every measurement actively contributes to the correction of the production process.

These needs are driving the development and deployment of "smart measuring systems", i.e. measuring solutions that are capable of operating automatically and consequently applying correction mechanisms based on the available data enhancing the overall speed, flexibility and reliability [8]. They can be broadly divided into two categories:

- **Smart Instruments:** these are measurement devices that allow a more efficient and complete acquisition of data, such as real-time monitoring devices, multi-sensor data fusion systems, multi-view measuring instruments and on-machine measurement solutions;
- **Smart Tools:** these are algorithmic or software components which leverage advanced technologies such as Artificial Intelligence (AI), Machine Learning (ML) and Digital Twins (DT) to better control and optimize measurement processes.

The foundation of these advanced systems is the implementation of knowledge-driven solutions; these utilize a priori information, such as 3D CAD models or historical production data, to autonomously optimize the measurement strategy.

1.1.2 Measurement Errors and Uncertainty

A fundamental starting point in metrology is the concept of measurement error, which quantifies the difference between the measured result (M) and the true value (R) of the quantity being measured.

$$E = M - R \tag{1}$$

The errors in a measurement can be attributed to various sources, such as the instrument, the environment, the workpiece that is subjected to measurement or the procedure. They can be classified based on the effects that they have on repeated measurements:

- **Systematic errors:** consistent and repeatable errors that result in a shift of the measured result (set of measurements) from the true value. They can be corrected by the calibration process, but they cannot be individuated from the measurement of an unknown sample.
  Sources: instruments, procedures, operators.
- **Random errors:** caused by non-controlled random influence quantities. They may be characterized by the standard deviation and the type of distribution. The mean value of the distribution is often considered as a basis for the evaluation of systematic errors.

They cannot be eliminated/corrected, but they can be easily individuated from repeated measurements.

Sources: mechanical, thermal, or electrical fluctuations, resolution.

The true value of a measurand, defined in the VIM as "the quantity to be measured", is a hypothetical result and it is intrinsically unknowable, so the error can never be determined with absolute certainty. This reason led to the definition of measurement uncertainty. The result of a measurement is always to be associated with an uncertainty and confidence level. The measurement uncertainty is described in the VIM as a "non-negative parameter characterizing the dispersion of the quantity values being attributed to a measurand, based on the information used" or in other terms is the quantification of the doubt of any measurement, it can never be eliminated but it can be reduced by reducing the sources of errors. The confidence level instead refers to the probability that the real value lies in the uncertainty range.

All the measurements results should be indicated as follows:

$$y \pm (k \times u_c) = y \pm U \tag{2}$$

in which y represents the measured value, u_c is the combined standard uncertainty, k is the coverage factor corresponding to a specific confidence level (as reported in Table 1) and U is the expanded uncertainty.

Confidence level / %	**Coverage Factor**
68.3	1
90	1.645
95	1.960
95.5	2
99	2.576
99.7	3

Table 1. Confidence levels and their relative coverage factors

The evaluation of the measuring uncertainty is described in the "G*uide to the expression of Uncertainty in Measurement*" (GUM) [9], but it can be also carried out through other simpler and less rigorous approaches such as the "*Procedure for Uncertainty Management*" (PUMA) described in the ISO 14253-3:2011 [10] and the "*Comparator method*" described in the ISO 15530-3:2011 [11], and the Monte Carlo method described in the ISO/TS 15530-4:2008 [12].

1.1.3 Metrological Traceability

A measurement result is only meaningful if it can be related to establish references; this concept is described in the VIM as **traceability** and which is defined as "property of a measurement result whereby the result can be related to a reference through a documented unbroken chain of calibrations, each contributing to the measurement uncertainty"; that chain of standards is also referred to as traceability chain. In practical terms, this means that every measurement performed in an industrial or laboratory context must be traceable back to internationally recognised units of measurement (Si units) maintained by primary national and international metrology institutes, such as the Bureau International des Poids et Mesures (BIPM) and national bodies including PTB (Germany), NPL (United Kingdom), and INRIM (Italy). The standards in the traceability chain are organized in a hierarchical structure called standard pyramid (Figure 3).

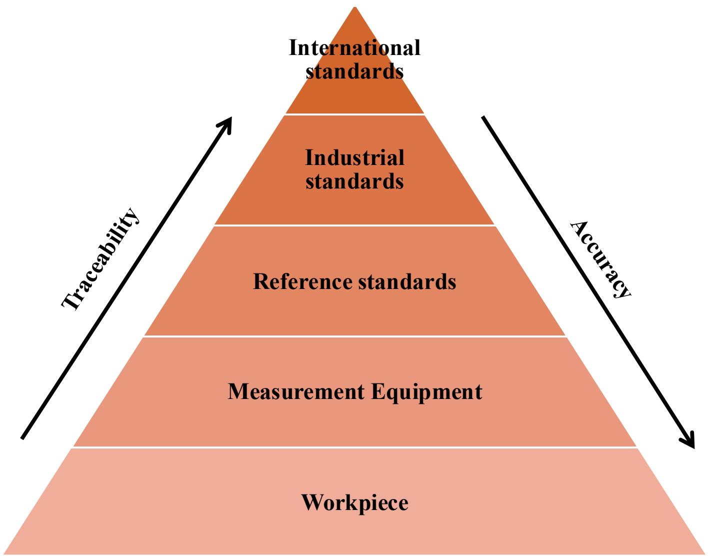

Figure 3. Calibration hierarchy or traceability pyramid

The practical mechanism through which traceability is established and maintained is calibration, defined in the VIM as the "operation that, under specified conditions, in a first step, establishes a relation between the quantity values with measurement uncertainties provided by measurement standards and corresponding indications with associated measurement uncertainties and, in a second step, uses this information to establish a relation for obtaining a measurement result from an indication"; in other terms it is the process that quantifies the relationship between the measuring results of an instrument and the true value of the measurand as a calibrated artefact with known uncertainty is used.

1.2 Coordinate Measuring System

In Geometrical Metrology several types of measuring instruments are deployed, and a continuous work of research and development is being carried on new solutions to improve even more the accuracy, the reliability and flexibility of these instruments.

Coordinate Measuring Systems (CMSs) are those devices capable of acquiring the spatial coordinates of points belonging to the surface of the measured workpiece, with the creation of a digital point cloud (PC), a mathematical representation of the real object that can be processed through dedicated software for the compliance verifications of the Geometrical Product Specifications (GPSs). The primary function of these systems is to measure the actual physical geometry of a workpiece. By comparing the acquired coordinates with the nominal CAD (Computer-Aided Design) model, CMSs evaluate fundamental metrological information such as position, form, dimensions, and orientation, that would otherwise be impossible to evaluate using manual methods.

Coordinate measuring systems can be classified according to several criteria; the most relevant classification divides the CMSs based on the data acquisition principle as shown in Figure 4. A fundamental distinction is made between Contact and Non-Contact instruments.

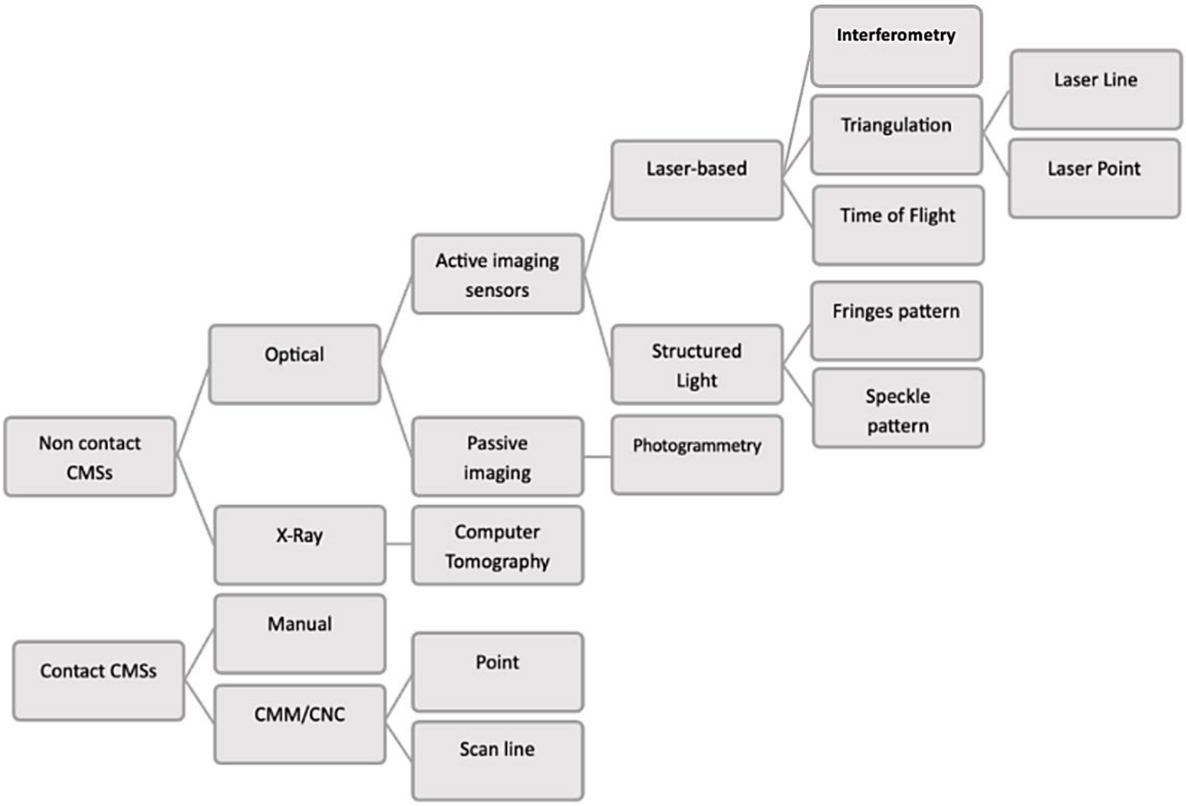

Figure 4. Classification of Coordinate Measuring Systems (CMSs) based on the acquisition principle

1.2.1 Contact-based coordinate measuring systems

Historically, Contact CMSs are the first to have been developed and integrated in the manufacturing industry; while the market for non-contact systems is growing rapidly, contact-based Coordinate Measuring Machines (CMMs) remain the "gold standard" in metrology due to their unmatched accuracy and low measurement uncertainty, which can reach sub-micron levels. The measuring principle of these types of instruments is simply the physical contact of a touch probe and the surface of the measured workpiece. Measurements can be carried out either by point-by-point acquisition or by scan mode with which the touch probe is made run over the surface. Despite their precision, these systems are relatively slow and may be unsuitable for measuring soft or delicate components that could be deformed or damaged by the probes contact force.

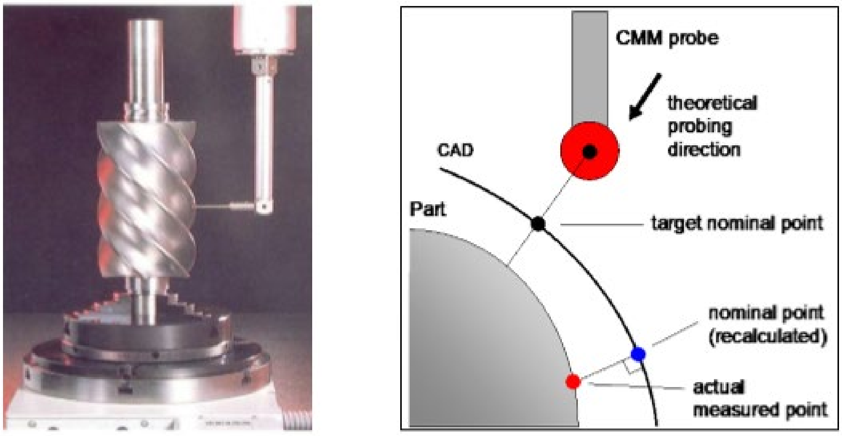

Figure 5. Physical principle of a Contact Coordinate Measuring Machine (CMM). Source: from [7].

1.2.2 Optical coordinate measuring systems

On the other hand, non-contact CMSs primarily utilize optical sensors to acquire the point coordinates from the interaction of the workpiece with the electromagnetic radiation. Their increasing adoption in factory floors and metrology labs is driven by their high acquisition speed, large measurement volumes, flexibility, and the ability to capture millions of points in a few seconds. This makes them ideal for in-line measurements, inspecting complex free-form geometries and fragile or soft materials. However, the measurement of hollow or complex geometries remains challenging for both contact and optical systems, due to limited accessibility for the probe or the line-of-sight. All these qualities come at the expense of higher measurement uncertainty compared to tactile systems; the interaction of the light with the workpiece is inherently complex and it introduces a significantly higher number of error sources. Furthermore, the performance of optical CMSs is strongly influenced by the optical properties of the surface, such as texture, reflectivity, glossiness, transparency, and colour.

Within the category of optical CMSs, further classifications can be made, either based on the coordinate determination principle, light source or on the dimensionality of measurements.

Classification by light source [13]:

- **Passive Optical CMSs:** these instruments rely on environmental light and heavy imaging processing. In this category there are the photogrammetry methods, which use heavy image processing to calculate the coordinates.

- **Active Optical CMSs:** these systems project a controlled light onto the workpiece, such as laser or a pattern (e.g. fringes or speckle). The source of light adds information onto the analysed surface, which is used by optical sensors to create the 3D scan. These techniques are generally faster and avoid some difficulties of photogrammetry (e.g. the need of scaling information and surface features for the triangulation).

Classification by measuring principle:

- **Triangulation:** it is based on the triangular geometrical relationship that permits the calculation of the distance of a measured point from the baseline defined by two sensors or a sensor and a light emitter which form a triangle. This is the measuring principle used in photogrammetry, structured light CMSs, and laser triangulation sensors.
- **Time-of-Flight (ToF):** These sensors measure the time elapsed between the emission of a laser pulse and its detection after reflection. Given the constant speed of light, the distance is derived. They are ideal for large-scale measurements (structures and geographic features) but typically offer low accuracy and low spatial resolution.
- **Interferometry:** This principle exploits the wave nature of light, measuring the phase shift between a reference beam and the beam reflected from the surface. It provides sub-micrometric accuracy; it is primarily used for surface texture and for laser-tracers or laser-trackers.

Classification by measurement dimensionality:

- **1D techniques (Point sensors):** these acquire coordinates point-by-point. To reconstruct a 3D surface, the sensor must be moved along at least two external degrees of freedom (e.g., on a CMM bridge).
- **2D techniques (Line Scanners):** these instruments project a laser line and acquire a 2D profile. A 3D scan requires at least one external axis of movement (mechanical or manual) to sweep the line across the part.
- **3D Techniques (Area scanners):** these can acquire a full point cloud of a specific area in a single shot (e.g. fringe projection) without the strict requirement of relative motion between the instrument and the workpiece during the measurement.

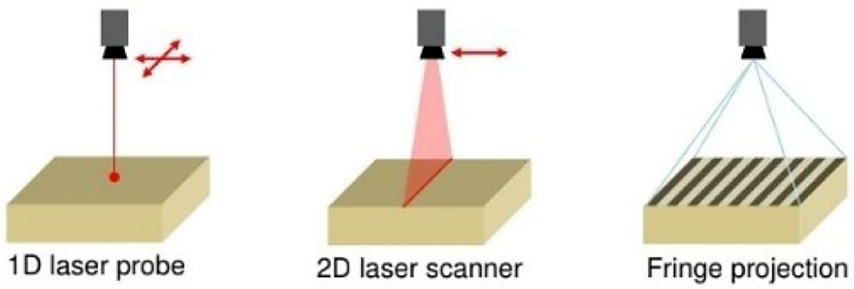

Figure 6. Classification of optical distance sensors and examples of 1D, 2D and 3D sensors. Source: from [7].

As it is key in this research, a brief description of the laser triangulation principle and handheld laser-based sensors is included in the following sections.

1.2.3 Laser Triangulation Sensors

As introduced previously, the active triangulation principle used in 3D laser scanners is a fast and reliable method widely applied in optical metrology. As detailed in the third chapter of *Advances in Optical Form and Coordinate Metrology* [14], this principle is based on solving the geometric triangles formed by the laser source, the optical sensor (usually a CCD or CMOS sensor) and the projected laser point (or line of points) onto the target surface. The distance between the laser emitter and the camera is fixed and known, defining the so-called "baseline". A laser emitter (Light Amplification by Stimulated Emission of Radiation) is a device that emits an electromagnetic beam with unique properties, fundamentally classified into monochromaticity, temporal and spatial coherence, and high directionality (collimation).

There exist various types of laser emitters which differ in the type of active medium used. In optical metrology, laser diodes [15] are employed due to their small dimensions, reliability and low cost. Laser diodes are produced in different colours depending on the materials used in the device (semiconductor and doping agent). The choice of the laser diode colour in a LT sensor can affect the measurement quality as a function of the target surface.

In 1D Laser Triangulation (LT) Sensors, a single laser point is projected onto the object of coordinates (x, z); its diffusely reflected light is then captured by the sensor at an observation angle that varies strictly according to the objects depth . Referring to Figure 7, the following geometrical relationship between the lateral coordinate x and the depth z can be established:

$$x = (z_0 - z) \tan \beta \tag{3}$$

Where β is the triangulation angle between the observation axis and the laser beam, z_0 is the reference depth where their intersection is represented by point O. Assuming the central projection model, another relationship that correlates x and z can be defined considering the lens and the sensor:

$$x = \frac{u}{f_x} \cdot z \tag{4}$$

where u represents the peak position of the detected laser on the sensor, and f_x is the focal length scaled to the detectors pixel unit. The latter can be described as $f_x = f \cdot s_x$, where f is the metric focal length and s_x is the number of pixels per unit length (pixel density) of the detector. Solving Equations (3) and (4) simultaneously yields the coordinates x and z of the measured point:

$$\begin{bmatrix} x \\ z \end{bmatrix} = \begin{bmatrix} \dfrac{u \cdot \tan \beta \cdot z_0}{f_x \cdot \tan \beta + u} \\ \dfrac{f_x \cdot \tan \beta \cdot z_0}{f_x \cdot \tan \beta + u} \end{bmatrix} \tag{5}$$

This equation can be written also in function of the baseline length b, considering the geometrical equation $b = z_0 \tan \beta$.

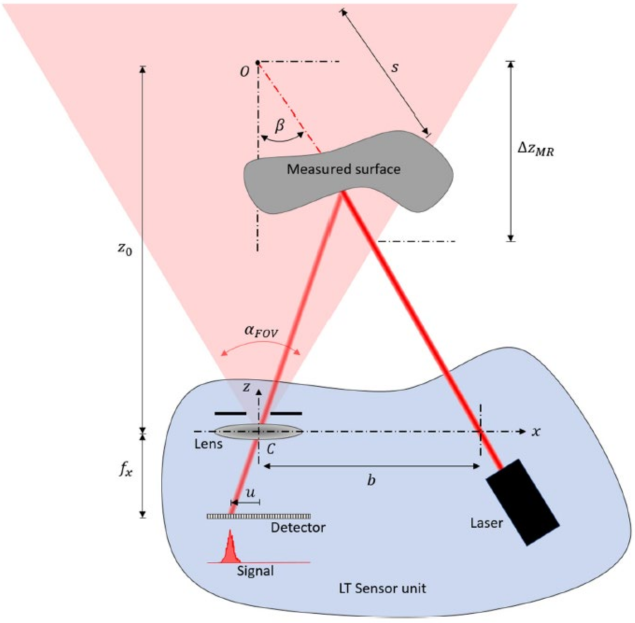

Figure 7. Schematic of Point LT sensor. Source: from [14]

Point LT sensors can be effectively extended to perform 2D profile measurements by substituting the standard laser dot with a continuous laser line, which is typically generated either by projecting the laser beam through a special lens (such as a cylindrical or a Powel lens) or by employing high-speed oscillating mirrors.

The spatial coordinates of the laser profile on the surface can be determined through a mathematical approach similar to the one previously described integrating a new expression for y, as shown in Figure 8. To capture the reflected line, these instruments use a 2D optical detector; u and v are respectively the horizontal and vertical pixel positions of the line, while f_x and f_y are the horizontal e vertical focal length scaled to the detectors pixel unit. The 3D coordinates of each point, along the line corresponding to pixel position (u, v) in the projection plane, can be computed according to the following equation:

$$\begin{bmatrix} x \\ y \\ z \end{bmatrix} = \begin{bmatrix} \dfrac{u \cdot \tan\beta}{f_x \cdot \tan\beta + u} z_0 \\ \dfrac{v \cdot f_x \cdot \tan\beta}{f_x \cdot f_y \cdot \tan\beta + f_y \cdot u} z_0 \\ \dfrac{f_x \cdot \tan\beta}{f_x \cdot \tan\beta + u} z_0 \end{bmatrix} \tag{6}$$

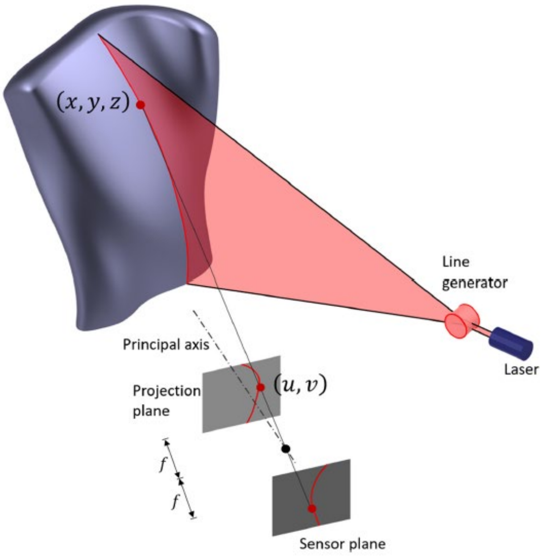

Figure 8. Triangulation of laser stripe points (x, y, z), image projection (u, v) and the laser. Source: from [14]

Stripe LT sensors are used to achieve faster measurement rates for image; the scan of an entire area can be obtained by just sweeping the laser line over the target. Even faster measurements are achieved by projecting and acquiring multiple laser lines simultaneously. Multi-line LT sensors are considered to be 2D techniques because, even if they do not acquire a just 2D profile, to properly scan an area a mechanism for the movement of the LT sensor or the measured object is necessary. Although multi-line LT sensors inspect a wider spatial portion per frame, in this thesis they are still conceptually classified as 2D measuring techniques, as they require a motion of the pattern over the surface to map a cohesive 3D point cloud.

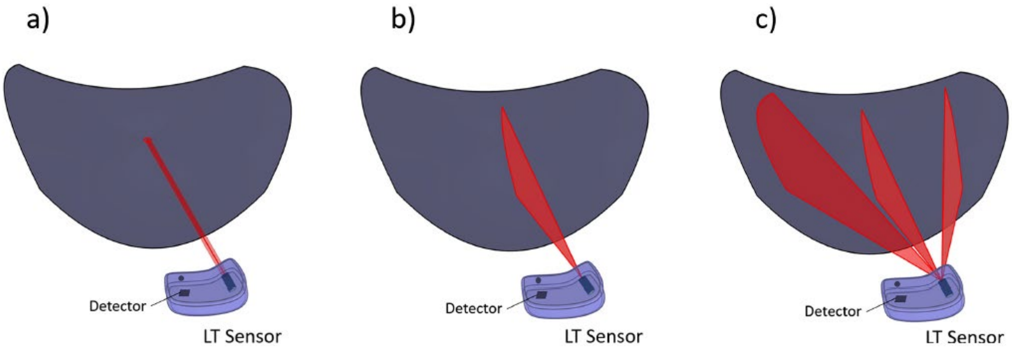

Figure 9. Dimensions of projected laser beams used in LT sensors; a) Point LT sensor; b) Stripe LT sensor; c) Multi-line LT sensor. Source: from [14]

Regardless of the specific laser configuration, a movement system and registration method are required to correctly unify within the global coordinate system the information of each image acquired over time. Real-time registration can be achieved with the use of hardware-based methods, which rely on external information to understand the position of the sensor in the space. The external information depending on the type of instrument can be given by:

- **Encoders:** devices that translate the mechanical motion into electrical signals; this method is employed in CMMs mounting laser probing systems and laser scanning articulated arms.
- **External Optical Tracking Component:** the position of the handheld device can be monitored by external metrological hardware. This includes laser trackers utilizing interferometric distance measurements aimed at retroreflective targets mounted on the scanner, or external stereophotogrammetric camera bars that track dedicated active or passive targets fixed onto the chassis of the handheld sensor.
- **Live tracking:** the instrument dynamically establishes its own spatial coordinates by utilizing an integrated stereophotogrammetric system. The sensors embedded cameras continuously capture the spatial distribution of retroreflective positioning targets (markers) placed directly onto or around the workpiece. By identifying a minimum number of shared markers between consecutive frames, the software realigns the newly acquired laser profiles in real time through spatial resection and triangulation algorithms.

A popular kind of LT systems is represented by portable handheld devices, which are hand controlled by an operator who can freely move the instrument around the object, while the system performs real-time alignment and fusion as described above. These systems provide a desirable flexibility, which allows the inspection of complex parts and freeform components. Due to their ease of use and portability, handheld devices are nowadays more and more employed in industry, in particular for quality control, reverse engineering, and maintenance.

The HANDYScan 3D Silver by Creaform, subject of this research, falls in the category of the hand-held multi line LT sensors, which employs the live tracking of the markers for its positioning.

1.3 Surface Types

In optical coordinate metrology, the type of the target surface can severely affect the quality of the acquired point cloud. Specifically, it impacts key metrics such as accuracy, surface coverage, point density, noise levels, and the presence of outliers (commonly referred to as "spikes", which are data points located very distant from the actual surface [16]). This occurs because light can interact with the surface in different ways, strongly depending on the material's surface finish, colour and composition [17].

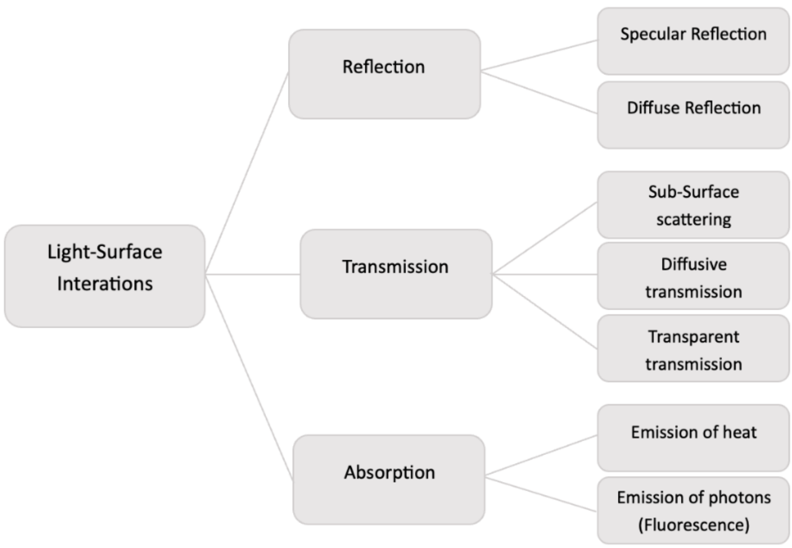

Figure 10. Schematic of light-surface phenomena

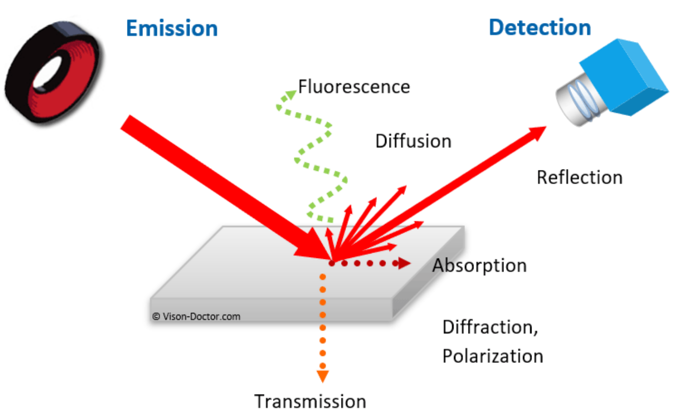

Figure 11. Interactions between light and surface. Source: from [18]

To formally describe the phenomenon of light-matter interaction, the fundamental optical energy balance can be introduced. The intensity of the incident light beam I_0 is divided into three main components according to the following conservation equation:

$$I_0 = I_R + I_T + I_A \tag{7}$$

Where I_R represents the reflected intensity, I_T is the transmitted, and I_A is the absorbed intensity. For LT sensors, the way incident light is reflected by the target surface, and consequentially collected by the sensors cameras, is of fundamental importance. The total reflected intensity I_R can be divided into two main directional components: the specular reflected light I_S, and the diffuse reflected light I_D, leading to the following equation:

$$I_R = I_S + I_D \tag{8}$$

The spatial distribution of the two components of reflected light is mathematically described by the Bidirectional Reflectance Distribution Function (BRDF) as described in the work of F. E. Nicodemus et al [19]. In simple terms, the BRDF is the mathematical representation of the reflected pattern (or lobe) generated when a light beam hits a surface.

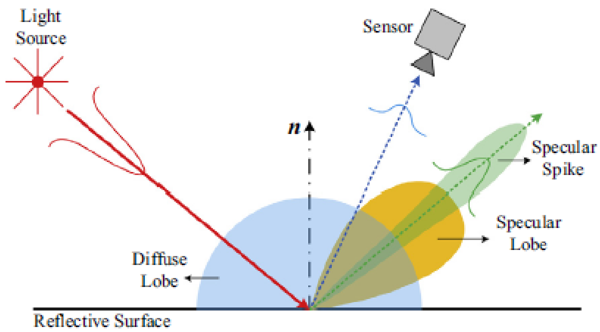

Figure 12. Light reflection components in scanning a reflective surface. Source: from[20]

Consequently, depending on how the intrinsic physical and optical properties of the material alter the optical energy balance and the spatial distribution of reflected light, surfaces can be metrologically classified into two broad categories: cooperative and non-cooperative.

1.3.1 Cooperative surfaces

A surface is defined as cooperative when its optical properties maximize the quality of the backscattered signal acquired by the sensors. This condition is met when the surface exhibits predominantly diffuse reflection, as represented in Figure 13; this ideal behaviour is characteristic of Lambertian surfaces.

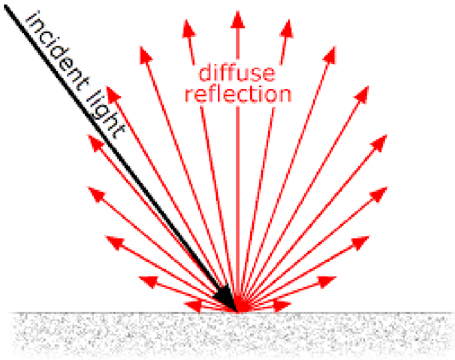

Figure 13. Representation of a Lambertian Surface.

The total diffuse reflection is described by the Lambert's cosine law, which says that the luminous intensity $I(\theta)$ is directly proportional to the cosine of the angle θ between the observation direction and the surface normal:

$$I(\theta) = I_n \cos\theta \tag{9}$$

Lambertian surfaces are also called isotropic diffuse reflectors since the radiance L_D captured by the optical sensor is constant, thus giving a uniform signal independent of slope θ of the sensor, thereby preventing local sensor saturation and uncontrolled intensity gradients. This can be explained by considering the definition of radiance:

$$L_D = \frac{I(\theta)}{A_{proj}} = \frac{I_n \cos\theta}{A\cos\theta} = \frac{I_n}{A} = constant \tag{10}$$

The use of calibrated artefacts made with cooperative finishes (e.g. opaque ceramic spheres) is in fact prescribed by the ISO 10360-13 standard for the metrological verification of measuring systems, as it allows the intrinsic uncertainty of the instrument to be isolated from the variables introduced by the material under examination.

1.3.2 Non-Cooperative surfaces

Conversely, a surface is classified as non-cooperative when its behaviour differs from an ideal Lambertian surface and its optical and physical characteristics prevent the acquisition of accurate and reliable data because the sensor cannot collect the backscattered light or its path is distorted leading to missing data, elevated noise levels, or the generation of severe measurement outliers [16]. The main measurement challenges can be categorized as follows:

- **Specularity:** shiny surfaces promote a strong specular reflection generating a narrow and highly directional BRDF lobe. The shininess of a surface is intrinsically linked to the surface texture, when it presents a roughness comparable to or significantly smaller than the wavelength of the incident laser, it behaves as an optical mirror. When the specular beam is deflected away from the cameras field of view, the signal cannot be captured; conversely, if it reflects directly into the lens, it causes an overexposure and pixel saturation (Figure 14). Moreover, on shiny concave geometries the problem of secondary reflections becomes even more relevant generating false geometric data (spikes) [16].

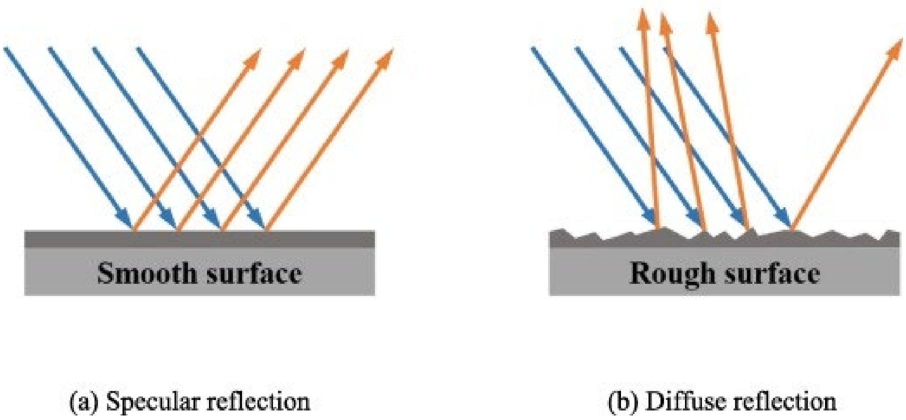

Figure 14. Smooth vs rough surfaces type of reflection. Source: from [21]

- **Subsurface Scattering:** the light beam penetrates the translucent material, such as uncoloured polymers, glasses, resins, and certain ceramics, and it is scattered in different directions, the light returns to the sensor from a point that differs from the incident point, increasing the width of the laser point or line and introducing a distortion, as shown in Figure 15.

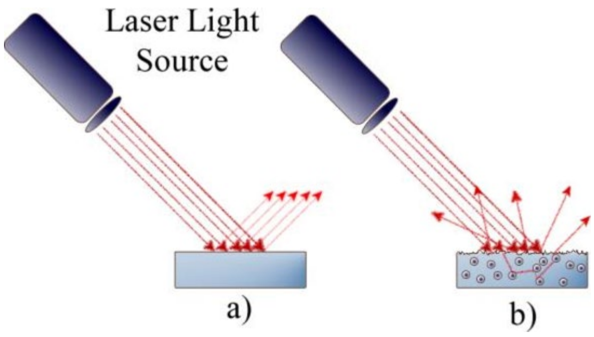

Figure 15. Strong Sub-Surface Scattering can degrade the quality of the measurement. Source: [22]

- **High Transparency:** very transparent materials cannot be measured since the light is passing through the component, usually showing little to no reflection.
- **High absorption:** dark-coloured surfaces, such as carbon fiber reinforced plastics, or materials that have high absorbance of incident light, cause the absorption component I_A to be predominant and consequently, the reflected intensity I_R to be drastically reduced. Thus, in this case the sensor can collect only a small amount of reflected light resulting in underexposure of the camera's pixel.

These problems are faced in industrial and metrological applications with the applications of specific spray mattifying coatings. In some cases, the adjustment of the scanner parameters, such as the shutter speed, the exposure time or laser power can result in an improvement in quality measurement.

1.3.3 Mattifying spray coatings

To transform a non-cooperative surface into a cooperative one, the application of a mattifying coating through specific sprays is common practice. These coatings cover the surface with an opaque material that prevents specular reflection but also the transmission inside the material, the thickness and homogeneity of the layer depend on the operator ability. There are different types of coatings, and they can be classified as:

- *Traditional sprays | Permanent Sprays:*
  In this category all the coatings that don't evaporate from themselves, but they need to be removed in a second step after the measurements. The use of these sprays can be useful for the repeatability of multiple measurements taken over time but in industrial cases it introduces an additional step, and the act of cleaning could damage the surface.

They are made with a solid powder/compound that is sprayed on the surface by a pressurized gas or solvent, such as ethanol or n-pentane; most commercialized sprays contain powder either of titanium dioxide (TiO2), chalk or zinc stearate.

- *Sublimating sprays | Temporary Sprays*

  They use a sublimating agent which deposits on the surface as solid particles, but as the time passes the crystals sublimate directly at the gas state. They have the great advantage of not needing a cleaning step but their effect changes over time as the layer is sublimating.

The use of these mattifying coatings is common practice in industrial shop floors as they help strongly improving the measurement of workpieces with non-cooperative surfaces. Given their importance in industrial applications, mattifying sprays and coatings have been extensively investigated in the literature [23–26]

1.4 Performance Evaluation

The verification process is defined by the VIM as "*provision of objective evidence that a given item fulfils specified requirements*" [3], and it is performed through rigorous tests. Performance verification is a fundamental and rigorous procedure in metrology, which is applied to measuring systems to establish a metrological traceability, and to ensure that it operates consistently within specified metrological limits. Specifically, the system's measurement errors do not exceed the Maximum Permissible Errors (MPE) declared by the manufacturer. The maximum permissible error, in the VIM is "*the extreme value of measurement error, with respect to a known reference quantity value, permitted by specifications or regulations for a given measurement, measuring instrument, or measuring system*". The MPE in geometrical metrology can be stated in either one of three forms:

$$MPE = \pm B \tag{11}$$

$$MPE = \pm\left(A + \frac{L}{K}\right) \tag{12}$$

$$MPE = \pm \min\left(A + \frac{L}{K}; B\right) \tag{13}$$

Where A, B and K represent three constants associated with the measuring system, while L is the length of the measured characteristic.

For a measurement system to pass the performance verification tests, the measurements must conform to a set of MPEs. Generally, performance verification is divided into three main categories: acceptance tests, reverification tests, and interim tests. Acceptance tests are performed at the beginning of the instrument's lifecycle to validate the manufacturers specifications. Conversely, reverification tests are performed periodically by the user to ensure the instrument maintains its intended metrological performance over time. Both of these formal procedures require the use of calibrated, traceable artefacts measured under strictly controlled environmental conditions. Finally, interim checks are simplified, routine tests performed between reverifications. They are designed to maintain confidence in the systems ongoing performance and to quickly detect any systematic error.

The standardization of these tests for coordinate measuring systems (CMSs) is of fundamental importance. The reference standards are contained in the ISO 10360 series, which establishes a universal vocabulary and testing procedures for acceptance and reverification tests. This series is regarded as a general Geometrical Product Specification (GPS) standard, as reported in the Matrix Model described in the ISO 14638 [27].

Historically, this series was developed for the standardization of contact CMMs by defining a rigorous vocabulary in ISO 10360-1:2001 [28] and testing procedures in ISO 10360-2:2009 [29]. However, the rapid development of non-contact optical instruments necessitated an expansion of this normative framework. The ISO 10360-8:2013 [30] was introduced to address the integration of optical distance sensors onto traditional CMMs. Given the absence of dedicated performance evaluation protocols for multiple view systems based on area scanning, manufacturers relied heavily on the German guideline VDI/VDE 2634 part 3, which at the current time has been withdrawn. Recently, this framework was formalized and expanded at the international level with the publication of ISO 10360-13:2021. The procedures from ISO 10360-13 are based on the VDI/VDE while introducing some key differences.

1.4.1 VDI/VDE 2634 Part 3

Before the introduction of specific ISO standards for optical CMSs, the metrology laboratories and manufacturers relied on the German guideline VDI/VDE 2634 part 3. This document was published in 2008 by the Association of German Engineers (VDI), representing the first effort to establish a standardized evaluation protocol for optical 3D measuring systems based on area scanning. For context, the VDI/VDE 2634 series has three parts: Part 1 (2002) covers photogrammetric or point-by-point imaging systems, Part 2 (2002) covers single-view area-scanning systems (e.g. fringe projectors or laser stripe scanners), and Part 3 (2008) covers multi-view area-scanning systems (scanners or systems that capture an object from multiple positions).

The guideline defined specific test artefacts and introduced key quality parameters such as probing error, sphere-spacing error, and flatness measurement error. Although it was technically a national guideline rather than an international standard, its robust methodology made it the universally accepted *de facto* standard in the industry for years, serving as the fundamental groundwork upon which the modern ISO frameworks were subsequently built. The VDI/VDE 2634 part 3 was officially withdrawn in February 2024 in favour of ISO 10360-13.

1.4.2 ISO 10360-13:2021

As optical 3D CMSs became increasingly common, the need for a globally recognized standard led to the publication of ISO 10360-13:2021. This standard supersedes the concepts of VDI/VDE 2634 part 3, formalizing the acceptance and reverification tests of optical 3D CMSs consistently with the other standard of the ISO 10360 series.

Important for the context of this research, the ISO 10360-13:2021 explicitly states in its scope that it is not originally intended for certain classes of instruments, specifically mentioning hand-held laser-line type scanners. However, the standard states that "*parties can apply this document to the above or other types of CMSs by mutual agreement*".

To effectively characterize an optical CMS, the standard introduces the definition regarding the measurement volumes:

- **Sensor Measurement Volume (SMV):** "*the volume of measurement of the sensor realized without movement of the sensor relative to the workpiece fulfilling the specifications stated by the manufacturer*".

- **Concatenated Measurement Volume (CMV):** "*volume of measurement of the CMS obtained by movement of the sensor relative to the workpiece and the registration fulfilling the specifications stated by the manufacturer*".

The standard also identifies two distinct measurement processes:

- **Single-View Measurement (SV):** "*measurement of spatial coordinates done with an optical sensor without movement relative to the workpiece*".
- **Multiple-View Measurement (MV):** "*measurement of spatial coordinates through registration and fusion of multiple single-view measurements in different locations and orientations of the optical sensor relative to the workpiece*".

As specified the document's notes, while within the SMV the data can be acquired with both a single-view measurement and a multiple-view measurement, in the case of CMV the measurement falls automatically in the multiple-view case.

The metrological performance of the instrument is evaluated through a set of rigorous metrics which require the measurement of calibrated, traceable artefacts and the assessment of specific errors. From these values a set of Maximum Permissible Errors (MPEs) is found and the compliance with the manufacturer specifications is checked. These quality metrics include the probing size and form errors, flat-form distortion errors, distortion errors and volumetric length measurement errors. In Table 2 a comparison between the errors presented by the VDI/VDE2634 part 3 and the ISO 10360-13.

Name of error	**VDI/VDE 2634-3 Symbols**	**ISO 10360-13 Symbols**	**i qualifiers**	**j qualifiers**
Probing Size Error	PS	$P_{Size.Sph.i:j:O3D}$	All - 95%	SMV.SV - SMV.MV
Probing Form Error	PF	$P_{Form.Sph.i:j:O3D}$	All - 95%	SMV.SV - SMV.MV
Flat-Form Distortion Error	-	$D_{Form.Pla.i:j:O3D}$	All - 95%	SMV.SV - SMV.MV -
Distortion Error	SD	$D_{CC.j:O3D}$	-	SMV.SV - SMV.MV -
Volumetric Length Measurement Error	E	$E_{Vol.j:O3D}$	-	CMV.MV

Table 2. Comprehensive summary of the errors as defined in the guide VDI/VDE 2634-3 and in the standard ISO 10360-13. Source: adapted from [14]

Probing Size Errors $(P_{Size.Sph})$

It is defined as the error of indication when measuring the calibrated diameter of a test sphere, calculated via a least-squares fit of a designated percentile (100% or 95%) of all acquired point cloud (Figure 16).

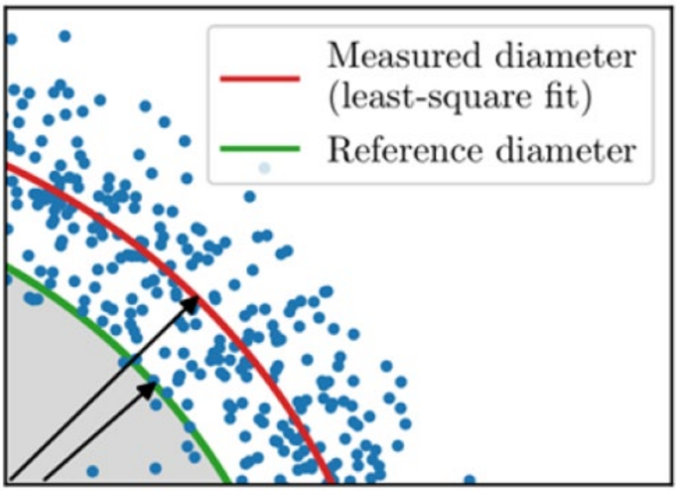

Figure 16. Bidimensional representation of Probing Size Error. Source: from [31]

Probing Form Errors $(P_{Form.Sph})$

It is defined as the smallest width of a spherical shell that encompasses a specific percentile (100% or 95%) of all measured data points on a calibrated test sphere. This metric describes the local dispersion and noise intrinsic to the point cloud.

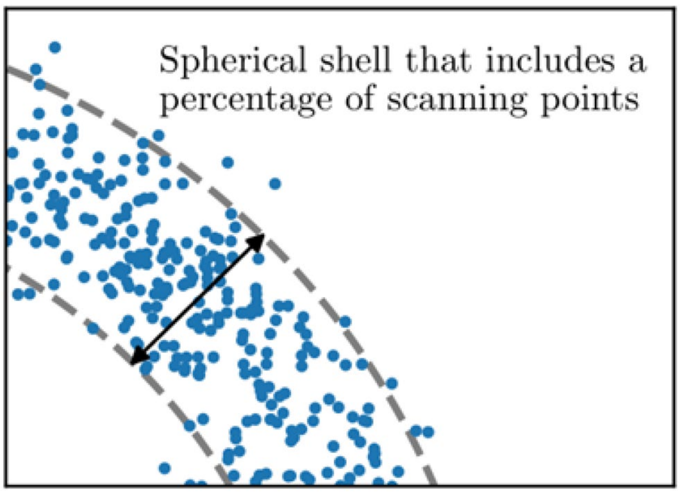

Figure 17. Bidimensional representation of Probing Form Error (95%). Source: from [31]

Flat-Form Distortion Error ($D_{Form.Pla}$)

It is the minimum distance between two parallel planes that encompass a given percentile (100% or 95%) of data measured on a calibrated test flat plane. Similarly to the Probing Form Error, this metric measures the dispersion and noise of a point cloud, but when measuring a perfectly flat surface.

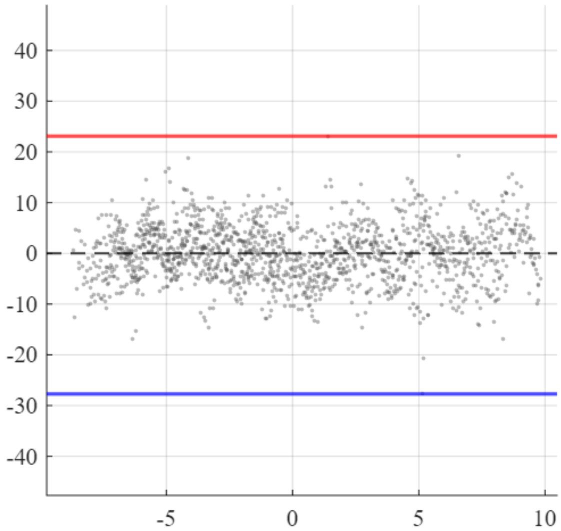

Figure 18. Representation of the Flat-Form Distortion Error.

Distortion Error (D_{CC})

The error of indication when measuring a calibrated centre-to-centre distance (using a ball bar) within the sensor measurement volume. The objective of this metric is to isolate and quantify the geometric deformations intrinsic to the sensor's optical system without the compounding influence of global sensor displacements or external reference tracking.

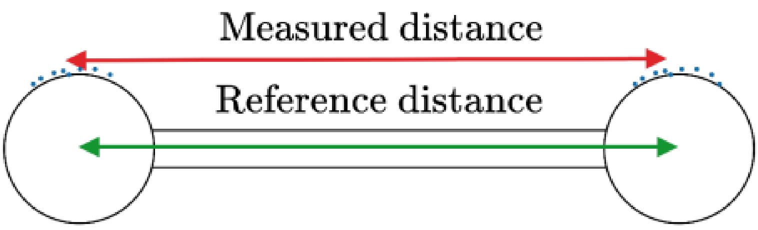

Figure 19. Bidimensional representation of the Distortion Error. Source: from [31]

Volumetric length measurement error (E_{Vol})

It represents the error of indication when measuring five calibrated lengths along different positions and orientations using a ball beam. Unlike the local distortion error, E_{Vol} is designed to evaluate the macro-scale 3D volumetric accuracy of the system. It quantifies how measurement errors propagate through the spatial concatenation pathway and the registration algorithms.

1.5 Literature gap and motivation of the work

The ISO 10360 series define the basis for the acceptance and reverification tests of CMSs, with the introduction of a rigorous framework; however, despite its evolution, its direct application to certain modern metrological instruments presents critical challenges. Handheld multi-line laser scanners do not fit into ISO 10360-8, nor are they fully aligned with ISO 10360-13, which was designed for optical CMSs rigidly mounted on a CMM or fixed support, rather than freely handled by an operator. As introduced previously in this chapter (section 1.2.3), handheld multi-line laser scanners are intrinsically dynamic multi-view optical CMSs, unable to collect the 3D data of a full area in a single frame. Instead, they acquire points corresponding to a laser grid, requiring manual motion by the operator, and fuse together the points from the different views through a live tracking system.

This dynamic operational behaviour creates a significant normative gap. Handheld laser scanners lack a clearly defined, static Sensor Measurement Volume (SMV) as introduced in the ISO 10360-13 testing protocols. This aspect makes the execution of the acceptance and reverification tests ambiguous, and no dedicated standard has been issued yet. A rigorous adaptation of the ISO 10360-13 framework is therefore necessary to establish a reliable protocol for evaluating the metrological performance of handheld laser scanners. In practice, manufacturers of handheld scanners often rely on procedures based on the ISO 10360 series and the withdrawn technical guide VDI/VDE 2634 part 3, frequently combining the two, simplifying some tasks, and not adopting well-defined kinematic strategies.

Not much can be found in the literature about a direct adaptation of these performance verification standards to handheld LT sensors specifically, but a number of related studies address the problem from different angles, offering both useful precedents and evidence of the gap this thesis aims to fill.

In the work of Kersten et al. [32] were tested the geometrical accuracy of several handheld scanning systems, including the Creaform HandySCAN 700, DOTProduct DPI-7/DPI-8, Artec Spider, and Mantis Vision F5 SR, in a comparative campaign. Reference data were acquired with two structured-light projection systems used as ground truth, and the quality metrics followed the VDI/VDE 2634 Part 3 vocabulary: probing form error (PF), probing size error (PS), and sphere-spacing error (SD). A practical detail reported by the authors, directly relevant to the present work, is that handheld scanners must be moved manually, slowly and uniformly around the object, at a working distance typically between 20 cm and 50 cm, a constraint that anticipates the need, addressed in Chapter 2, to define controlled scanning kinematic strategies for the HandySCAN.

The study of Kalinowski et al. [33] investigated three handheld structured-light scanners (Creaform GO!Scan Spark, Artec Eva, and Artec Spider) using dumbbell artefacts with three different textures (a heterogeneous black-and-white pattern, a plain white surface, and a metallic surface), following the VDI/VDE 2634 part 3 guideline calculating the sphere distancing (SD), the probing form (PF) and size (PS) errors. The probing form error also depended on both instrument and surface: the GO!Scan was largely insensitive to texture, the Eva showed the highest error on the textured sphere, and the Spider showed the highest error on the metallic sphere, likely due to stronger reflections at its short working distance.

Icasio-Hernández et al. [34] assessed the sensitivity of the length tests defined in the VDI/VDE 2634-2 guideline and the ISO 10360-13 standard to systematic errors in structured-light systems, using a structured-light sensor mounted on a Cartesian CMM to position the target within the measurement volume. Their sensitivity analysis identified which positions and orientations of the test lengths within the measurement volume are most revealing of systematic errors. This is, to date, one of the few studies to place the VDI/VDE and ISO 10360-13 frameworks side by side on the same instrument, and it supports the assumption adopted throughout this thesis that the two approaches can be treated as largely equivalent in metrological intent, which justifies drawing on both when adapting the standard to the HandySCAN.

Finally, Abe [35] addressed the volumetric length measurement error (E_{Vol}) defined in ISO 10360-13, proposing a prototype material standard with densely distributed observation points arranged in a two-dimensional planar layout to re-validate length-measuring performance tests, and comparing two different concatenation pathways for combining multiple single-view length measurements: one conservatively optimized, the other deliberately detoured. The results showed a measurable dependency of the capture efficiency on the concatenation strategy adopted. This finding confirms that the choice of scanning and registration pathway, not only the intrinsic sensor performance, can influence the resulting volumetric accuracy of a concatenated measurement.

The effect of user-controllable scanning parameters, central to the second objective of this thesis, was investigated by Ameen et al. [36] in a study on handheld scanners for automotive applications. Using a free-form car door as the test object, the authors compared two handheld scanners against a CMM equipped with a continuous scanning touch probe, applying a three-level Design of Experiments to optimize scanning parameters including resolution, shutter speed, and laser power. This is, among the reviewed literature, the only study to treat shutter speed explicitly as an experimental factor rather than a fixed acquisition setting, and it provides a direct methodological precedent for the shutter speed optimization campaign carried out in Chapter 3. The present thesis, however, narrows the investigation to calibrated cooperative and non-cooperative spheres rather than a free-form industrial part, in order to isolate the effect of the parameter from the added complexity of a free-form geometry.

Particularly relevant to how surface type affects measurement performance is the work of Meana et al. [37]. This study compared the performance of three laser triangulation sensors: one automatic sensor mounted on a CMM, and two handheld sensors mounted on articulated measuring arms of different generations. The sensors were used to scan six high-precision reference spheres, made of different materials (steel, ceramic, polymer) and with different surface finishes (glossy and matte). The study identified and quantified a systematic effect known as the "edge effect" or "horizon effect". This effect reduces the accuracy of the points acquired near the apparent edge of the sphere, where the laser beam hits the surface at a near-tangent angle. The authors also observed that surface finish has a major influence on sensor performance, often greater than geometry alone. The glossiest sphere could not be measured by either the automatic sensor or the older handheld sensor. Only the most recent handheld sensor was able to acquire it correctly. There, the effect of surface finish on the point cloud quality acquired by the HandySCAN is comparable to, or even greater than, the effect of sphere size alone.

The reviewed studies show that individual VDI/VDE 2634 and ISO 10360-13 metrics, such as probing errors and length test, can be applied to handheld optical scanners, though none adapts the framework as a whole. In particular, none proposes a full verification protocol for a multi-line handheld laser scanner, nor systematically relates acquisition parameters such as shutter speed to the standardized error metrics under non-cooperative surface conditions.

This gap is consistent with the scope clause of the standard itself, which explicitly excludes hand-held laser-line type scanners while allowing parties to apply the document "to the above or other types of CMSs by mutual agreement", a provision that constitutes the foundation for the approach adopted in this thesis. In industrial practice, manufacturers themselves commonly refer to ISO 10360-13 for the acceptance and reverification of handheld systems, while simplifying or adapting specific tasks of the protocol to the dynamic nature of these instruments, as also confirmed by the acceptance procedure applied by Creaform to the HandySCAN SILVER (see section 2.1.1).

Performance verification, in both the standard and the reviewed literature, is generally carried out under cooperative surface conditions, which maximize the stability and repeatability of the results. However, when these conditions are not guaranteed, as is frequently the case with non-cooperative industrial surfaces, it becomes relevant to evaluate how the standardized quality metrics vary as a function of the scanners exposure settings. Building on the DoE -based precedent of Ameen et al., but focusing specifically on shutter speed and on calibrated, traceable artefacts of both cooperative and non-cooperative finish, this thesis aims to fill this specific and currently unaddressed intersection between the ISO 10360-13 framework and the practical challenges of scanning non-cooperative materials in industrial conditions.

The present thesis pursues two main objectives:

1) to define a rigorous protocol for evaluating the metrological performance of handheld laser scanners, adapting the ISO 10360-13 framework to a Creaform HandySCAN SILVER;
2) to investigate the effect of shutter speed, a user-controllable acquisition parameter, on measurement quality when scanning both cooperative and non-cooperative surfaces.

The first objective is addressed in Chapter 2, responding to the normative gap discussed above. The second objective, discussed in Chapter 3, focuses on isolating the effect of shutter speed through a dedicated single-factor Design of Experiment repeated on both cooperative and non-cooperative calibrated spheres. The ultimate goal is to provide a useful basis for future standardization, as well as a practical tool for obtaining reliable measurements in an industrial setting.

Chapter 2: Performance Evaluation of handheld laser-based sensor

The primary objective of this chapter is to present a comprehensive overview of the methodology developed to evaluate the metrological performance of the Creaform HandyScan 3D Silver handheld laser-based sensor. Since this instrument operates in an inherently dynamic manner, the performance presents some challenges compared to traditional stationary optical coordinate measuring systems (CMS). Consequently, the methodological framework of this work is built upon a controlled adaptation of the international standard ISO 10360-13:2021. The following sections describe the calibrated material measures used as geometric references, the kinematic scanning strategies implemented to simulate and concatenate measurement volumes, and the software pipeline employed for data post-processing and the computation of probing, distortion, and form errors. This thesis work was carried out at the metrology laboratory of the Department of Industrial Engineering (DII) at the University of Padua.

2.1 Materials, Laboratory Instrumentation

This thesis work was carried out at the metrology laboratory of the Department of Industrial Engineering (DII) at the University of Padua. The laboratory is kept at a controlled temperature and humidity level at (20 ± 0.5) °C and (45 ± 10) % respectively. The following sections present the technical specifications and characteristics of the HandySCAN Silver portable laser scanner, the ball beam and the flat plane used for the performance verification tests.

2.1.1 Handheld multi-line laser-based sensor: Creaform HandySCAN SILVER

The instrument under metrological analysis in this project is the HandySCAN SILVER (Serial Number: 9670050) by Creaform Inc.

As anticipated in the previous chapter (section 1.2.3) it is a multi-line handheld laser-based sensor, from hereafter identified as HandySCAN in this thesis, and that falls in the class of the Optical 3D CMSs. During the scanning process (Figure 20), the device projects a grid pattern made of 14 blue laser (of class 2M) lines onto the surface of the workpiece. The integrated dualcamera system records the deformation of these laser lines as they adapt to the objects geometry, continuously computing the 3D surface coordinates to generate a point cloud. Simultaneously, the scanner tracks its own movement relative to the part by identifying the positions of retro-reflective targets, of 6 mm diameter, placed either directly on the workpiece or in the surrounding environment, essentially locking the coordinate reference system to the part itself.

Figure 20. Scanning process with the HandySCAN SILVER. Source: [38]

The instrument is connected via cable to both the power supply and a PC, and operated through the proprietary VXelements software. The only controllable hardware scanning parameter available to user control is the Shutter Speed. Expressed in milliseconds (ms), this parameter defines the temporal interval during which the shutter remains open, which directly corresponds to the synchronized pulse duration of the projected multi-line laser grid. This behaviour was observed during preliminary experimental tests, and it is not openly described by the manufacturer. The shutter speed values range between a minimum value of 0.10 ms to a maximum limit of 8 ms, featuring a default setting of 0.15 ms; its precise value can be set either manually by the user or automatically (suggested when the scanned surface is large enough) prior to the starting of the measurements, by the system in a specific setting widow. This parameter controls how much light can be captured by the optical sensors: higher values allow more laser light to reach the cameras, increasing exposure, while lower values reduce it. The cameras work the best within a certain exposure range, but the amount of light reflected depends on the surface colour and characteristics (as discussed in the section 1.3), selecting an appropriate shutter speed is essential to ensure correct acquisition. The exposure conditions are schematically presented in Table 3. The manufacturer suggests keeping the shutter speed close to its default value, since higher values reduce acquisition speed, in particular when the scanner is moved rapidly. Moreover, longer exposure intervals may introduce motion related artefacts: relative displacements between the scanner and the surface during the measurement may result in blurred laser lines images, negatively affecting point cloud quality.

Colour	Status	Description
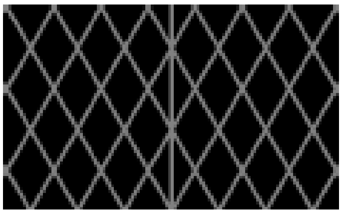	Underexposed	The cameras are not or are only weakly perceiving the reflection of the lasers. The software is not gathering enough information to calculate and build a mesh
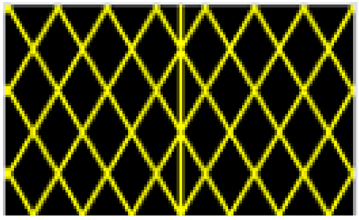	Optimal	The lasers are seen as clean and defined lines. Surface calculations is done in ideal circumstances
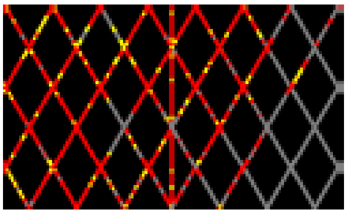	Saturated	The reflection of the lasers is so intense that the cameras are dazzled. Laser lines are not clearly defined and may lead to an improper surface reconstruction or an unusual amount of noise in the data.

Table 3. Status of the camera sensors depending on the shutter speed level. Source: Creaform manual.

The technical specifications of the measuring system are reported by the manufacturer and summarized in Table 4.

Manufacturer technical specifications	
Accuracy	Up to 0.040 mm
Volumetric accuracy	0.020 mm ± 0.1 mm/m
Working Distance	From 200 mm to 450 mm
Depth of Field	250 mm
Measurement Rate	800 000 measurements/s
Measurement Resolution	0.03 mm
Mesh Resolution	0.20 mm
Scanning Area	(310 × 350) mm
Light source	14 blue laser lines
Shutter speed	From 0.10 ms to 8 ms

Table 4. Technical specifications of the HandySCAN SILVER. Source: Creaform.

Prior to the purchase, the HandySCAN SILVER underwent acceptance testing performed by Creaform Inc. (certificate No 02-24176-0689, issued on 2024-06-25). The procedure, carried out according to Creaforms internal protocol ATP962 -01, assessed both the volumetric accuracy through sphere spacing measurements, adapted from the guide VDI/VDE 2634-3, and the dimensional accuracy through sphere diameter measurements.

For these tests 4 ball bars of 2 different lengths (520 mm and 435 mm) were employed to perform the acceptance procedure.

The results of the instrument calibration certificate are reported in Table 5. Figure 22 shows the Sphere Spacing errors measured in the four different ball bar positions, while Figure 23 reports the Probing Size errors values measured in the different sphere positions.

Test	Specifications	Limits / mm	Results / mm
Sphere Spacing	Volumetric accuracy L = 520 mm	± 0.0721	0.0283
Sphere Spacing	Volumetric accuracy L = 435 mm	± 0.0594	0.0040
Sphere Size Error	Deviation from nominal diameter	-	0.0324

Table 5. HandySCAN SILVER calibration test results

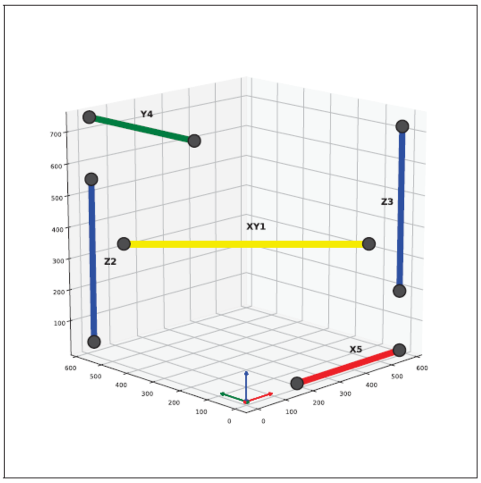

Figure 21. Ball Bars positions in the Creaform Inc. Acceptance Test of the Creaform HandySCAN BLACK, for the SILVER model the XY1 position is not taken into account. Source: Creaform

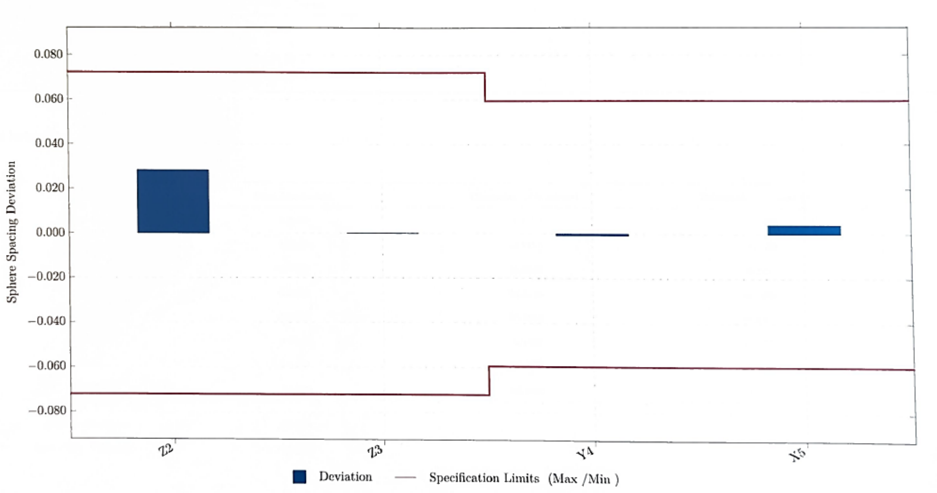

Figure 22. Sphere Spacing errors in the four different positions. Source: Creaform calibration certificate 02-24176-0689

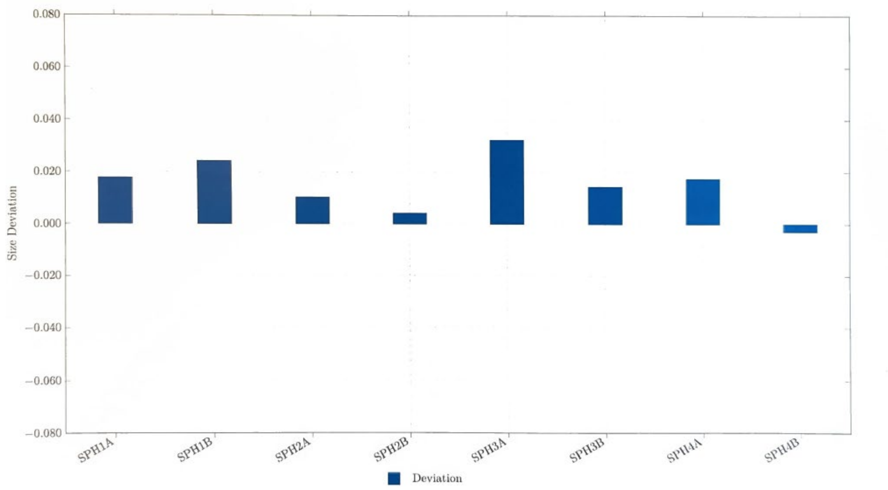

Figure 23. Probing Size Errors measured in different position. Source: Creaform calibration certificate 02-24176-0689

All the measured deviations lie within the specification limits, confirming the instrument compliance at the time of acceptance. The acceptance verification tests were performed following reduced procedure based on both the ISO 10360 series and VDI/VDE 2634 guides.

2.1.2 Reference Material Measures

The verification process, as described both in the standard ISO 10360-13:2021 and in the technical guides VDI/VDE, requires the employment of calibrated artefacts, also called material measures. These tools are fundamental to establish the metrological traceability of the instrument. The dimensional and form characteristics of these standards must be certified with expanded uncertainty (U) levels significantly lower than the maximum permissible error (MPE) limits stated by the manufacturer of the sensor under evaluation. The surface roughness of the measured features must be negligible with respect to the MPE.

The surface-light interaction is of fundamental importance to the measurement quality, in this sense the ISO 10360-13:2021 states that the surface characteristics required are the one stated by the manufacturer, while the VDI/VDE2634-3 states that the surface must show only diffuse reflection. Two material measures are used in the performance verification process: a ball beam and a granite surface plate.

Ball Beam

The distortion errors and volumetric length errors are evaluated using a carbon fiber ball beam (Serial Number: 0626245016) manufactured by MetrologyWorks Inc. featuring 6 magnetic slots to attach the calibrated metallic spheres (Figure 24). The ball beam underwent metrological calibration by an accredited laboratory, under certificate No 5016-09262024.

Figure 24. Ball Beam

The certified centre-to-centre distances for the off-axis ball beam, referenced to the standard temperature of 20°C, are reported in Table 6.

Off Axis Scale Bar Certificate Length					
l_{1-2} / mm	l_{1-3} / mm	l_{1-4} / mm	l_{1-5} / mm	l_{1-6} / mm	CTE / K^{-1}
199.85812	399.92798	599.93530	799.92703	999.92703	1.51×10^{-6}

Table 6. Certificate lengths interval of the ball beam

The calibration and measurement expanded uncertainty associated with the certificate's lengths, expressed with a coverage factor K of 2 and corresponding to a confidence level of approximately 95%, is $U = (3.2 + 0.6L)$ µm.

The ball beam can be mounted on a KOBA tilting support, which allows to perfectly level the ball beam and to precisely incline it from a horizontal position to angles of ± 50° with 5° steps.

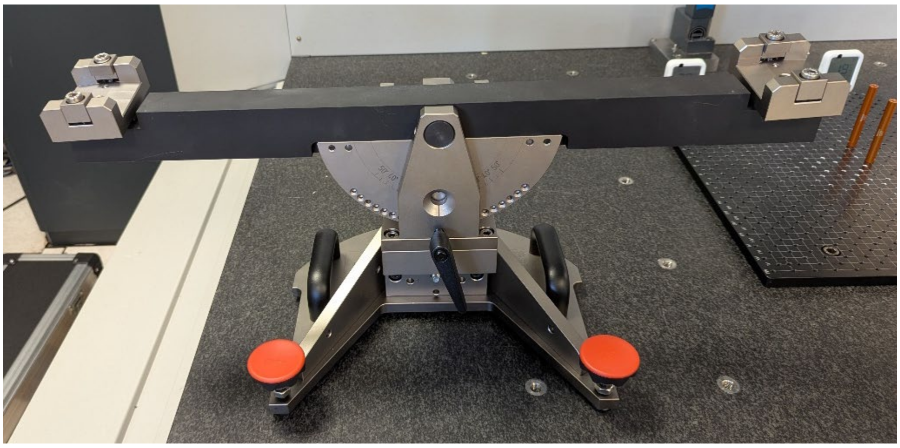

Figure 25. KOBA ball beam tilting support.

Matte calibrated spheres

Two set of calibrated spheres, compatible with the ball beam frame, are available in the laboratory equipment: one set of metallic matte spheres and the other of metallic shiny spheres.

The set of matte spheres (Figure 26) is used in the stage of performance verification, as they have cooperative surfaces and are ideal to evaluate the probing errors.

The measured data are reported in Table 7, with calibration and measurement uncertainties of ±43 µin (1.09 µm) for sphericity and ±39 µin (0.99 µm) for diameter, both at a coverage factor of K = 2.

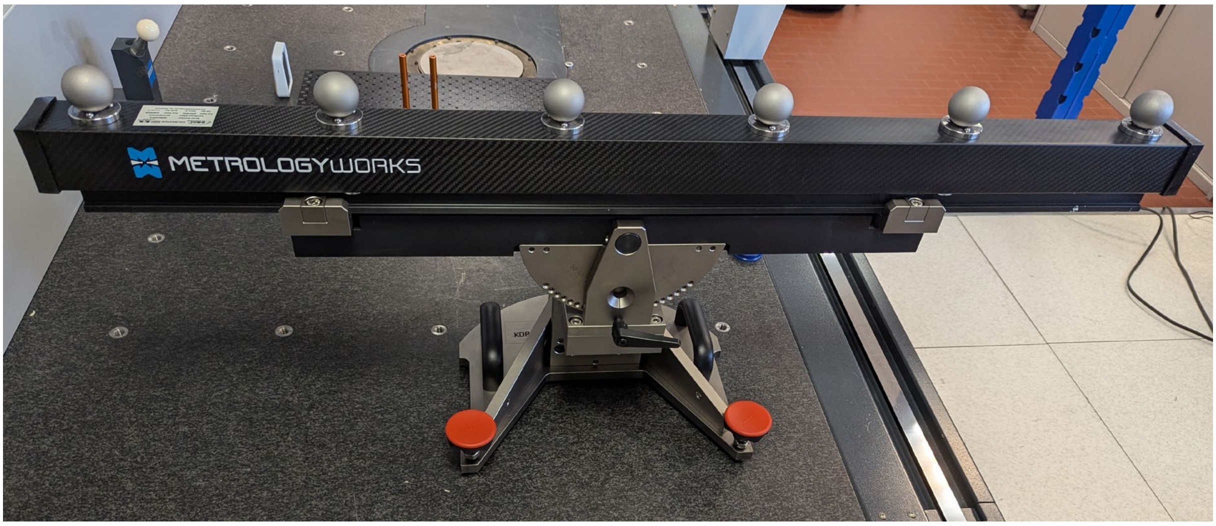

Figure 26. Test Ball Beam equipped with the matte metallic calibrated spheres.

Metallic matte spheres	Serial Number	Certificate	Sphericity / µm	Calibrated diameter / mm
1	20240409-01	0901-04092024	2.03	38.0942
2	20240409-02	0902-04092024	0.76	38.0985
3	20240409-03	0902-04092024	1.02	38.0987
4	20240409-04	0902-04092024	0.51	38.0967
5	20240409-18	0902-04092024	0.76	38.0972
6	20240409-19	0902-04092024	1.51	38.0922

Table 7. Calibrated diameters of the set of metallic matte spheres, measured at temperature of 20°C

<u>Granite Flat Plane</u>

The flat-form distortion error is evaluated using a precision granite surface plate (Serial Number: 06040425) manufactured by Mitutoyo Measuring Instruments Co., Ltd (Figure 27). The plate, classified as Grade 0 according to the manufacturers specifications, has nominal dimensions of 630 × 400 × 80 mm and was subjected to metrological calibration by the manufacturer under inspection certificate No. 06040425-SK. The calibration was performed at a controlled temperature of 20 °C and 58% relative humidity, on 2000-05-29.

The flatness deviation was assessed over a grid of measurement points distributed across the working surface, as shown in Figure 27. The measured flatness deviation across the surface was 2 μm.

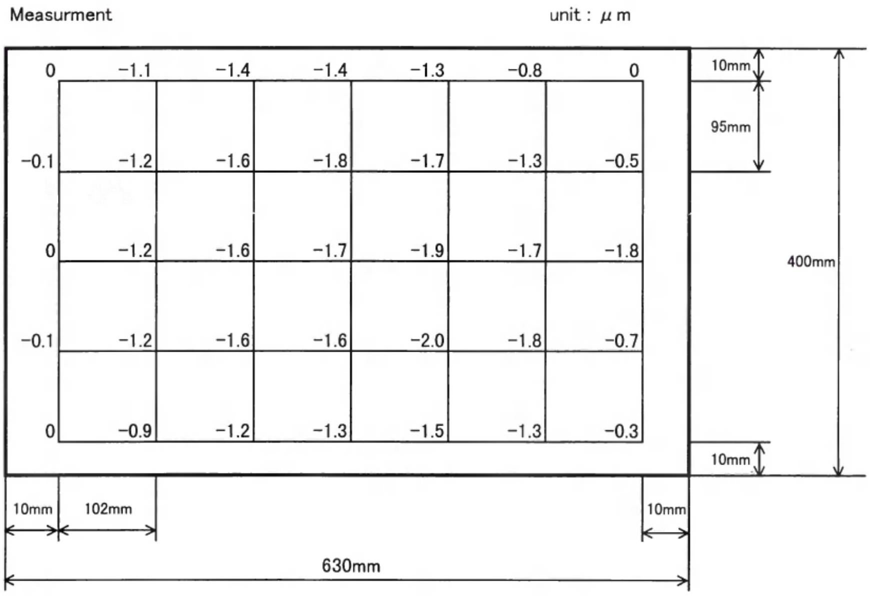

Figure 27. Mitutoyo granite flat plane calibration results. Source: calibration certificate 06040425 SK

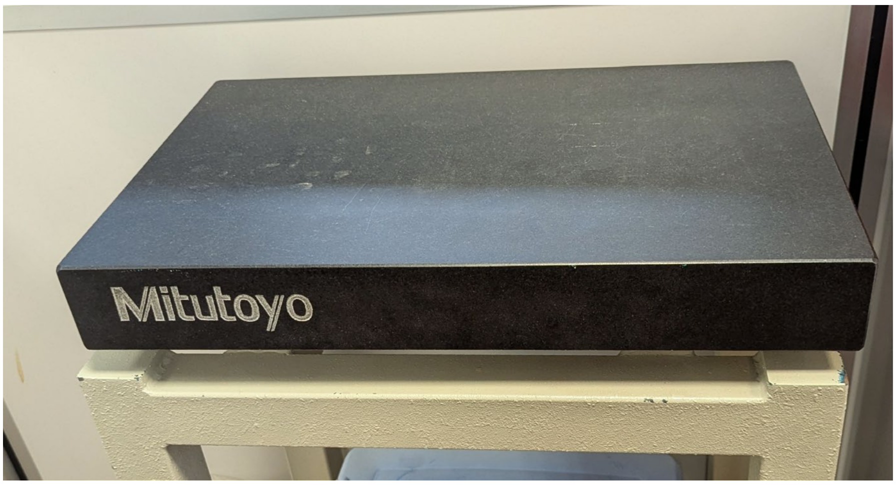

Figure 28. Mitutoyo granite plane

2.2 Performance Verification according to ISO 10360-13 framework

Handheld laser-based sensors, as described in the section 1.2.3 can be considered 2D measuring techniques; the Single View Measurement scan, obtained by keeping the instrument still, contains not enough data for a correct evaluation. For this reason, a new strategy is proposed, which involves the movement of the instrument following specific scanning kinematics (CMV.A, CMV.B and CMV.C), which are proposed in the following. Then, the description of the measurement procedures, divided for each error is reported.

2.2.1 Acquisition pattern characteristics

In the ISO 103600-13 framework, the Sensor Measurement Volume (SMV) covers a fundamental role in the verification processes. Despite multi-line laser scanners do not have a proper SMV, the same concept is used to describe the acquisition geometry, i.e. the spatial region within which the instrument is capable of acquiring valid data (mesh triangles) in a single frame. Given the divergent nature of the laser lines, the SMV takes the shape of a truncated pyramid (frustum) along the optical axis Z, whose bases correspond to the field of view (FOV) captured at the two ends of the depth of field: the smaller base at the minimum working distance (z_1 = 200 mm) and the larger base at the maximum working distance (z_2 = 450 mm).

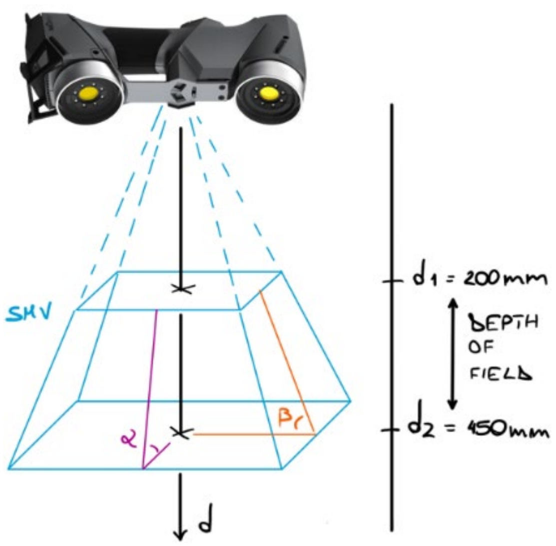

Figure 29. HandySCAN Sensor Measurement Volume (SMV) representation.

Since the manufacturers specifications provide only nominal values for the field of view, an experimental characterization is carried out to obtain a more direct indication of the actual dimensions of the SMV. The procedure consists of acquiring a plane positioned at different working distances within the declared depth of field. The distance between the scanner and the reference plane was estimated as the distance between the best-fit plane obtained from the acquired point cloud and the origin of the instruments reference frame, which is conventionally set at the scanner head at the beginning of the acquisition.

Two acquisitions are performed at the two extremes of the working range (corresponding to z_1 = 200 mm and z_2 = 450 mm), from which the effective field of view was estimated at each distance. The results indicate a field of view of approximately 210 × 250 mm² at the minimum working distance and approximately 380 × 450 mm² at the maximum working distance.

It should be noted that this experimental setup presents some limitations: the accuracy is limited by the manual positioning of the instrument, and the tilt of the measured plane with respect to the instruments reference plane was not explicitly accounted for. For this reason, the resulting values should be regarded as indicative approximations of the real SMV dimensions rather than exact measurements.

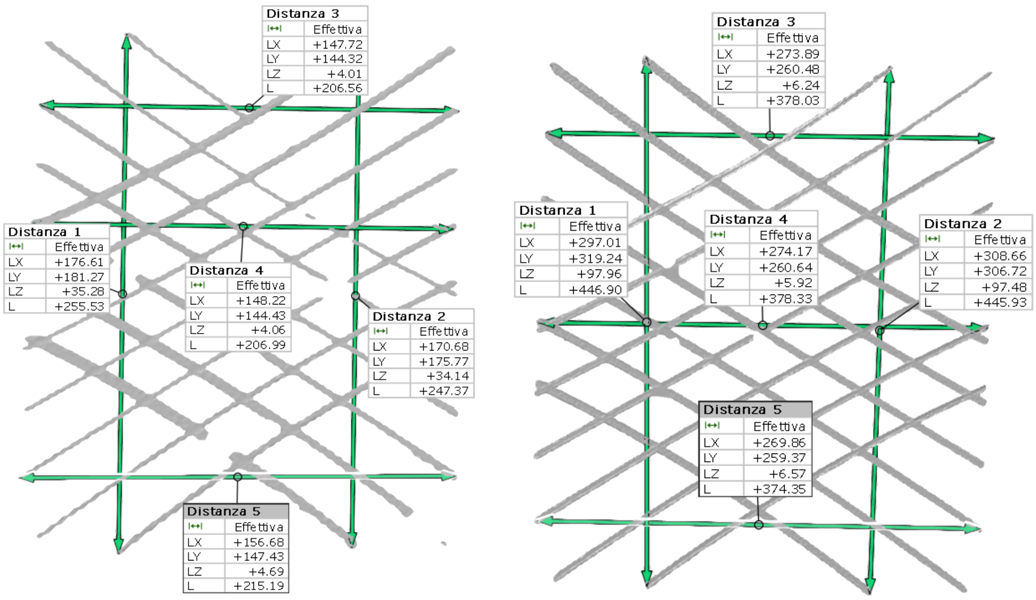

Figure 30. Field of view measurements at working distance of 250 mm and 450 mm

On the 2D projected laser pattern the longer side direction is called y while the shorter side direction is defined as x. The average distance between the lines in the scan taken at the maximum working distance, is approximately 50 mm in the x direction and 95 mm in the y direction.

2.2.2 Definition of Scanning Kinematic Strategies

According to the ISO 10360-13 three types of measurement volume strategies are provided across the different measurements (Table 2), each of them with a specific objective:

- SMV.SV (Sensor Measurement Volume - Single View)
- SMV.MV (Sensor Measurement Volume - Multiple View)
- CMV.MV (Concatenated Measurement Volume - Multiple View)

As previously stated, these methods are not directly applicable to the HandySCAN. For this reason, another approach is here proposed, which introduces a controlled movement of the sensor. In this new approach, four scanning kinematic strategies are defined: CMV.A, CMV.B, CMV.C and CMV.D.

CMV.A and CMV.B are respectively introduced to replace SMV.SV and SMV.MV, while CMV.D is formulated as practical implementation of CMV.MV in the volumetric length measurement error E_{Vol} (section 2.2.6). The distortion error D_{CC}, the flat-form distortion error $D_{Form.Pla}$ and the probing errors conversely, are only evaluated in the SMV (either SMV.SV or SMV.MV) with no CMV.MV counterpart defined by the standard, as previously shown in Table 2. To evaluate the behaviour of these errors under practice-like, unconstrained scanning conditions the fourth strategy CMV.C is introduced as an extension.

CMV.A (Single view)

Also referred to as a "single view" approach, the CMV.A strategy involves moving the instrument along a single, straight linear direction. For simplicity two main translation directions at a fixed working distance are identified:

- Horizontal direction, from here indicated as y_tr
- Vertical direction, from here indicated as x_tr

The CMV.A method is meant to replace the SMV.SV, and so to evaluate the errors isolating the influence of the working distance and of the portion of the laser grid concerned in the acquisition, allowing the evaluation of localized effects. Limiting the degrees of freedom to a single translation prevents the instruments dynamic registration algorithm from compensating for potential errors through multiple overlapping views, thereby exposing the raw performance of the sensors laser grid.

The extents of the translation proposed in this work is less than or equal to twice of the maximum Laser Lines Distance (LLD) in that direction, this to guarantee a good coverage but limiting the number of overlaps.

In the case of HandySCAN the translations limits are:

- $\text{x\_tr} \leq 2 \times \text{LLD}_\text{x} \cong 2 \times 50\ \text{mm} = 100\ \text{mm}$
- $\text{y\_tr} \leq 2 \times \text{LLD}_\text{y} \cong 2 \times 85\ \text{mm} = 190\ \text{mm}$

The concatenated measurement volume (CMV.A:x_tr or CMV.A:y_tr), obtained by translating the scanner along a single direction, does not have a cuboid boundary but a geometry approximated by a truncated pyramid. This shape results from the combination of two effects: the natural pyramidal opening of the instruments field of view and the linear extrusion introduced by the translation (x_tr or y_tr) along a single direction. ISO 10360-13 explicitly allows for a sensor measurement volume that is not parallelepiped in shape, stating that in such cases the subdivision into eight voxels "shall follow that shape to correspond with the parallelepiped case as much as possible" (ISO 10360-13:2021, 6.2.2.3.1).

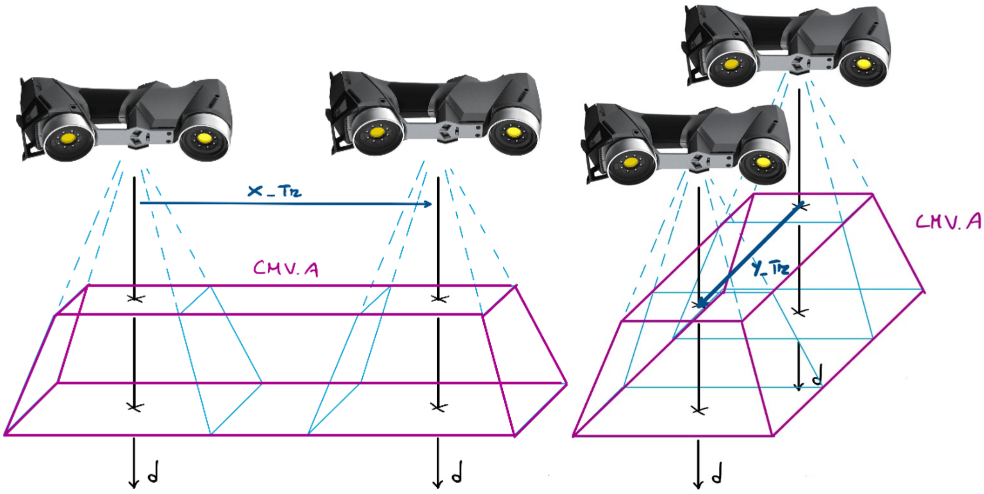

Figure 31. Schematic of the CMV.A strategies, with the translation along the x and y directions.

CMV.B (Multiple view)

This strategy features the registration and fusion of multiple CMV.A measurements taken from different locations and directions, likewise the SMV.MV described in the ISO 10360-13 framework. The objective of this strategy is to include and evaluate the influence of stitching and fusion of multiple scans on the different types of errors.

A key aspect of handheld scanners is the recognition and use of the retroreflective targets applied for instrument position live tracking; the acquired position of those targets, whenever kept fixed through all the measurements, can be directly applied in the registration process, by either performing the registration of the targets or by using the same reference system.

Specifically, in this work to ensure a highly controlled measurement environment and isolate the instruments software capabilities, a set of targets is pre -acquired to establish a stable, global reference system. Since these targets are solidly attached to the measured surface, the resulting individual point clouds are automatically aligned into the global coordinate system and combined by the instruments built -in registration and fusion algorithms.

CMV.C (Free pathway measurement)

The CMV.C strategy, also referred to as "free pathway measurement" consists in moving the instrument freely around the material measure, following a trajectory similar to that adopted in conventional measurement practice. Unlike CMV.A, this approach does not constrain the sensor motion to fixed directions, but the operator moves the sensor along an unconstrained path around the object to obtain a complete surface acquisition, maximizing the coverage, and characterized by multiple overlaps of the laser lines, leveraging on the live registration and fusion algorithms. This method provides an important insight on how the accuracy changes when shifting from the challenging scanning conditions proposed in the CMV.A to a more practice-like approach.

<u>CMV.D (Extended translation)</u>

Unlike CMV.A, CMV.B and CMV.C, which were introduced to replace the SMV.SV, SMV.MV and free-pathway acquisition modes respectively, the CMV.D strategy is designed as implementation of the CMV.MV when measuring volumetric length measurement error E_{vol} that has the objective of assessing the macro-scale accuracy of the CMS and the propagation of registration and concatenation errors across the entire extent of the concatenated measurement volume.

The CMV.D strategy consists of a single-direction translation of the instrument, similar to CMV.A, but with translation length large enough to acquire the entire length of the reference ball beam. As for CMV.A, two directions are defined, CMV.D:x_tr and CMV.D:y_tr, along the same reference axes. Because the translation constraint is removed, a CMV.D acquisition involves a much larger number of overlapping frames along the whole translation and relies extensively on the instruments live registration and fusion algorithm .

2.2.3 Distortion Errors

As defined in the standard and described in the section 1.4.2 , the distortion error D_{CC} quantifies the error of indication when measuring the calibrated distance between the centres of two spheres. Its evaluation is used for isolating the geometric deformations intrinsic to the sensors optical system.

The ISO 10360-13 procedure consists of dividing the measurement volume into 8 adjacent sub-volumes, i.e. voxels, and to position a calibrated ball bar in specific positions so that the spheres are completely within two different voxels. Out the 28 possible positions of the material measure, relative to the voxels' definition, the standard identifies 12 of them mandatory for the performance verification. The relevant aspect is that these positions can be achieved by moving one of either the instrument or the calibrated length, as the focus lies in their relative position.

In this work instead, consistently with the scanning kinematic strategies introduced in section 2.2.2, the distortion errors are evaluated through measurements performed according to the CMV.A, CMV.B and CMV.C strategies, and by using equation (14:

$$D_{cc.j:O3D} = L_{cc,meas} - L_{cc,cal} \tag{14}$$

Where $L_{CC,meas}$ is the measured length, $L_{CC,cal}$ is the calibrated length of the material measure, while j is a qualifier that indicates the measurement strategy type, specifically CMV.A, CMV.B or CMV.C.

The measured length $L_{CC,meas}$ is calculated using Equation 15:

$$L_{cc,meas} = \|C_1 - C_2\| \tag{15}$$

Where C_1 and C_2 are the centres of the two gaussian spheres fitted on the spherical patches corresponding to the calibrated spheres. In the fitting process no filtering is applied, considering in this way the 100% of the points belonging to the two spherical patches, as stated in the Annex B of the ISO 10360-13 "*All the points measured on gauging surfaces according to the rated operating condition of the CMS shall be used for testing the length measuring performance.*"

The CMV.A strategy divides into two different sub-cases depending on the translation direction, i.e. x_tr or y_tr. Considering both movement directions and the 12 positions from the standard, a total of 24 individual measurements are performed as indicated in Table 8. The measurements are taken positioning the instrument correctly with respect to the ball beam. For each position 3 measurements are performed. The maximum value obtained is then compared with the $D_{CC.CMV.A:O3D:MPE}$.

Position	Sphere 1 position in voxel	Sphere 2 position in voxel	k
1:k	1	7	x_tr ; y_tr
2:k	4	6	x_tr ; y_tr
3:k	5	3	x_tr ; y_tr
4:k	8	2	x_tr ; y_tr
5:k	2	4	x_tr ; y_tr
6:k	3	1	x_tr ; y_tr
7:k	3	4	x_tr ; y_tr
8:k	6	8	x_tr ; y_tr
9:k	7	5	x_tr ; y_tr
10:k	6	5	x_tr ; y_tr
11:k	4	5	x_tr ; y_tr
12:k	3	6	x_tr ; y_tr

Table 8. Positions of the calibrated length in the CMV.A. Source: adapted from [2].

The voxel division and the translation directions are also reported in Figure 32.

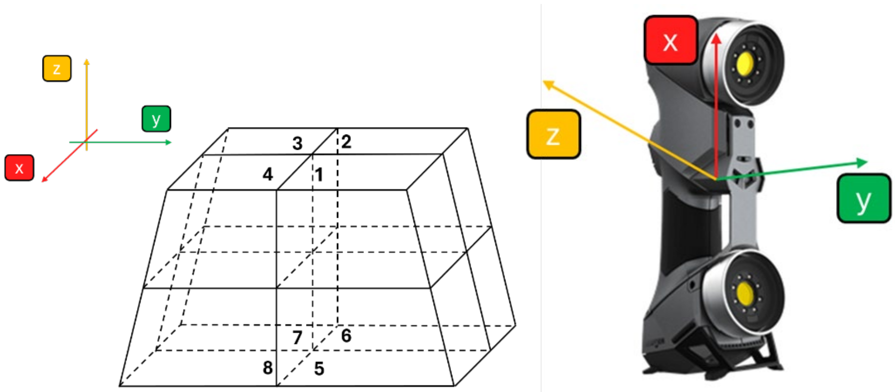

Figure 32. Representation of the voxel numeration in the CMV.A strategies

In the CMV.B case, by using the target positions, for each of the 3 repetitions, all the 24 measurements are fused together and so 3 comprehensive CMV.B errors are obtained, the larger one defines the $D_{CC.CMV.B:O3D:MPE}$.

For the CMV.C strategy, the sensor was moved with a continuous, unconstrained motion around the calibrated artefact, which is positioned horizontally. The same measurement is repeated for a total of three scans and the maximum distortion error is then confronted with the MPE.

Reference artefact and measurement process

In the evaluation of these errors, the ISO 10360-13 refers to the use of a calibrated centre-to-centre distance of a ball bar. However, a calibrated ball beam was used as a substitute in this work. The ball beam described in section 2.1.2, equipped with two metallic matte spheres (sphere 20240409-01 and sphere 20240409-02, positioned respectively in position 1 and 2 of the ball beam), was used as the reference artefact for this test. Prior to the acquisitions, the following scanning parameters were fixed and kept constant throughout all the measurements:

- **Shutter speed:** set to 0.15 ms, in accordance with the default setting defined by the manufacturer as the optimal value for cooperative surfaces under controlled laboratory conditions.
- **Resolution:** set to 0.20 mm, corresponding to the maximum mesh resolution declared by the manufacturer, in order to maximize the point cloud density and the fidelity of the reconstructed geometry.
- **Post-processing filters** (e.g. mesh polishing, hole filling, smoothing) provided by the VXelements software were deactivated, so that the acquired point cloud would reflect the raw performance of the instrument without any algorithmic improvement.

Of fundamental importance is the positioning of the reflective targets, which needs to be constant throughout all the measurements for a correct registration of the acquired data for the "Multiple View" evaluation strategy. For a correct approach the targets must not be applied on the spheres' surfaces as their thickness and adherence to the surface alters the results, or as in the case of the HandySCAN does not generate valid points (data loss represented by a hole). For this reason, the retroreflective targets need to be applied over the ball beam and the near environment.

The ball beam and support assembly is positioned over the vibration proof plane of a CMM (ZEISS Prismo) to reduce the effect of vibrations during the measurements.

In our measurement set up to avoid damaging the Ball Beam surface, apposite covers to fit between the magnetic supports, and over which the targets are stably glued, were 3D printed. These artefacts are kept in the lab to avoid thermal changes, and they are kept still on the ball beam positions during the whole distortion error measurement campaign.

Material Measure requirements

The standard defines two important requirements for the selection of the material measure dimensions, i.e. the calibrated length L_{cal} and the sphere diameter D_{cal}, relative to the longest spatial diagonal of sensor measurement volume L_0, which in our case becomes the longest spatial diagonal of the concatenated measurement volumes CMV.A:k $L_{0:CMV.A}$. Specifically, the adapted requirements become:

- $0.02 \times L_{0:CMV.A} \leq D_{cal} \leq 0.2 \times L_{0:CMV.A}$
- $L_{cal} \geq 0.3 \times L_{0:CMV.A}$

The longest spatial diagonal in the defined "Single View" volumes is found in the CMV.A:y_tr and is equal to 664.17 mm. The requirement on the sphere diameter in the presented set up is verified, as the calibrated spheres diameters are both approximately equal to 38.1 mm which is well within the required range of 13.28mm and 132.83mm. However, the ball beam available in the laboratory only provides calibrated centre-to-centre distances of 199.85812 mm (l_{1-2}) and 399.92798 mm (l_{1-3}); the shorter of these two lengths does not satisfy the length requirement by a small margin, and although l_{1-3} formally satisfies the minima, its physical extent exceeds the transversal dimensions of the narrower cross-sections of the CMV.A volume, preventing its practical use for the single-translation configurations. Given this instrumental constraint, and in the absence of a longer calibrated artefact compatible with the sensors measurement volume, the 199.858 mm nominal length (l_{1-2}) was used as the reference distance for the CMV.A distortion error evaluation. This choice is not fully compliant with the dimensional requirement proposed in section 2.2.4, and this limitation is explicitly acknowledged. This deviation from the proposed requirements should be considered as a methodological limitation of the present work, motivated by the practical availability of calibrated artefacts in the laboratory, and is recommended as a point of improvement for future works.

2.2.4 Probing Errors

As defined in the standard and described in the section 1.4.2 , the probing size and probing form errors are measured on a calibrated sphere with cooperative surface finish, and they are of fundamental importance to understand the local accuracy of the scanner in the acquisition of the point cloud.

Both the probing size and probing form errors are evaluated using two subscripts:

- i identifies the percentile of the acquired point cloud used in the error evaluation: $i =$ All when 100% of the points are retained, and $i = 95\%$ when the point cloud is filtered to keep only 95% of the population, discarding the most extreme 5%, following the procedure described below. The standard requires that the same filtered dataset be used to derive both the probing size and probing form errors for a given percentile.
- k identifies the scanning strategy adopted for the acquisition, i.e. CMV.A, CMV.B or CMV.C strategies defined in section 2.2.1. For the CMV.A strategy, the translation direction (x_tr or y_tr) needs to additionally be specified.

For the "Single View" case the standard provides three evaluations of these errors, which are then used to establish the maximum permissible errors. Consistently with the ISO 10360-13 requirement that the same measurement data used for the distortion error evaluation also be used for the probing errors, the point clouds acquired during the distortion error measurements are reused for this purpose, in particular considering the data relative to Sphere 1, whose position within each of the eight voxels of the concatenated measurement volume is reported in Table 8.

It should be noted that for practical reasons the ball beam was not always positioned as described in Table 8, but in some cases the two spheres 20240409-01 and 20240409-02 occupied inverted positions. For clarity, the actual voxel to sphere correspondence is specified in Table 9. In the probing sphere evaluation with the CMV.A strategy, the reported results are only the one corresponding to the actual sphere 20240409-01, this to be able to consistently evaluate and confront the errors associated with the same spherical calibrated artefact; consequently, the analysis of the probing errors does not covers all the 8 voxels across the 12 positions as listed in Table 8, missing the characterization of voxel 3, and the remaining voxels are sampled with an un uneven number of repetitions. For the purposes of this thesis, this limitation is considered acceptable since the objective is the metrological characterization of the sensor rather than a strict compliance verification. The evenly voxel coverage as described in the standard is recommended as a point of improvement for future works.

Position	Sphere 1		Sphere 2	
	Voxel	Calibrated sphere	Voxel	Calibrated sphere
1	1	20240409-02	7	20240409-01
2	4	20240409-02	6	20240409-01
3	5	20240409-01	3	20240409-02
4	8	20240409-01	2	20240409-02
5	2	20240409-01	4	20240409-02
6	3	20240409-02	1	20240409-01
7	3	20240409-02	4	20240409-01
8	6	20240409-01	8	20240409-02
9	7	20240409-02	5	20240409-01
10	6	20240409-01	5	20240409-02
11	4	20240409-02	5	20240409-01
12	3	20240409-02	6	20240409-01

Table 9. Adaptation of table 8 with the actual voxel to sphere correspondence, the sphere 20240409-01 positioned consistently in the first position of the ball is highlighted.

In addition, an acquisition following the CMV.C strategy is performed on a single sphere, in order to evaluate the probing errors under more representative free-pathway scanning conditions.

The measurement parameters are the same as those reported for the distortion errors evaluations; the only material measure requirement is set on the calibrated diameter $0.02 \times L_{0:CMV.A} \leq D_{cal} \leq 0.2 \times L_{0:CMV.A}$, which has already been verified.

Probing Size Error

The Probing Size Error is calculated with the following equation quantifies the error of indication when measuring the calibrated diameter of the test sphere, and it is derived as the difference between the diameter obtained from an unconstrained, unweighted least-squares (Gaussian) fit to the i-percentile of the point cloud $D_{meas,i}$ and its calibrated value D_{cal}:

$$P_{Sph.Size.i:j:O3D} = D_{meas,i} - D_{cal} \quad (16)$$

Probing Form Error

The Probing Form Error describes the local dispersion and noise intrinsic to the acquired point cloud, and it is defined as the thickness of the thinnest spherical shell, concentric with the fitted sphere, that encompasses the selected percentile i of measured points:

$$P_{Sph.Form.i:j:O3D} = R_{max,i} - R_{min,i} \quad (17)$$

where $R_{max,i}$ and $R_{min,i}$ are respectively the maximum and minimum radial distance, measured from the fitted centre C_i, of the points belonging to the i-percentile set. Being a shell thickness, this quantity is by definition non-negative.

Sphere fitting procedure and optimal spherical shell evaluation

The fitting of a sphere to the acquired point cloud represents a fundamental step in the evaluation of both errors. ISO 10360-13 indicates the use of an unconstrained, unweighted least-squares (Gaussian2) algorithm as the reference association method, while intentionally leaving the procedure for determining the optimal i-percentile shell unspecified.

For the i = All case, the process is straightforward: a single least-squares sphere fit to the complete point cloud directly yields the fitted diameter $D_{meas,All}$and centre C_{All}. The probing size error is then computed directly from $D_{meas,All}$ (Equation (16)), while the probing form error is obtained by calculating the Euclidean distance of every point from C_{All}, and taking the difference between the maximum and minimum of these distances (Equation (17).

The $i = 95\%$ case is more complex, as the standard leaves unspecified both the criterion for identifying which points belong to the retained 95% subset and the procedure for determining the optimal shell fitted to that subset. It indicates only that an admissible approach consists of an initial least-squares association followed by the iterative elimination of the most extreme points, possibly over several iterations, until the desired percentile of the population is retained, with the resulting shell taken as concentric with the final least-squares fit. Following this indication, an iterative fitting procedure was implemented in MATLAB, summarized in Figure 33and described below:

1. An initial least-squares sphere (C_{All}, $\mathrm{D}_{\mathrm{meas,All}}$) is fitted to the complete point cloud, as described above.
2. The radial distance of every point from the current centre is computed, and the corresponding residual with respect to the mean radius is evaluated.
3. Points are ranked by the absolute value of their residual, and the 95% of points with the smallest residuals (considering the absolute value) are retained as the candidate subset, discarding the most extreme 5%.
4. A new least-squares sphere ($C_{current}$, $D_{current}$) is fitted to the retained subset.
5. Steps 2–4 are repeated iteratively, updating both the retained point subset and the fitted centre at each cycle, until the displacement of the centre between two consecutive iterations falls below a fixed tolerance (convergence criterion) or a maximum number of iterations is reached.

Upon convergence, the final centre $C_{95\%}$, radius $D_{meas,95\%}$, and the associated 95% point subset are obtained simultaneously. As in the i = All case, this single result is used to compute both the probing size error and $R_{max,95\%}$, $R_{min,95\%}$ for the probing form error.

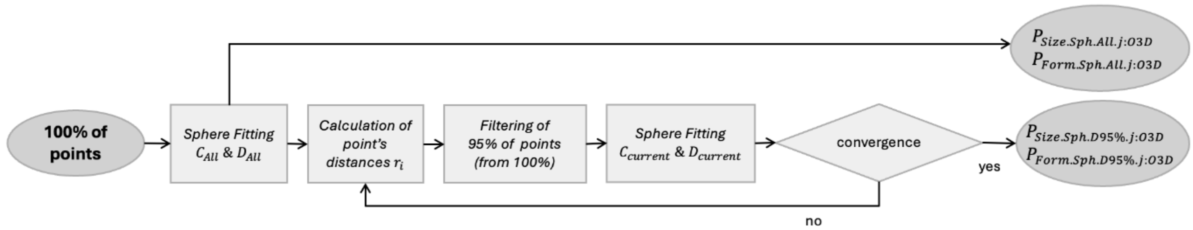

Figure 33. Flowchart algorithm for the evaluation of the 95% of points subset, then used for the evaluation of the Probing Errors

2.2.5 Flat-Form Distortion Error

The flat-form distortion error $D_{Form.Pla}$ is defined in the standard as the minimum distance between two parallel planes that encompasses a given percentile i (either 100% or 95%) of the acquired points obtained by measuring a calibrated reference plane. The error principle is similar to the probing form error but applied to flat surfaces; this error evaluates the local dispersion and noise characteristic of the Optical CMS. This error is calculated through Equation 18:

$$D_{Form.Pla.i:j:O3D} = d_{max,i} - d_{min,i} \tag{18}$$

where $d_{max,i}$and $d_{min,i}$are respectively the maximum and minimum signed distance, measured from the fitted plane, of the points belonging to the i-percentile set, and $j$is a qualifier indicating the measurement strategy adopted, specifically CMV.A or CMV.C, as introduced in section 2.2.2 ; coherently with the previous procedures the CMV.A strategy divides into two separated sub-cases depending on the translation direction, i.e. x_tr or y_tr.

The ISO10360-13 procedure comprises the subdivision of the measurement volume into 8 voxels, and the measurement of the refence plane in 6 different positions of the material measure relative to the defined voxels (as represented in Figure 34), which in the CMV.A case are repeated in both directions.

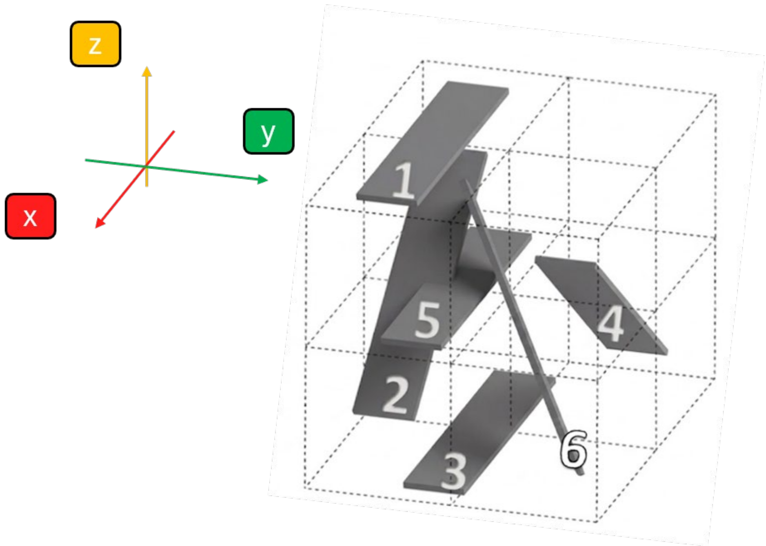

Figure 34. The six positions of the surface reference plane, described in the ISO 10360-13:2021. Source: adapted from [14]

For each position the standard recommends 3 measurement repetitions yielding a total of 36 measurements for the CMV.A strategy and so of 36 flat-form distortion error values; the largest one should be confronted with the maximum permissible error $D_{Form.Pla.i:CMV.A:O3D:MPE}$, which in the case of this work is not clearly defined.

Considering and fusing a single repetition in all the measured positions, a total of three values can be evaluated for the “multiple-view” strategy, CMV.B.

Reference artefact and measurement process

The flat-form distortion error is evaluated using the precision granite surface plate described in section 2.1.2 (Serial Number: 06040425, Mitutoyo), whose certified flatness deviation of 2 µm is negligible with respect to the expected performance of the HandySCAN, thereby satisfying the requirement that the reference artefacts own form deviation not compound with the sensors intrinsic distortion.

The standard defines two dimensional requirements for the test plane expressed relative to the longest distance within the sensor measurement volume L_0, which in this work corresponds, consistently with the approach adopted for the distortion error (section 2.2.3), to the longest spatial diagonal of the concatenated measurement volume $L_{0:CMV.A}$ (664.17mm). These two requirements regard the two dimensions of the surface plane:

- The longer side length $L_{cal,1} \geq 0.5 \times L_{0:CMV.A}$
- The shorter side length $L_{cal,2} \geq 0.1 \times L_{0:CMV.A}$

The granite surface plate described in paragraph 2.1.2 has nominal dimensions of 630 × 400 mm. Both requirements are satisfied with a considerable margin.

Prior to the acquisitions, the following scanning parameters were fixed and kept constant throughout all the measurements:

- **Shutter speed:** set to 1.21 ms, as automatically suggested by the VXelements automatic shutter speed selector for the granite planes surface characteristics. Differently than the ball beam case, the granite surface available in the laboratory is significantly darker and by keeping the default shutter speed value the sensor would result in an underexposure of the sensor; as the dimensions of surface is large enough to contain the whole laser grid the software automatic shutter speed selection is chosen.
- **Resolution:** set to 0.20 mm, corresponding to the maximum mesh resolution declared by the manufacturer.
- **Post-processing filters** (mesh polishing, hole filling, smoothing) were deactivated, consistently with the approach adopted for distortion and probing errors.
- **Reference targets removal:** the retroreflective positioning targets (targets 360) placed on the flat surface for the live tracking system were automatically excluded by the software.

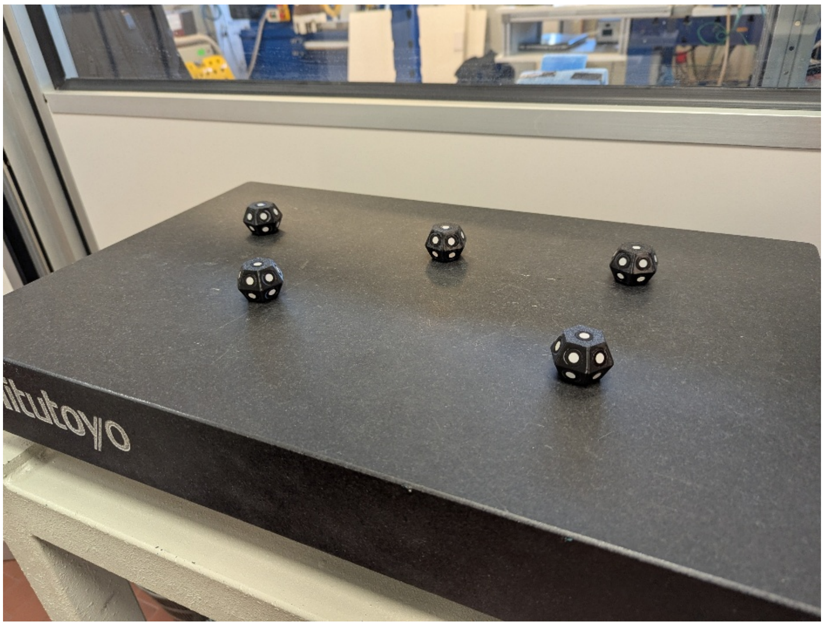

Figure 35. Retroreflective positioning targets placed on the Mitutoyo reference plane for the live tracking system, automatically excluded from the acquired point cloud.

<u>Plane fitting procedure and minimum thickness slab</u>

As for the probing form error, the standard does not identify a specific algorithmic method to evaluate the flat-form distortion error, for this reason a method similar to the probing form error approach is developed.

Specifically, to evaluate the thickness encasing the whole point cloud an unconstrained, unweighted Gaussian least-squares plane is fitted over the acquired data, as average reference plane, the flat-form error is then calculated through Equation (18) considering the maximum and minimum distances from the reference plane (residuals).

For the 95% point cloud subset the same iterative route used for the $P_{Sph.Form.D95\%:j:O3D}$ is applied but considering the centroid G of the PC and the normal vector n of the plane instead of respectively the centre and the radius of the sphere case:

1. An initial least-squares plane (G_{All}, $n_{\mathrm{meas,All}}$) is fitted to the complete point cloud, as described above.
2. The distance of every point from the current plane is computed.

3. Points are ranked by the absolute value of their residual, and the 95% of points with the smallest residuals (considering the absolute value) are retained as the candidate subset, discarding the most extreme 5%.
4. A new least-squares plane ($G_{current}$, $n_{current}$) is fitted to the retained subset.
5. Steps 2–4 are repeated iteratively, updating both the retained point subset and the fitted centre at each cycle, until the displacement of the normal vector between two consecutive iterations falls below a fixed tolerance (convergence criterion) or a maximum number of iterations is reached.

Through this method, the final 95% point subset is individuated as also the reference plane, the minimum and maximum residuals are used to calculate the error.

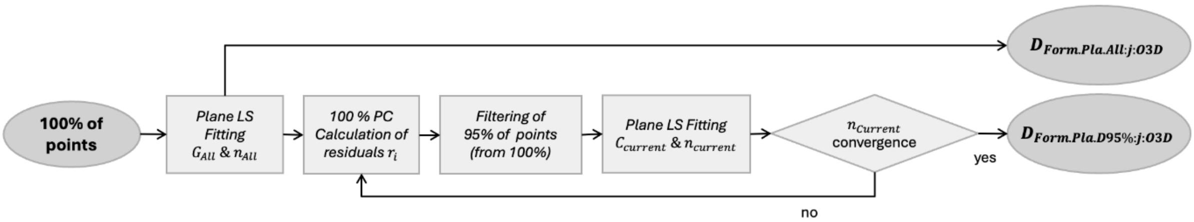

Figure 36. Flat-Form Distortion Error procedure

Another commonly used approach for evaluating the optimal bounding zone enclosing a point cloud (PC), specifically defined for flatness evaluation in standards ISO 1101 and ISO 12781 (Parts 1 and 2) [39–41], is the Minimum Zone (MZ) method, also known as the Chebyshev approximation. Although the MZ method is expressly designed to determine the minimal zone thickness, the Least Squares (LS) method was preferred in this work for the following reasons:

- The MZ method relies on non-linear iterative optimization, which can become computationally challenging and less stable, in particular when combined with subset filtering algorithms (e.g. the 95% point cloud evaluation).
- The LS algorithm is generally faster and more robust.
- The LS method is consistent with the processing approach adopted for the other form error evaluations in this study
- The LS association yields an error bound greater than or equal to the MZ definition thereby providing a conservative evaluation of the flat-form distortion error.

2.2.6 Volumetric Length Measurement Error

The volumetric length measurement error E_{Vol} quantifies the error of indication when measuring calibrated centre-to-centre distances across the full extent of the concatenated measurement volume. Unlike the distortion error D_{CC} which isolates the geometric deformations intrinsic to the sensor's optical system, E_{Vol} is designed to evaluate the macro-scale volumetric accuracy of the CMS, it quantifies how measurement errors propagate through the spatial concatenation as the sensor is moved across the entire measurement volume (ISO 10360-13, 6.4.1). Consistently with this objective, and as introduced in section 2.2.2, E_{Vol} is the only error for which the standard uses the CMV.MV qualifier. In this work, the CMV.D strategy (extended translation) is adopted as the practical replacement of this requirement.

<u>Reference artefact and measurement process</u>

The ball beam described in section 2.1.2, equipped with all six calibrated metallic matte spheres, was used as the reference artefact for this test. Positioning all six spheres simultaneously on the beam allows five calibrated centre-to-centre distances ($l_{1-2}, l_{1-3}, l_{1-4}, l_{1-5}$ and l_{1-6}) to be obtained from a single acquisition. The measurements were carried out by translating the HandySCAN (either along its x direction or y direction) parallel to the ball beam, covering its full length, following the CMV.D strategy. The procedure was repeated independently for both translation directions defined for CMV.D (CMV.D:x_tr and CMV.D:y_tr): for both translation directions three positions, consisting in three different working distances relative to the depth of field, were considered:

- Position 1: close to the working distance z_1 (approximately 20 cm), in the upper voxels' region;
- Position 2: corresponding to the mid-plane separating the upper and lower voxels (approximately 32.5 cm);
- Position 3: close to the maximum working distance z_2 (approximately 45 cm), in the farther voxels

At each of the three positions, the beam was kept approximately centred with respect to the instruments field of view . For each position and each direction, three repeated acquisitions were performed, for a total of 18 measurements, and an overall total of 90 acquired calibrated lengths.

The scanning parameters (shutter speed, resolution, deactivation of post-processing filters) and the target configuration were kept identical to those adopted for the distortion error measurements, as described in section 2.2.3 , in order to ensure consistency across the different error evaluations.

Chapter 3: Shutter Speed Optimization

In this chapter, a method for optimising the shutter speed choice setting of the instrument is presented. The tests were carried out by selecting spheres of different materials and surface finish. Specifically, four cases were taken into consideration:

- A metallic matte sphere
- A metallic shiny sphere
- A glossy sphere (i.e., a billiard ball)
- The same glossy sphere covered with a mattifying coating spray

As explained in detail in section 3.2, a measurement campaign was carried out for each of the selected spheres separately, using the HandySCAN laser systems described in the previous chapter, and testing ten shutter speed values in the scanning procedure. For each of these surface types, an optimal shutter speed range is calculated through the combination of a set of performance metrics calculated on the point clouds. The metrics considered includes metrics for the accuracy of the measurements, such as the probing errors described in Chapter 2, together with other metrics that measure positive characteristics useful for the measurement processes, such as point cloud density and coverage.

In the first section the additional laboratory equipment is described and reported; in particular the description of the spheres used and of the instruments used to characterize the thickness of the mattifying sprayed coating over the glossy sphere. In the second section the detailed measurement procedure, together with shutter speed optimization is described. Finally, in the last section of the chapter, the description and discussion of all the metrics used for the shutter speed optimization are presented.

3.1 Additional Laboratory Instrumentation

In the shutter speed optimization experimental procedure three calibrated spheres were deployed: two calibrated metallic spheres one of which was already described in the section 2.1.2 and one glossy sphere calibrated through the laboratory CMM. Moreover, a preliminary analysis on the thickness of the mattifying spray coating was carried out with the use of a square piece of a silicon wafer, which was half sprayed and left uncoated. The thickness was then evaluated through a confocal microscope (Sensofar S Neox).

3.1.1 Calibrated spheres

<u>Metallic Matte calibrated sphere</u>

The metallic matte sphere (Figure 37, left hand side) deployed in this phase of the project is sphere S/N 20240409-01, already introduced in section 2.1.2, also used in the performance verification. This sphere features a cooperative surface, showing a diffusive reflection. Its calibrated diameter and sphericity, reported in Table 7, are 38.0942 mm and 2.03 µm respectively, with calibration and measurement uncertainties of ±0.99 µm (diameter) and ±1.09 µm (sphericity), both at a coverage factor of K = 2.

<u>Metallic Shiny calibrated sphere</u>

The metallic shiny calibrated sphere S/N AZ140 (Figure 37, right hand side) was deployed as a highly specular, non-cooperative surface case. This sphere was calibrated by an accredited laboratory under certificate No Z140-08152024; the measured diameter is equal to 38.0985 mm, while the sphericity is 0.25 µm. The calibration and measurement uncertainties, both at a coverage factor of K = 2, are ±0.99 µm for the diameter and ±1.09 µm for the sphericity, consistent with those reported for the metallic matte sphere set.

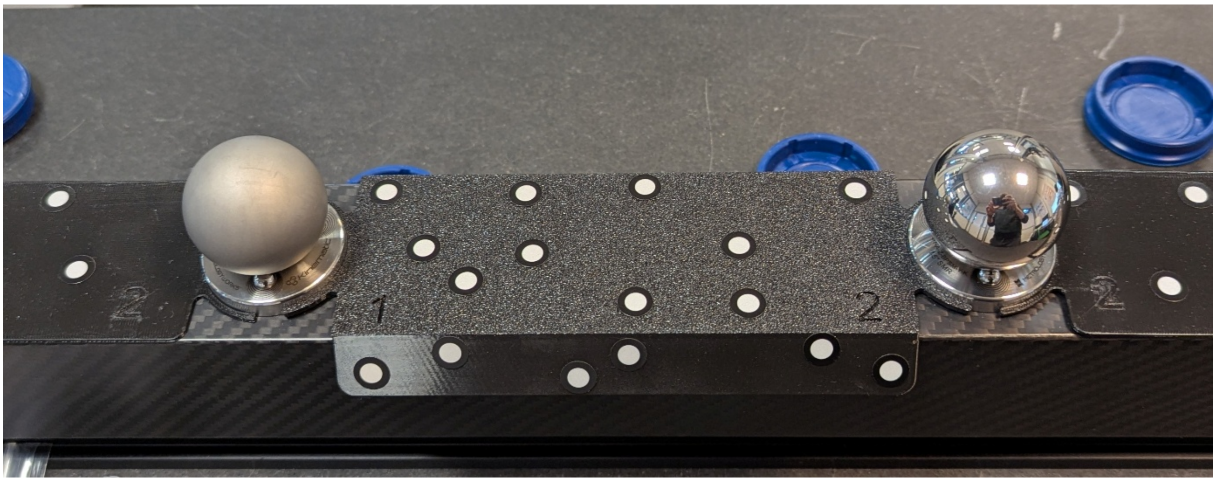

Figure 37. Metallic calibrated spheres, both matte and shiny

Billiard Glossy sphere

The glossy sphere corresponds to sphere 1 of a ball beam assembled in the laboratory using five billiard balls (hereafter referred to as the billiard ball beam). This ball beam was calibrated using the ZEISS Prismo CMM in a scanning mode (Figure 38). The measured diameter is 57.2954 mm and the sphericity is 12.5 µm. The measurement uncertainty of the ZEISS Prismo CMM, on the order of 4 µm, is at least one order of magnitude smaller than the expected probing errors of the HandySCAN. It is therefore considered negligible with respect to the accuracy required for using this sphere as a reference in the shutter speed optimization campaign.

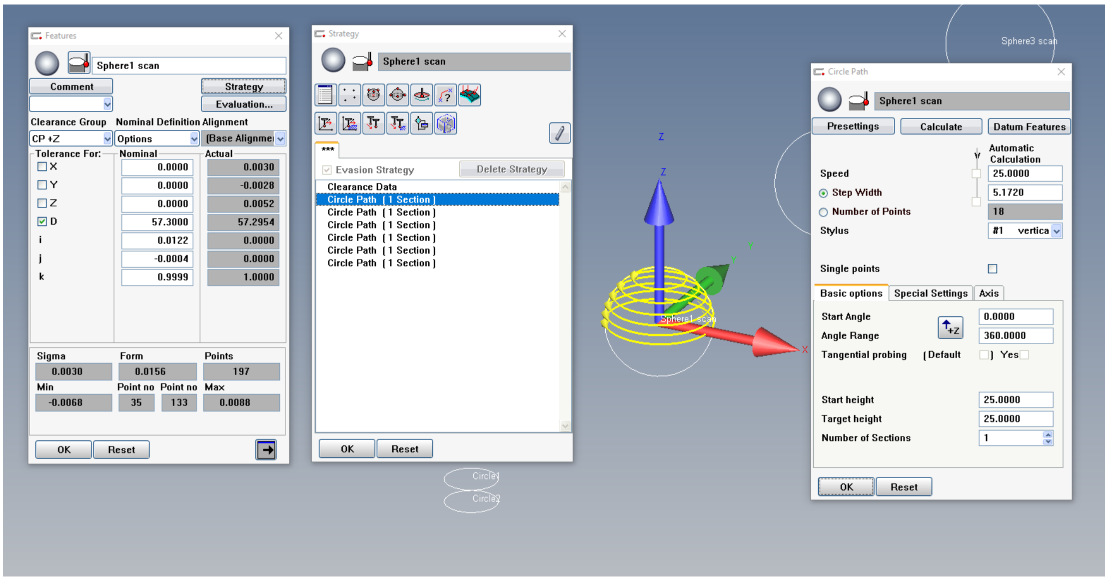

Figure 38. Glossy Billiard Ball beam scanning, CMM ZEISS Prismo scanning program

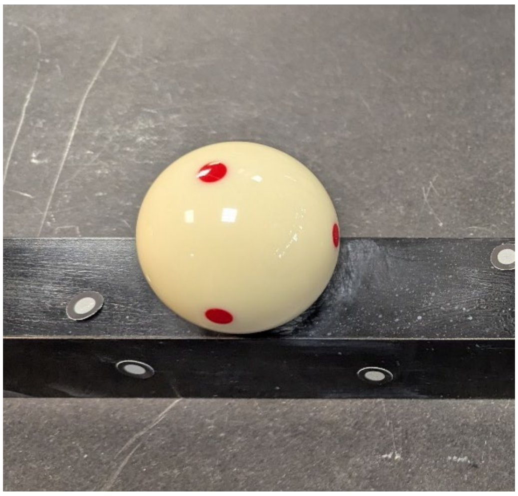

Figure 39. Billiard glossy sphere

Billiard mattified sphere

The same sphere 1 of the billiard ball beam after the measurements performed on the uncoated sphere, was mattified with the use of a mattifying spray applied from about 20-30 cm from the surface. The maximum thickness of the mattifying coating $t_{coating}$ was estimated to be equal to 5.2 ± 0.6 µm, as detailed in the section 4.2.1 . The diameter of the billiard ball was then corrected by adding the contribution of the mattifying layer to the sphere diameter ((19) resulting in a corrected diameter of 57.3058 mm

$$D_{mattified\ sphere} = D_{billiard\ sphere} + 2 \times t_{coating} \quad (19)$$

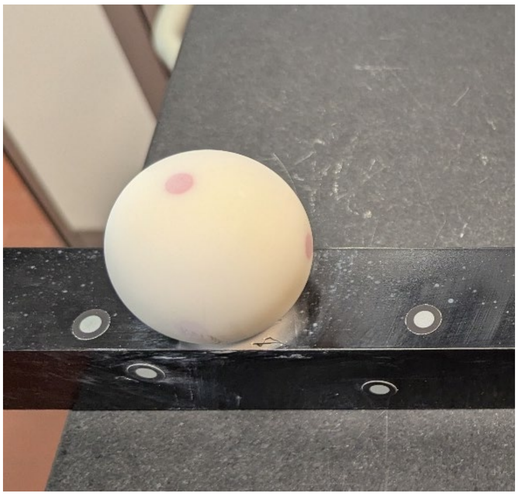

Figure 40. Billiard glossy sphere mattified with a mattifying spray

Sphere	Surface Finish	Sphericity / µm	Sphere diameter / mm
Metallic Matte S/N 20240409-01	Cooperative	2.03	38.0942
Metallic Shiny S/N AZ140	Non-cooperative	0.25	38.0985
Billiard Glossy Sphere 1 Biliard ball beam	Non-cooperative	12.5	57.2954
Billiard Mattified Sphere 1 Billiard ball beam+coating	Cooperative	-	57.2954 + 0.0104

Table 10. Spherical artefacts used in the shutter speed optimization campaign.

3.1.2 Supporting material for the coating thickness evaluation

Mattifying spray

The process of glossy sphere mattifying was achieved using a commercial permanent spray, the HELLING 3D Laser Scanning spray (Art. 119.990.001, HELLING GmbH, Heidgraben, Germany) (Figure 41). According to the manufacturer, this spray creates a homogenous fine-grain white coating that reduces the specular reflection on the object being scanned. The product was shaken before its use and then applied from 20/30 cm from the glossy sphere's surface, rotating manually the sphere to obtain a uniform coating. The nominal coating thickness of the coating is not specified by the manufacture as it also strongly depends on how it's used; for this reason, a preliminary coating thickness characterization was performed over a silicon wafer substrate, as indicated in the following.

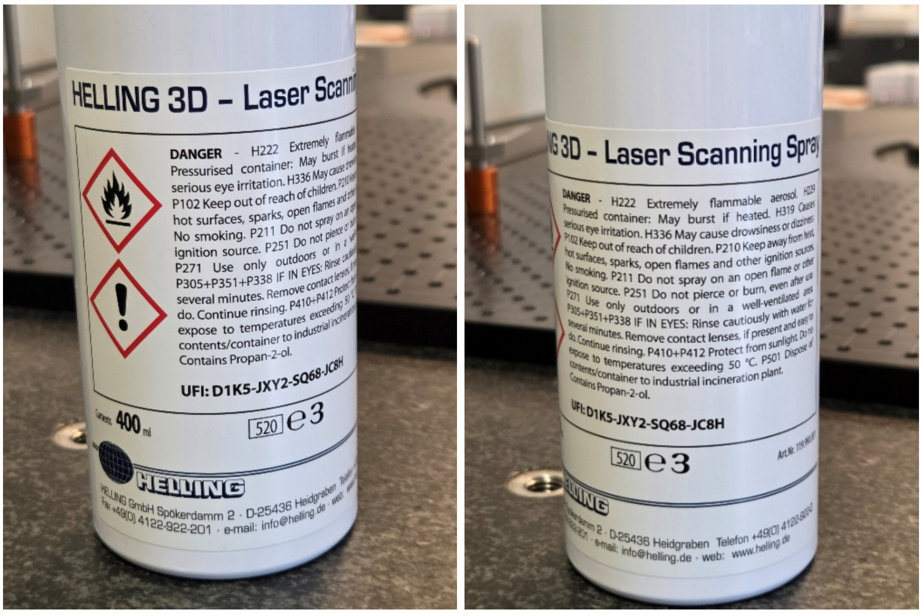

Figure 41. HELLING 3D Laser Scanning Spray.

Silicon wafer

To evaluate the thickness of the mattifying coating, the polished side of a square silicon wafer sample was used as substrate. Silicon wafers are characterized by an extremely high intrinsic flatness, making them a suitable geometric reference to isolate the coating thickness from substrate form deviations. Half of the wafer surface was masked with paper tape prior to spraying, so that a coated and an uncoated region could be obtained on the same sample and measured under identical conditions. The coating was obtained by spraying the half-masked wafer from about 30 cm for only few seconds. The tape was then carefully removed leaving the other half uncoated (Figure 42). The mattifying coating thickness characterization was then performed by means of a Confocal Microscopy (Sensofar S Neox) through which a set of 9 measurements in 3 different positions was performed.

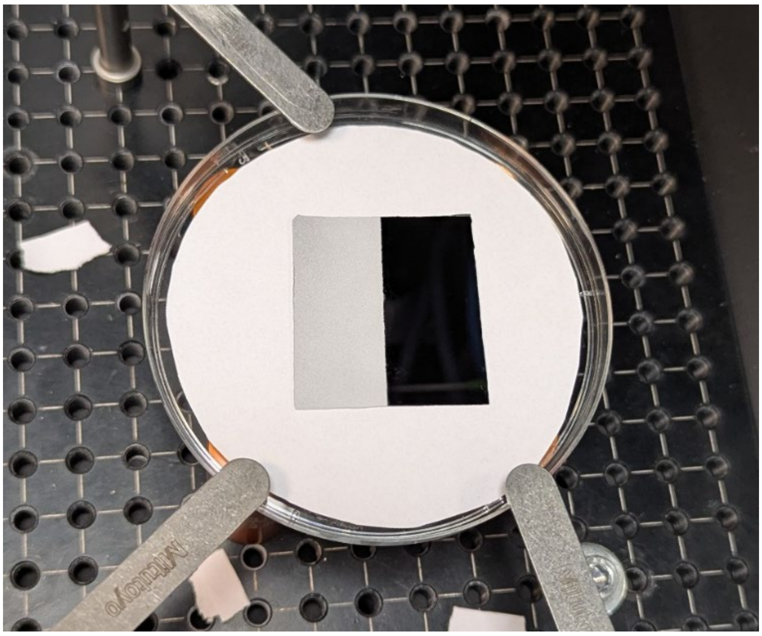

Figure 42. Silicon wafer sample with the left half coated with a mattifying spray and the right half uncoated.

<u>ZEISS O-Inspect 3/2/2 – Confocal chromatic sensor</u>

For the evaluation of the coating thickness, an analysis was carried out by means of the confocal chromatic sensor (Dot-Scan). This sensor is mounted on the ZEISS O-Inspect 3/2/2 coordinate measuring machine, a multi-sensor coordinate measuring system. Its working principle is based on chromatic dispersion of white light: different wavelengths are focused at different distances from the lens, so that only the wavelength in focus at the target surface is detected, allowing a contactless distance measurement. The declared metrological performance, according to ISO 10360-8:2013, is reported in Table 11.

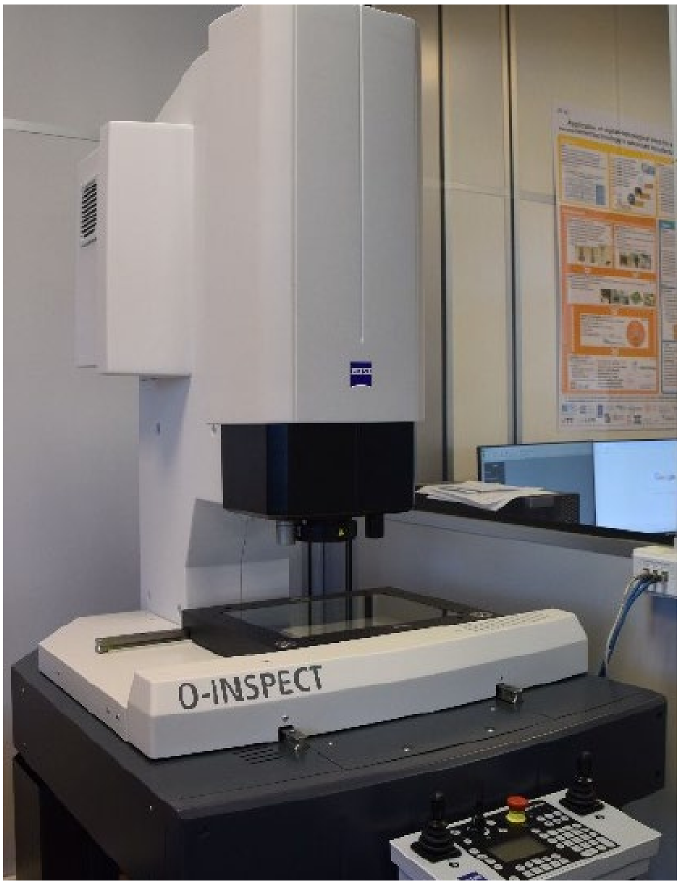

Figure 43. ZEISS O-Inspect 3/2/2

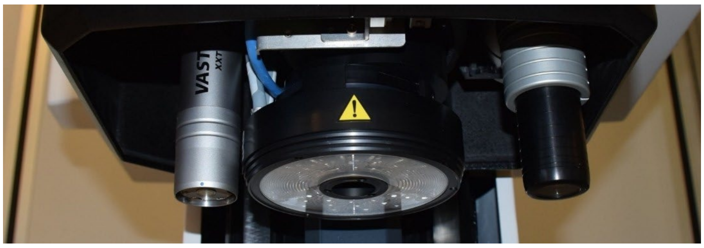

Figure 44. Zeiss O-Inspect 3/2/2 measuring head. From left to right: contact measuring probe housing, telecentric camera with illumination system, and confocal chromatic sensor.

Maximum Permissible error			
one-dimensional length measurement error	E(1D)	2.2 + L/150	MPE expressed in µm, L in mm
Probing error	P	5	µm

Table 11. Metrological performances of the confocal chromatic sensor mounted on the ZEISS O-Inspect 3/2/2

The system allows scanning acquisitions at rates up to 1000 pts/s, with a measuring range of 3 mm, a working distance of 21.5 mm, a resolution of 36 nm, and a measuring spot diameter of 9 nm. The maximum tilt angle for surface detection is ±24°.

Sensofar S Neox: Optical Confocal Microscope

To measure the thickness of the mattifying layer the 3D optical profiler Sensofar S Neox (Figure 45), available at the T.E.S.I. metrology laboratory of the University of Padua. This instrument is used for surface topography measurements, that can be performed according to three different optical principles: confocal microscopy (CM), focus variation (FV) and white light interferometry (WLI). Among these methods, the confocal microscopy was employed for the thickness analysis. The instrument is positioned on an anti-vibration table to reduce the impact of vibrations caused by its motorized sample-movement system. Table 12 reports the main technical specifications of the instrument related to the confocal principle, based on the optical objective employed. For this measurement, the 20× objective was used.

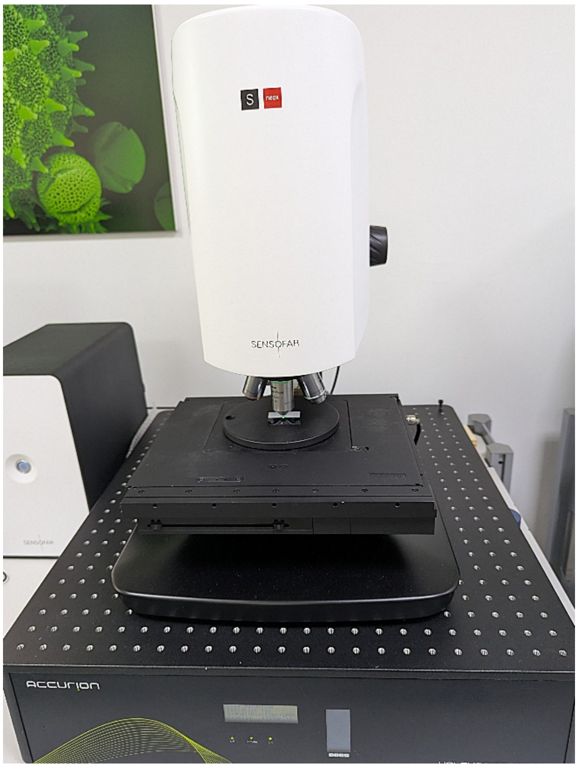

Figure 45. Sensofar S Neox

Objective magnification	2.5×	20×	100×
Working Distance /mm	6.5	4.5	1.0
Numerical Aperture	0.075	0.45	0.9
Field of View / µm	7016×5280	636×477	127×95
Spatial Sampling / µm	5.16	0.83	0.17
Lateral Resolution / µm	1.87	0.31	0.15
Vertical Resolution / µm	300	8	2
Maximum Slope / °	3	21	51

Table 12. Technical specifications of the Confocal Sensor for each objective magnification.

3.2 Design of Experiment and Optimization method

The shutter speed (t_{SH}), as already introduced in section 2.1.1 , is the only user-controllable hardware scanning parameter of the HandySCAN, which controls the exposure of the optical sensor. The amount of light reflected to the cameras depends both on the shutter speed value and on the reflective behaviour of the scanned surface, which in turn depends on its material and finish (section 1.3).

Through its software interface (VXelements), the instrument is able to suggest an optimal shutter speed value depending on the surface type; this automatic method, however, presents a strong limitation with respect to the optimization pursued in this work: it only identifies the shutter speed level that improves the exposure of the overall laser grid (as shown in Table 3), without considering the actual effects on the resulting point cloud. The present work follows a different approach: it focuses instead on the evaluation of an optimal shutter speed range that improves the overall set of evaluation metrics computed directly on the acquired point clouds. The chosen optimization metrics, described in detail in section 3.2.3 , are:

- Probing errors for the accuracy
- Spherical coverage
- Point cloud density.

3.2.1 Design of Experiment

The shutter speed optimization campaign is structured as a single-factor Design of Experiment (DoE), in which the shutter speed t_{SH} is the only controlled experimental factor.

This single-factor DoE is repeated independently for each of the four surface conditions listed in Table 9 (metallic matte, metallic shiny, billiard glossy, billiard mattified). This design was chosen to highlight the influence of this parameter on the point cloud characteristics and the possible differences between cooperative and non-cooperative surface types, following a straightforward and simplified approach. More complex design are discussed in the future outlooks.

<u>Factor and levels</u>

The shutter speed is varied across ten levels, covering the full operative range of the HandySCAN SILVER (0.10 – 8.00 ms):

Shutter Speed Levels / ms									
0.10	0.15	0.20	0.30	0.40	0.50	1.25	2	5	8

Table 13. Shutter Speed Levels of the single factor DoE

The interval space between the levels is not uniform, with a higher concentration of levels as the t_{SH} gets closer to the lower end. This choice is due to two main reasons: first, preliminary observations show that the performance metrics change more rapidly at lower shutter speed values; second, the manufacturer suggests using low values of shutter speed whenever possible to improve the acquisition speed. Moreover, this choice reflects the characteristics of the slider in the software, i.e. the shutter speed does not change linearly moving the slider. The manufacturers default value of 0.15 ms is included as one of the ten levels, so that the default shutter speed can be directly compared with the optimized result.

For each shutter speed level, 5 repeated acquisitions were performed, for a total of 50 measurements per surface case. The order of execution of all these measurements was randomized to prevent the introduction of systematic drift from a possible systematic variation of the operator manual movement of the HandySCAN; specifically, a randomized complete block design was adopted: the 5 repetitions were treated as 5 different blocks, within which the 10 shutter speed levels were randomized independently.

Movement type

All the acquisitions were performed using an articulated, free-hand scanning movement along a semicircular trajectory; in each measurement the trajectory is followed twice, forward and back, in order to achieve a higher repeatability and to keep the scanned area approximately constant across the runs. Differently from the performance verification stage, this choice of movement is made to represent a more general, standard scanning practice.

The working distance between the instrument and the sphere is kept fixed at the mid-plane position of the depth of field (approximately 32.5 cm).

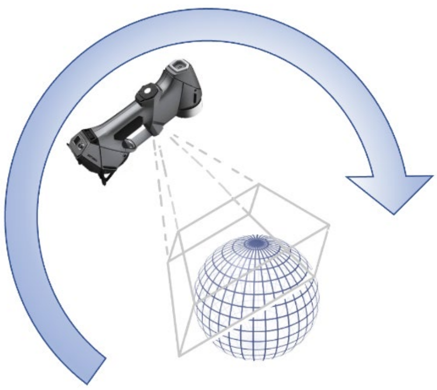

Figure 46. Kinematic strategy adopted in the DoE measurements

3.2.2 Acquisition and Pre-processing Procedure

For every measurement of the DoE, only the shutter speed is varied according to the values in Table 13. All the other scanning parameters are kept fixed, consistently with the settings adopted in Chapter 2: the resolution is set to 0.20 mm, corresponding to the maximum mesh resolution computed by the software, and the post-processing filters (mesh polishing, hole filling, smoothing) provided by the VXelements software are deactivated, so that the acquired mesh reflects the raw performance of the instrument at each shutter speed level. At the end of each run, the acquired mesh is exported and manually cleaned in CloudCompare: the sphere is isolated from the rest of the scanned scene, removing the supporting base and any surrounding surface not belonging to the sphere itself. From the resulting mesh, the point cloud used for the subsequent analysis is extracted by taking the coordinates of the mesh vertices and is saved in an ASCII text format. The cleaned point cloud of each run constitutes the input to the performance metrics presented in section 3.2.3 .

3.2.3 Performance metrics

The quality of these point clouds (associated to the calibrated artefacts listed in Table 10) is then evaluated through a set of metrics. These metrics are introduced to quantify how accurate the acquired data is in representing the reference sphere and how complete the acquired surface is when measuring with the same movement.

For the point cloud accuracy, the metrics considered are the probing errors already introduced in the previous chapter. However, a complete analysis of the acquired data quality requires also an evaluation of the sphere surface completeness: a point cloud could in fact be accurate while still being incomplete, acquiring only a small portion, presenting holes or showing an uneven distribution of points. This is particularly evident for low shutter speed values, which often results in a smaller amount of acquired points due to an underexposure of the sensor. For this reason, the coverage and point density metrics are introduced. The surface coverage indicates the percentage of the total theoretical area of the sphere captured by the HandySCAN, while the point cloud density measures the number of points per unit area.

The k-Nearest Neighbours (kNN) approach is chosen to estimate the surface coverage and density without requiring an explicit reconstruction of the surface mesh, relying instead on the local spacing between neighbouring points. For every point of the cloud, the distances to its k nearest neighbouring points are computed; the mean of these k distances defines the local resolution around that point, while the distance to the k-th (farthest) neighbour is used to approximate the local neighbourhood as a circle of that radius r_i (Figure 47). The local point density is then obtained as the ratio between the number of neighbours k and this local neighbourhood area, and, conversely, the local area contribution A_i of each point is obtained by dividing the same neighbourhood area by k. Summing these local area contributions over the entire point cloud gives an estimate of the total measured area A_{meas}, which, compared to the theoretical sphere area $A_{th} = 4\pi R^2$, yields the surface Coverage as their percentage ratio. The point cloud Density is instead obtained as the mean of the local densities computed at every point, and the overall Resolution as the mean of the local spacings.

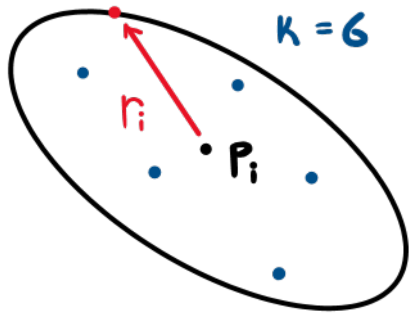

Figure 47. Calculation of the area A_i associated with a single point

This procedure is implemented in a MATLAB function called SphereArea_kNN.m. Given the point cloud as input, the function performs a k-nearest-neighbour search using MATLABs knnsearch, with a default neighbourhood size of $k = 6$, chosen as it corresponds to the natural number of neighbours in a regular hexagonal packing of points on a 2D surface. As for the probing error functions, the fitted centre and radius of the reference sphere can either be provided directly as inputs or computed internally through a call to SphereFitISO; in this work the pre-computed values are always passed, consistently with the approach adopted for the other metrics.

In this thesis the kNN approach is chosen rather than a Delaunay meshing method, because despite being computationally slower and being based on an estimate area rather than an explicit reconstruction, it does not require any external threshold parameter to be tuned separately for each surface condition.

3.2.4 KPI Definition and Optimization

The objective of the performance metrics introduced in the previous paragraph is to find an optimal shutter speed, or range, for each surface condition that can improve the quality of the point cloud in terms of accuracy and noise but also improve the data completeness in terms of coverage and point cloud density; in order to do that, these metrics need to be combined into a single aggregated Key performance Index (KPI) or also referred to as score.

For this purpose, a tool was developed that, given one of the four surface conditions and the values of the metrics computed at each shutter speed level, combines them into a single KPI.

The tool leaves the user free to choose which metrics to include and which priority to assign to each of them, so the optimization can be adapted to different measurement needs.

The tool normalizes and adapts the metric values computed on the acquired data, into dimensionless indices compatible with each other defined so that an increase in the index always corresponds to an improvement in performance. These indices are then linearly combined into a single Score, computed as the weighted sum of the individual indices. The relative weight assigned to each metric is determined through the Modified Digital Logic (MDL) method, further detailed in "Metric Weighting and Score Calculation” below.

For the KPI results reported in the section 4.2, the metrics considered are the probing errors evaluated considering the 95th percentile and the coverage evaluated through the kNN approach. The choice of using the probing errors evaluated on the 95th percentile rather that the 100% was made to limit the influence of isolated noisy points on the resulting Score. Although the point density is introduced and discussed in the results (section 4.2), it is not included in the score evaluation, the reasons for this choice, based on the experimental results obtained for the four surface conditions, are discussed in section 4.2.6 .

<u>Normalization and definition of the indices</u>

Since the selected metrics are expressed in different units and magnitudes, each of them is normalized to the [0, 1] range before being combined. For a given metric, the normalization uses the minimum and maximum values observed across all shutter speed levels of a given surface, and depends on whether the metric is a decreasing or an increasing property. For each metric k, $x_k(t_{SH})$ indicates the value obtained at a given shutter speed level, while $x_{k,min}$ and $x_{k,max}$ represent the lowest and highest values recorded for that same metric over the full set of shutter speed levels tested on the surface in question

For decreasing properties, where a lower value corresponds to a better performance ($P_{Sph.Form}$ and $P_{Sph.Size}$), the index is defined as:

$$I_k(t_{SH}) = 1 - \frac{\mathrm{x_k(t_{sh})} - \mathrm{x_{k,min}}}{\mathrm{x_{k,max}} - \mathrm{x_{k,min}}} \tag{20}$$

For increasing properties, where a higher value corresponds to a better performance (Coverage and Point Density), the index is instead defined as:

$$I_k(t_{SH}) = \frac{x_k(t_{sh}) - x_{k,min}}{x_{k,max} - x_{k,min}} \tag{21}$$

With both definitions, the resulting index I_k is bounded between 0 and 1, and a value close to 1 always corresponds to the best observed performance, for every metric.

<u>Metric Weighting and Score Calculation</u>

Not all metrics are equally relevant to the optimization, so the user can assign a priority to each one before the Score is computed: a metric can be excluded (priority 0), or assigned priority III (low), II (medium), or I (high). The weight w_k of each metric k is then obtained through a Modified Digital Logic (MDL) procedure [42], a concept adapted from material selection literature for this application. Every pair of selected metrics is compared, assigning a pairwise comparison value:

- if the two metrics share the same priority, the pair is assigned (1-1);
- if one metric is more important than the other (they differ by one level of priority), the pair is assigned (2-1);
- if one metric is much more important than the other (they differ by two levels of priority), the pair is assigned (3-1).

Summing and normalizing these pairwise comparison values give the final weights w_k, which sum to unity. As the weight are defined, the overall Score for each shutter speed level can be computed as:

$$Score(t_{SH}) = \sum_k w_k \times I_k(t_{SH}) \tag{22}$$

Since every $I_k(t_{SH})$ is between 0 and 1 and the weights sum to unity, the Score also stays between 0 and 1, in which values closer to 1 mean better overall performance. For each shutter speed level, the mean score over the 5 repetitions (section 3.2.1) is computed and used as reference value, while the standard deviation of the 5 individual scores gives an indication of the experimental variability at that t_{SH}.

A second-order polynomial is fitted on the mean score values in function of the shutter speed: if the fitted parabola is concave and its vertex falls inside the parameter range, the vertex is then taken as the optimal shutter speed t_{SH}^*; otherwise, the level with the highest observed Score is reported as the best available operating point. Besides this single value, an optimal range is also defined as the interval of t_{SH} where the fitted Score stays within a fixed tolerance, equal to 0.05 score points, from its maximum, so the user gets an optimal interval instead of a single value. The choice of a fixed tolerance is made to allow direct comparison across the 4 surfaces.

Furthermore, as the optimal shutter speed t_{SH}^* is obtained from a parabolic fit of the mean score at each level, its value depends only on these mean values without considering the variability observed across the 5 repetitions. To evaluate how sensitive t_{SH}^* is to this experimental variability, a Monte Carlo (MC) simulation is performed, to serve as a primary validation of the method described above. The simulation consists of 1000 iterations, which create for each t_{SH} level a synthetic set of points normally distributed around the mean score and with standard deviation equal to the experimental standard deviation observed across its 5 repetitions. At each iteration, a new parabolic fit is then computed on this synthetic dataset, following the same procedure described above, and the corresponding optimal shutter speed $t_{SH,MC,i}^*$ is extracted and stored.

However, not every iteration produces a valid synthetic $t_{SH,MC,i}^*$: those simulations that produce convex parabolas or show an optimal shutter speed external to the HandySCAN physical range are discarded, since they do not define a meaningful value for t_{SH}^*. The number of valid simulations out of the 1000 total is reported as an indicator of how reliably the score peak can be identified with the Monte Carlo simulation: a high number of discarded simulations indicates that the experimental noise, relative to the curvature of the fitted parabola, is large enough to make the position of the maximum uncertain, and is explicitly reported alongside the results as an indication of the reliability of the estimate.

The resulting set of valid simulations produces a distribution of simulated optimal shutter speed values, whose median is taken as the final optimal value $t_{SH,MC}^*$. From this distribution, a 68% confidence interval (± one standard deviation around the median) is reported, providing an estimate of how reliably t_{SH}^* can be identified given the measurement scatter observed in the experimental campaign. A narrow confidence interval indicates that the optimal shutter speed is well defined and stable with respect to experimental noise, while a wide interval suggests that the Score curve is relatively flat around its maximum, and that several shutter speed values in that range would yield comparable performance.

An alternative of defining no-valid iterations to discard, would be to consider, for each of the 1000 synthetic curves, the maximum fitted score value within the tested range. This method was not adopted, since it would introduce an artificial accumulation of results exactly at the range boundaries, not representative of a genuine estimate of the Score peak.

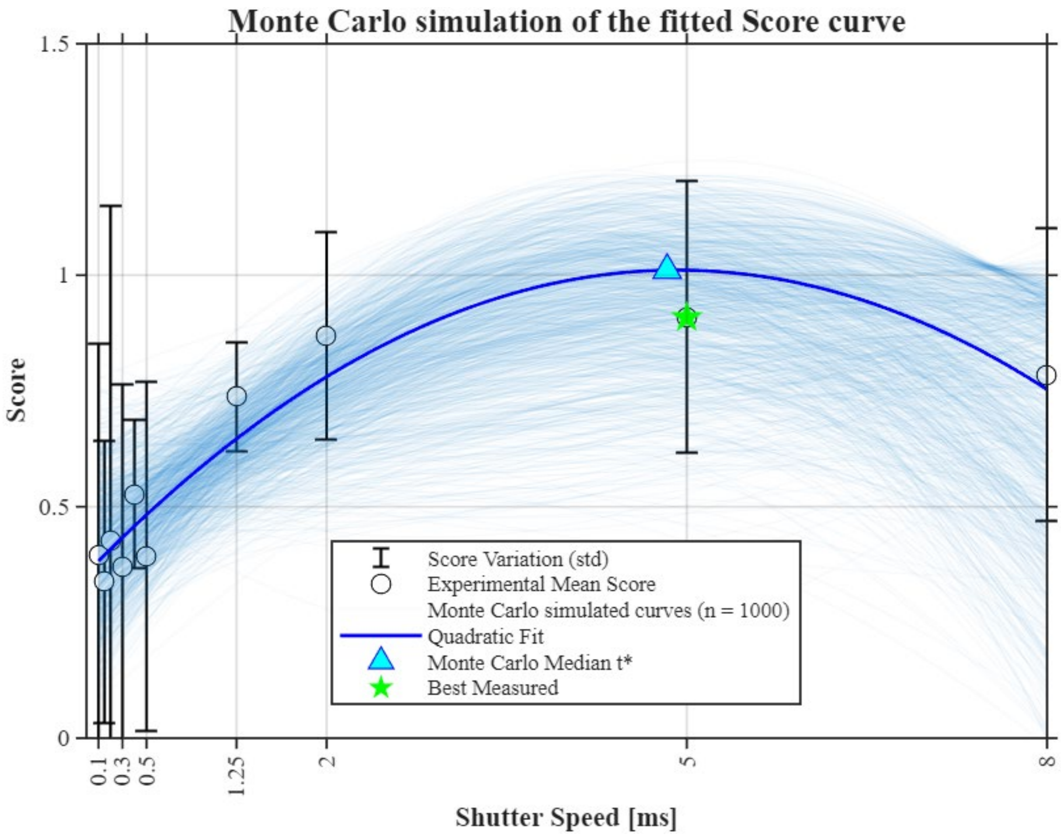

Figure 48. Monte Carlo simulation of the fitted Score curve (from the metallic shiny sphere results), showing experimental mean Score values (circles), the quadratic fit (blue line), the 1000 simulated fitted curves (light blue band), the Monte Carlo median optimal shutter speed $t^*_{SH,MC}$ (triangle), and the best measured value (star)

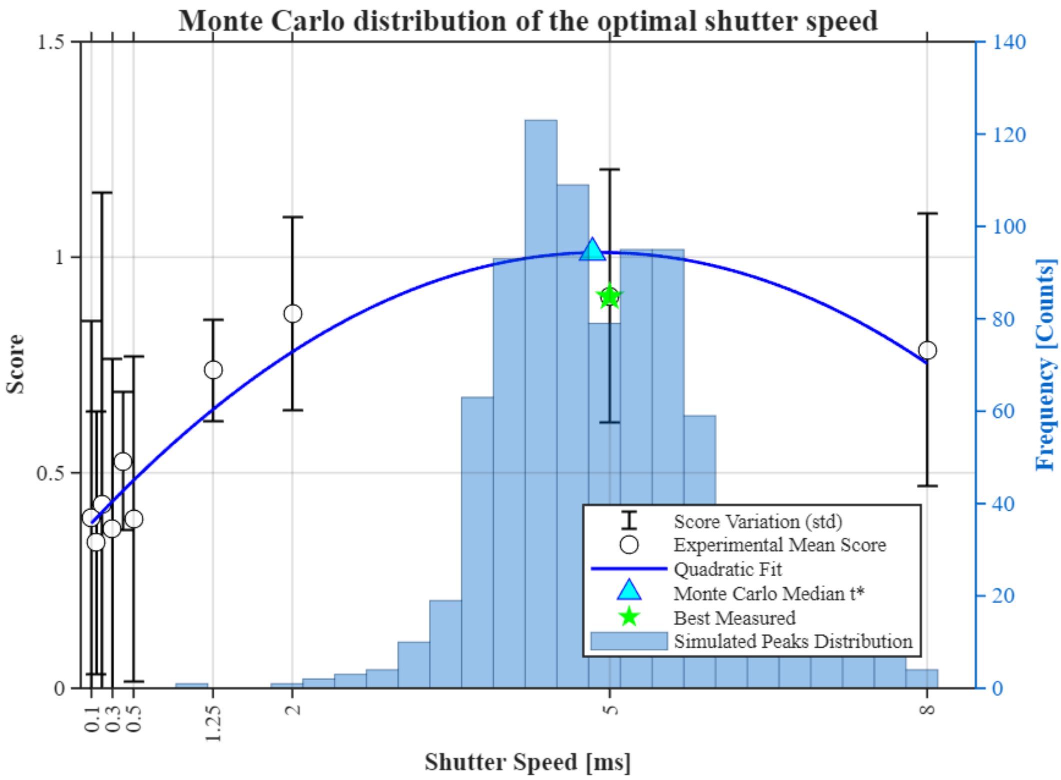

Figure 49. Monte Carlo distribution of the optimal shutter speed (from the metallic shiny sphere results), showing the quadratic Score fit (blue line), experimental mean values (circles), the best measured value (star), and the distribution of the 1000 simulated optimal shutter speed values (histogram, right axis)

Chapter 4: Results and Discussion

In this chapter the experimental results are presented and discussed. In the first section the measured errors of the HandySCAN performance verification are reported, according with the procedure proposed in Chapter 2: . In the second section, the experimental results obtained from the DoE campaign described in Chapter 3: are reported and discussed, together with the results of the mattifying coating thickness characterization.

4.1 Performance verification results of the HandySCAN SILVER

4.1.1 Distortion Errors

The distortion error D_{CC} was evaluated according to the procedure described in section 2.2.3, using the calibrated ball beam equipped with spheres 20240409-01 and 20240409-02 (calibrated distance l_{1-2}= 199.85812 mm). The results are reported separately for the CMV.A, CMV.B and CMV.C scanning strategies.

Distortion errors - CMV.A (Single View)

For the CMV.A strategy, a total of 72 individual distortion error values were obtained (12 positions × 2 directions × 3 repetitions). Table 14 and Table 15 report all the individual $D_{CC.All}$ values for every position, separately for the x_tr and y_tr directions.

Position	$D_{CC.CMV.A:x_{tr}:O3D}$ / mm		
	Rep 1	**Rep 2**	**Rep 3**
1	0.17310	0.15727	0.16105
2	0.14432	0.15530	0.15996
3	0.17327	0.16022	0.16268
4	0.16629	0.15178	0.15093
5	0.17141	0.18094	0.16997
6	0.15886	0.18333	0.16604
7	0.16315	0.17800	0.16792
8	0.21140	0.15760	0.16550
9	0.17596	0.17016	0.17805
10	0.14489	0.18298	0.22266
11	0.14216	0.12861	0.15766
12	0.17184	**0.23873**	0.18251

Table 14. Individual D_CC values obtained for the 12 positions of the CMV.A:x_tr distortion error test, over the 3 repetitions.

Position	$D_{CC.CMV.A:y_{tr}:O3D}$ / mm		
	Rep 1	**Rep 2**	**Rep 3**
1	0.17362	0.18928	0.17659
2	0.15106	0.18262	0.16127
3	0.16736	0.16593	0.17170
4	0.15693	0.16097	0.16329
5	0.20255	0.18863	0.18302
6	0.17313	0.16452	0.17314
7	0.16098	0.17764	0.16790
8	0.16921	0.16677	**0.20884**
9	0.18811	0.16305	0.18776
10	0.14558	0.20375	0.16261
11	0.13549	0.14250	0.13784
12	0.15911	0.13682	0.16268

Table 15. Individual D_CC values obtained for the 12 positions of the CMV.A:y_tr distortion error test, over the 3 repetitions.

The largest value observed for the distortion error for the CMV.A strategy is equal to 0.23873 mm and is found in the twelfth position for the x_tr translation direction. The main values are represented in Table 16. It can be observed that all the individual $D_{CC.CMV.A}$ values are positive, indicating a systematic overestimation of the calibrated length rather than a random dispersion around the nominal value.

Direction	**Minimum distortion error / mm**	**Maximum D_{CC} / mm**
x_tr	0.129 Position 11	0.239 Position 12
y_tr	0.135 Position 12	0.209 Position 8

Table 16. Range of the $D_{CC.CMV.A}$ for x_tr and y_tr directions, across all the measurements

The mean values calculated on the three repetitions separately for the translation direction and positions are plotted in Figure 50.

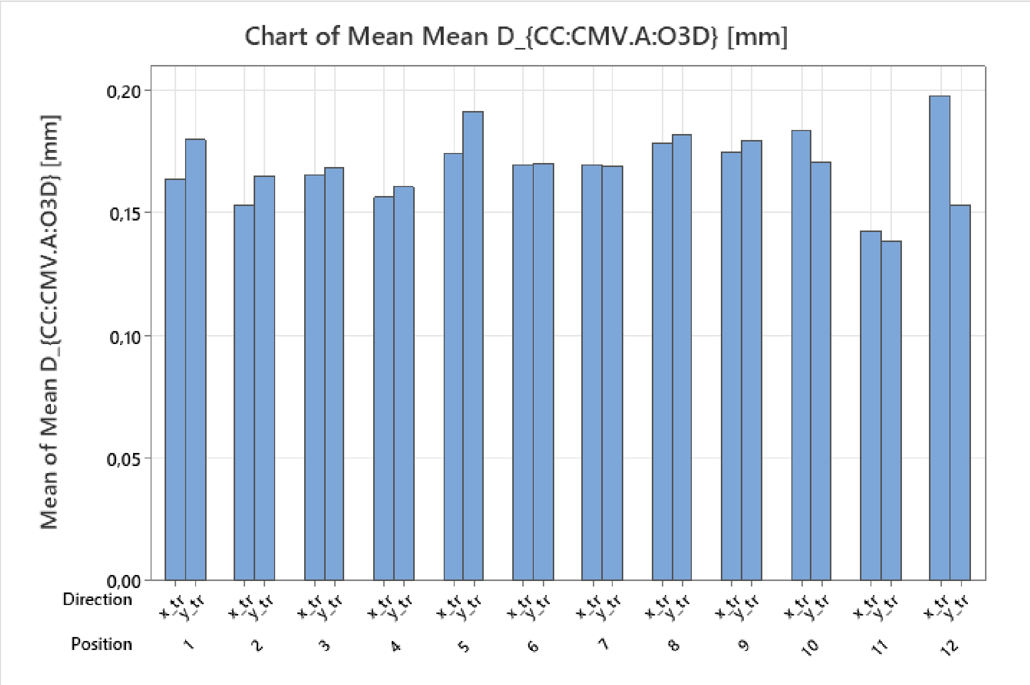

Figure 50. Mean $\boldsymbol{D}_{CC.CMV.A}$ per positions and translation direction

<u>Distortion errors - CMV.B (Multiple View)</u>

In the evaluation of the distortion error according to the CMV.B strategy, the point clouds obtained from the CMV.A measurements are fused together before the fitting of the spheres: a single PC is obtained by unifying the data from all 12 positions and both translation directions but separately for each repetitions; in this manner three fused point clouds are obtained each including 24 CMV.A measurements, and three $D_{CC.CMV.B:O3D}$ are consequently computed.

Repetitions	$\boldsymbol{D}_{CC.CMV.B:O3D}$ **/ mm**
1	0.176
2	0.176
3	0.187

Table 17. Distortion errors CMV.B

The maximum observed $D_{CC.CMV.B:O3D}$ is equal to 0.187 mm, and it is represented in Figure 51. As can be observed, the three errors obtained by the fusion processes are perfectly aligned with the "single view" distortion error values, indicating that there is not a significant error introduced by the live positioning and registration system of the HandySCAN.

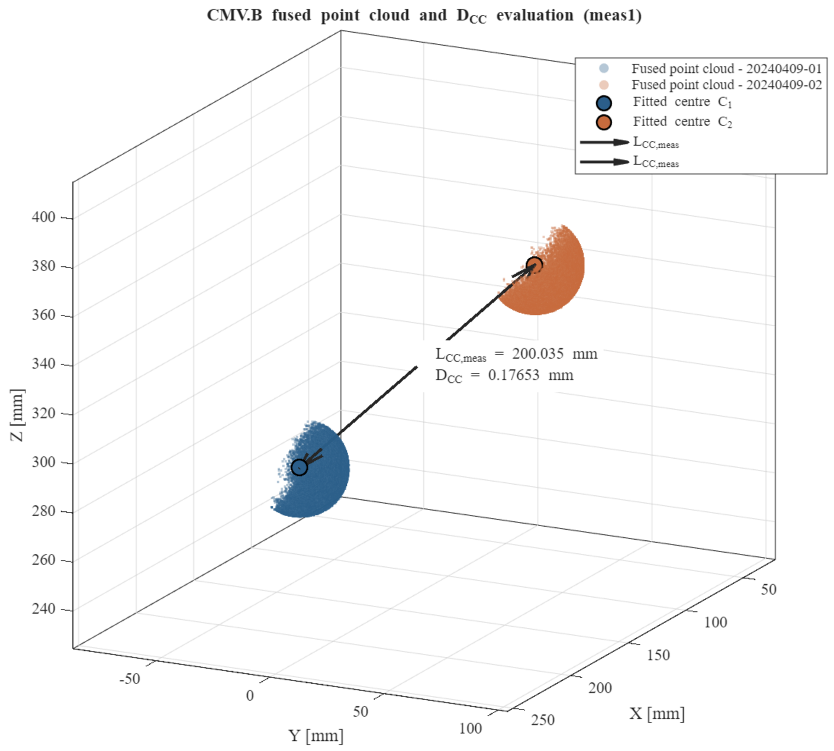

Figure 51. Maximum distortion error $D_{CC.CMV.B}$ obtained from the fusion of the first repetitions of the CMV.A measurements.

<u>Distortion Errors - CMV.C (Free pathway measurement)</u>

For the CMV.C strategy, three repeated measurements were performed by moving the sensor freely around the two calibrated spheres. From these measurements three distortion errors are computed and reported in Table 18.

Repetitions	$D_{CC.CMV.C:O3D}$ / mm
1	0.185
2	0.182
3	0.183

Table 18. Distortion errors CMV.C

The maximum observed $D_{CC.CMV.C:O3D}$ is equal to 0.185 mm. The values obtained with this scanning strategy are surprisingly larger than the ones obtained with translation motions, despite the free-pathway approach guaranteeing a higher data completeness than other scanning strategies.

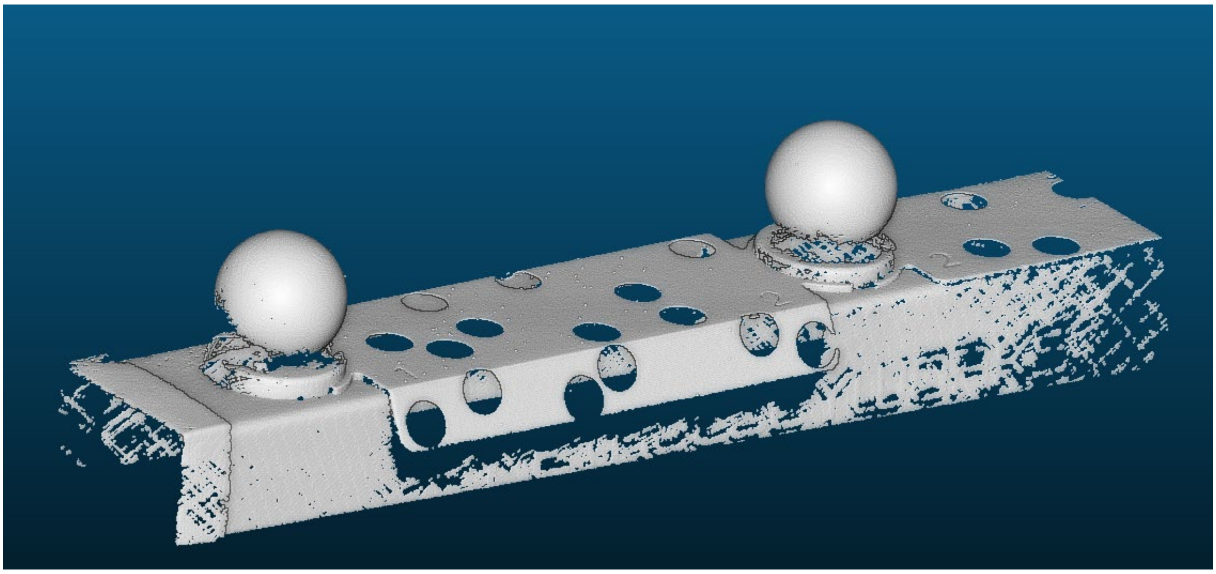

Figure 52. Point cloud acquired in the first repetition of the $D_{CC.CMV.C:O3D}$

4.1.2 Probing Errors

The probing size and probing form errors were evaluated according to the procedure described in section 2.2.4 , using the data acquired during the distortion error measurements. The probing errors were evaluated on the calibrated metallic matte sphere 20240409-01 which occupies a different voxel in each position according to Table 9. The results are reported separately for the CMV.A, CMV.B and CMV.C scanning strategies.

Probing Errors - CMV.A (Single View)

Through the data used for the CMV.A kinematic strategy a total of 64 individual spherical point cloud was evaluated, from which a total of 4 probing error values were computed: $P_{Size.Sph}$ and $P_{Form.Sph}$ both evaluated on 100% and 95% of the points. The data are presented divided by error type.

Probing Size Errors

Position	Voxel	$P_{Size.Sph.CMV.A:x_{tr}:All:O3D}$ / mm			$P_{Size.Sph.CMV.A:x_{tr}:D95\%:O3D}$ / mm		
		Rep 1	Rep 2	Rep 3	Rep 1	Rep 2	Rep 3
1	7	-0.034	-0.024	-0.005	-0.039	-0.026	-0.006
2	6	-0.063	-0.041	-0.031	-0.058	-0.041	-0.036
3	5	-0.003	-0.021	-0.014	+0.005	-0.020	-0.016
4	8	-0.000	-0.003	-0.014	+0.001	-0.009	-0.013
5	2	-0.018	-0.011	-0.008	-0.017	-0.017	-0.011
6	1	-0.039	-0.019	-0.018	-0.037	-0.017	-0.019
7	4	-0.001	+0.005	-0.005	-0.012	+0.003	-0.005
8	6	+0.004	-0.013	-0.018	-0.014	-0.015	-0.012
9	5	-0.002	-0.013	-0.014	-0.017	-0.017	-0.019
10	6	-0.045	-0.043	+0.000	-0.045	-0.043	-0.006
11	5	-0.039	-0.049	-0.024	-0.043	-0.040	-0.018
12	6	-0.014	+0.065	+0.010	-0.020	+0.027	+0.016

Table 19. Individual probing size error values for the 12 positions of the CMV.A.x_tr test over three repetitions

Position	Voxel	$P_{Size.Sph.CMV.A:y_{tr}:All:O3D}$ / mm			$P_{Size.Sph.CMV.A:y_{tr}:D95\%:O3D}$ / mm		
		Rep 1	Rep 2	Rep 3	Rep 1	Rep 2	Rep 3
1	7	-0.042	+0.003	-0.018	-0.035	-0.004	-0.022
2	6	-0.022	-0.009	-0.009	-0.023	-0.005	-0.013
3	5	-0.006	-0.010	+0.007	-0.006	-0.014	+0.003
4	8	-0.020	-0.024	-0.023	-0.022	-0.028	-0.028
5	2	+0.012	-0.011	+0.011	+0.015	-0.009	+0.009
6	1	-0.004	-0.022	-0.012	-0.008	-0.025	-0.014
7	4	-0.024	+0.002	-0.042	-0.028	-0.003	-0.039
8	6	-0.076	+0.002	+0.058	-0.062	+0.029	+0.046
9	5	-0.064	-0.070	-0.005	-0.046	-0.073	-0.011
10	6	-0.041	+0.011	-0.012	-0.060	+0.005	-0.002
11	5	-0.080	-0.030	-0.045	-0.085	-0.028	-0.058
12	6	-0.021	-0.057	-0.028	-0.020	-0.060	-0.027

Table 20. Individual probing size error values for the 12 positions of the CMV.A.y_tr test over three repetitions

The largest absolute value observed for the probing size error (i = All) is equal to −0.080 mm, found at position 11 for the y_tr direction (voxel 5); the same measurement gives also the largest probing size error considering the 95% percentile of data, which is equal to -0.085 mm. Table 21 summarizes the range of the probing size error for both percentiles and directions.

For the evaluation of the diameter, it can be observed that the effect of the 95% filtering process does not give always positive outcomes, the removal of points in certain cases could result in a worse sphere fitting. Moreover, unlike the distortion error results, the sign of the probing size error is less uniform: most positions show negative results indicating an underestimation of the measured diameter, but position 11 y_tr and position 12 x_tr differs from this trend, indicating that the probing size error is more sensitive to run-to-run variability at specific voxels than to a globally consistent underestimation trend.

Direction	Range	All	95%
x_tr	Minimum $P_{Size.SPh}$ / mm	−0.063 (Position 2)	−0.058 (Position 2)
	Maximum $P_{Size.Sph}$ / mm	+0.065 (Position 12)	+0.027 (Position 12)
y_tr	Minimum $P_{Size.SPh}$ /mm	−0.080 (Position 11)	−0.085 (Position 11)
	Maximum $P_{Size.Sph}$ / mm	+0.058 (Position 8)	+0.046 (Position 8)

Table 21. Range of the $P_{Size.Sph}$ for x_tr and y_tr directions, across all the measurements

Probing Form Errors

Position	Voxel	$P_{Form.Sph.CMV.A:x_{tr}:All:O3D}$ / mm			$P_{Form.Sph.CMV.A:x_{tr}:D95\%:O3D}$ / mm		
		Rep 1	Rep 2	Rep 3	Rep 1	Rep 2	Rep 3
1	7	1.065	0.878	0.816	0.151	0.176	0.194
2	6	0.856	1.492	0.796	0.237	0.319	0.189
3	5	0.966	0.676	0.578	0.181	0.178	0.121
4	8	0.573	0.849	0.808	0.114	0.193	0.191
5	2	0.480	0.535	0.513	0.094	0.095	0.079
6	1	0.514	0.401	0.575	0.066	0.064	0.076
7	4	1.094	0.524	0.498	0.084	0.101	0.090
8	6	1.363	1.275	0.956	0.425	0.338	0.284
9	5	1.222	1.224	1.239	0.426	0.271	0.231
10	6	1.249	1.651	1.315	0.333	0.569	0.531
11	5	1.353	1.432	1.102	0.407	0.358	0.366
12	6	1.339	2.043	1.076	0.300	0.936	0.269

Table 22. Individual probing Form error values for the 12 positions of the CMV.A.x_tr test over three repetitions

Position	Voxel	$P_{Form.Sph.CMV.A:y:All:O3D}$ / mm			$P_{Form.Sph.CMV.A:y_{tr}:D95\%:O3D}$ / mm		
		Rep 1	Rep 2	Rep 3	Rep 1	Rep 2	Rep 3
1	7	0.852	1.269	0.695	0.233	0.288	0.181
2	6	0.904	1.203	0.924	0.203	0.274	0.169
3	5	1.099	0.545	0.669	0.206	0.121	0.158
4	8	0.673	0.961	1.001	0.153	0.171	0.169
5	2	0.603	0.446	0.587	0.101	0.081	0.101
6	1	0.693	0.917	0.251	0.095	0.076	0.058
7	4	0.802	0.552	0.497	0.134	0.126	0.148
8	6	1.015	1.173	1.424	0.341	0.414	0.564
9	5	1.559	1.186	1.467	0.421	0.344	0.478
10	6	1.779	1.220	1.338	0.592	0.423	0.444
11	5	1.225	1.284	1.595	0.404	0.519	0.459
12	6	0.676	1.226	0.760	0.147	0.258	0.174

Table 23. Individual probing Form error values for the 12 positions of the CMV.A.y_tr test over three repetitions

The largest observed value for the probing form error (i = All) is equal to 2.043 mm, found at position 12 for the x_tr direction (voxel 6); the second highest value, 1.779 mm, is found at position 10 for the y_tr direction, also corresponding to voxel 6. This indicates that voxel 6 is consistently the least favourable across both translation directions, but this is also the position with the highest number of repeated measurements.

Considering the 95th percentile, the largest value is 0.936 mm, found at position 12 (voxel 6) for the x_tr direction. A significant drop in magnitude of the errors when comparing the same measurements with different percentile values confirms that the 95% filtering removes a substantial fraction of the outlying points. Table 24 summarizes the range of the probing form error for both percentiles and directions.

The highest probing form error values are concentrated in the voxels farther from the sensor (5 to 8), while the nearer voxels (1, 2 and 4) show comparatively lower dispersion. This spatial trend directly reflects voxel placement within the concatenated measurement volume, consistent with the expected degradation of angular resolution and point density of a laser triangulation sensor as the working distance increases within the depth of field.

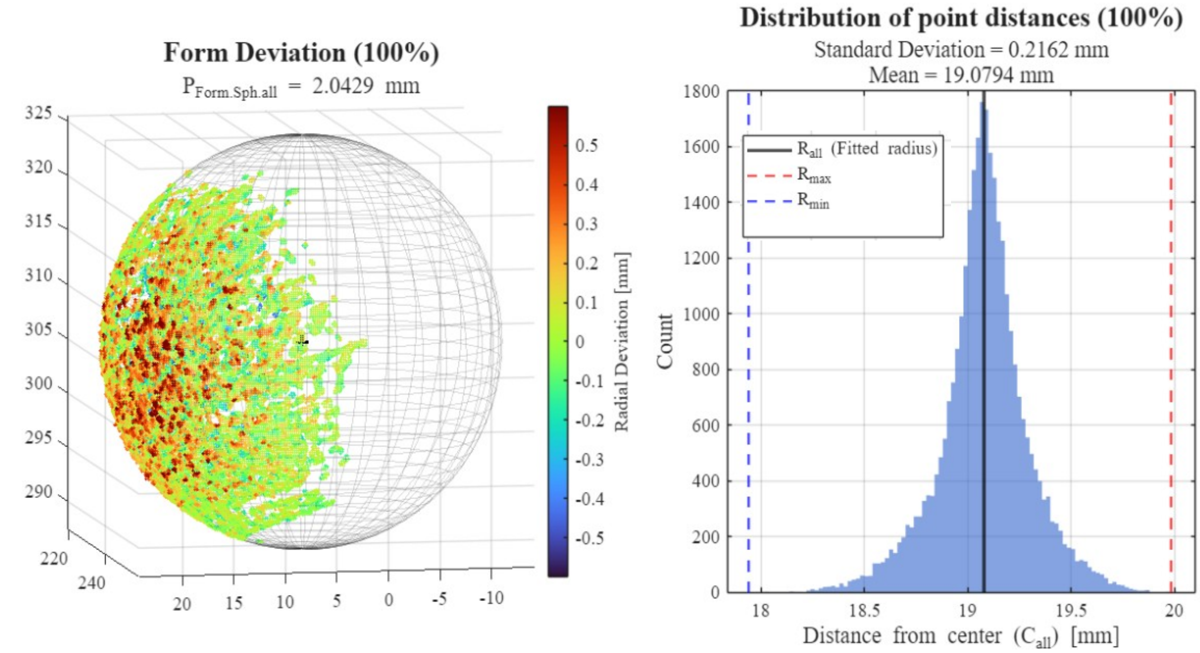

Figure 53. Maximum observed probing form error (100% of points) on sphere 20240409-01, position 12, repetition 2. Left: colour map of point residuals with respect to the fitted radius. Right: histogram of point distances from the fitted centre C_{All}.

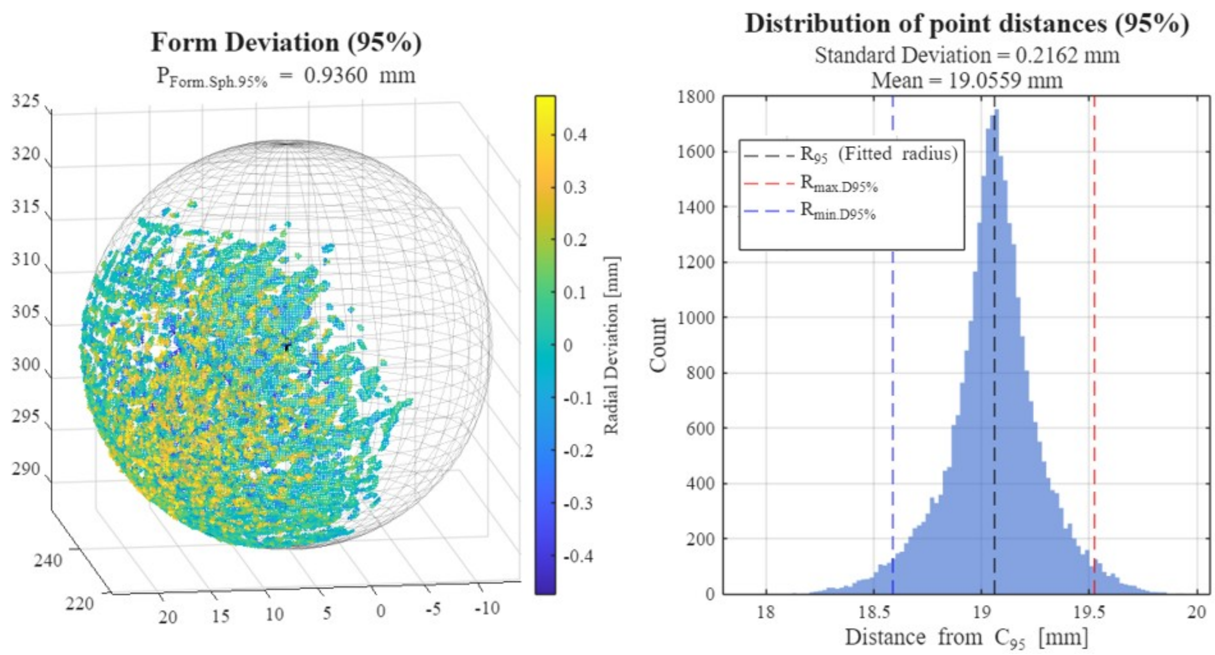

Figure 54. Maximum observed probing form error (95th percentile) on sphere 20240409-01, position 12, repetition 2. Left: colour map of point residuals with respect to the fitted radius. Right: histogram of point distances from the fitted centre $C_{95\%}$.

Direction	Range	All	D95%
x_tr	**Minimum** $P_{Form.SPh}$ / mm	0.401 (Position 6)	0.064 (Position 6)
	Maximum $P_{Form.Sph}$	2.043 (Position 12)	0.936 (Position 12)
y_tr	**Minimum** $P_{Form.SPh}$ / mm	0.251 (Position 6)	0.058 (Position 6)
	Maximum $P_{Form.Sph}$ / mm	1.779 (Position 10)	0.592 (Position 10)

Table 24. Range of the $P_{Form.Sph}$ for x_tr and y_tr directions, across all the measurements

Probing Errors - CMV.B (Multiple View)

For the CMV.B strategy, the same fused final point cloud defined for the evaluation of $D_{CC.CMV.B:O3D}$ was employed but extracting only the sphere 20240409-01 obtaining a total of 3 values for each error. The results are reported in Table 25 and Table 26.

Repetitions	$P_{Size.Sph.CMV.B.All:O3D}$ / mm	$P_{Size.Sph.CMV.B.D95\%:O3D}$ / mm
1	−0.0132	−0.0014
2	−0.0104	−0.0023
3	+0.0002	+0.0088

Table 25. Probing Size error results for the CMV.B strategy

Repetitions	$P_{Form.Sph.CMV.B.All:O3D}$ / mm	$P_{Form.Sph.CMV.B.D95\%:O3D}$ / mm
1	1.783	0.300
2	2.100	0.353
3	1.694	0.299

Table 26. Probing Form error results for the CMV.B strategy

As it can be noticed the probing size error remains small across all the three repetitions, showing $P_{Size.Sph.CMV.B.All:O3D}$ equal to -0.0132 mm and $P_{Size.Sph.CMV.B.D95\%:O3D}$ equal to +0.0088 mm as the largest errors; this means that the fusion process does not influence significantly the estimated diameter.

On the other hand, the probing form errors of the CMV.B strategy are larger than the CMV.A mean errors and comparable to the CMV.A results observed in the farther voxels (positions 8-10). This behaviour is expected, since the CMV.B point cloud results from the fusion of all the CMV.A measurements; the fused shell thickness is therefore driven by the highest noise contributions. The largest probing form errors for percentile of points 100% and 95% are respectively 2.100 mm and 0.353 mm.

Probing Errors - CMV.C (Free Movement Measurements)

As for the other evaluations of the probing errors also in this case the data used were the three scans already employed for the distortion error evaluations, but using just sphere 20240409-01.

The probing size errors associated to this scanning strategy are reported in Table 27 while the probing form error in Table 28.

Repetitions	$P_{Size.Sph.CMV.C.All:O3D}$ / mm	$P_{Size.Sph.CMV.C.D95\%:O3D}$ / mm
1	+0.027	+0.027
2	+0.017	+0.020
3	+0.021	+0.027

Table 27. Probing Size error results for the CMV.C strategy

Repetitions	$P_{Form.Sph.CMV.C.All:O3D}$ / mm	$P_{Form.Sph.CMV.C.D95\%:O3D}$ / mm
1	1.557	0.085
2	1.687	0.078
3	1.795	0.080

Table 28. Probing Form error results for the CMV.C strategy

Differently from the CMV.A and CMV.B strategies, the CMV.C probing size error is consistently positive across the three repetitions, suggesting a slight overestimation of the calibrated diameter under free-pathway scanning conditions, in contrast with the marginally negative bias observed for CMV.A and CMV.B.

The probing form error, on the other hand, is close to the mean CMV.A values (All percentile), but lower than the CMV.B result; the free motion of the CMV.C strategy, covering the sphere from several point of view, appears to avoid the accumulation of the higher-dispersion contributions that characterize the farther voxels of the CMV.A and CMV.B volumes. This could mean that a continuous and unconstrained scanning path allows the sensor to average out localized systematic errors and the noise amplification that typically affect the extremities of the sensors measurement volume .

4.1.3 Flat-Form Distortion Errors

The flat form distortion errors results, according to section 2.2.5 were evaluated using the granite plane surface as reference artefact, and the results are reported in the following separately based on the kinematic scanning strategy.

<u>Flat Form Distortion Errors - CMV.A (Single View)</u>

In the "single view" scanning strategy, the reference plane was measured considering the 6 positions described in the standard, with both translation directions (x_tr and y_tr) and for 3 repetitions, for a total of 36 individual CMV.A measurements.

Position	$D_{Form.Pla.CMV.A:x_{tr}:All:O3D}$ / mm			$D_{Form.Pla.CMV.A:x_{tr}:D95\%:O3D}$ / mm		
	Rep 1	Rep 2	Rep 3	Rep 1	Rep 2	Rep 3
1	1.597	1.214	2.202	0.151	0.215	0.159
2	3.542	1.853	1.771	0.726	0.449	0.370
3	2.928	3.412	2.900	0.998	1.190	0.991
4	1.070	1.290	1.164	0.228	0.179	0.174
5	1.237	1.097	0.972	0.321	0.199	0.131
6	2.052	1.192	0.976	0.312	0.176	0.142

Table 29. Flat-Form Distortion Error values obtained for the 6 positions of the CMV.A strategy and considering the x_tr movement

Position	$D_{Form.Pla.CMV.A:y:All:O3D}$ / mm			$D_{Form.Pla.CMV.A:y_{tr}:D95\%:O3D}$ / mm		
	Rep 1	**Rep 2**	**Rep 3**	**Rep 1**	**Rep 2**	**Rep 3**
1	1.646	1.458	1.465	0.153	0.307	0.181
2	2.134	2.138	2.398	0.564	0.580	0.597
3	3.028	2.915	2.930	1.062	0.938	1.087
4	1.217	1.317	1.038	0.247	0.163	0.173
5	1.488	1.090	1.264	0.209	0.204	0.120
6	1.737	0.950	1.510	0.277	0.156	0.104

Table 30. Flat-Form Distortion Error values obtained for the 6 positions of the CMV.A strategy and considering the y_tr

The largest observed value for the flat-form distortion error (i = All) is equal to 3.542 mm, found at position 2 for the x_tr direction; considering the y_tr direction, the largest value is instead 3.028 mm, found at position 3. The position 3, which corresponds to the farthest position of the surface with respect the sensor, shows the highest values for both translation directions; this suggests that in this region of the concatenated measurement volume is an higher level of noise is acquired.

Considering the 95th percentile, the largest value is 1.190 mm (x_tr, position 3) and 1.087 mm (y_tr, position 3), again located at the same position, confirming that the 95% filtering, while substantially reducing the magnitude of the error, does not change which position of the measurement volume is the most critical.

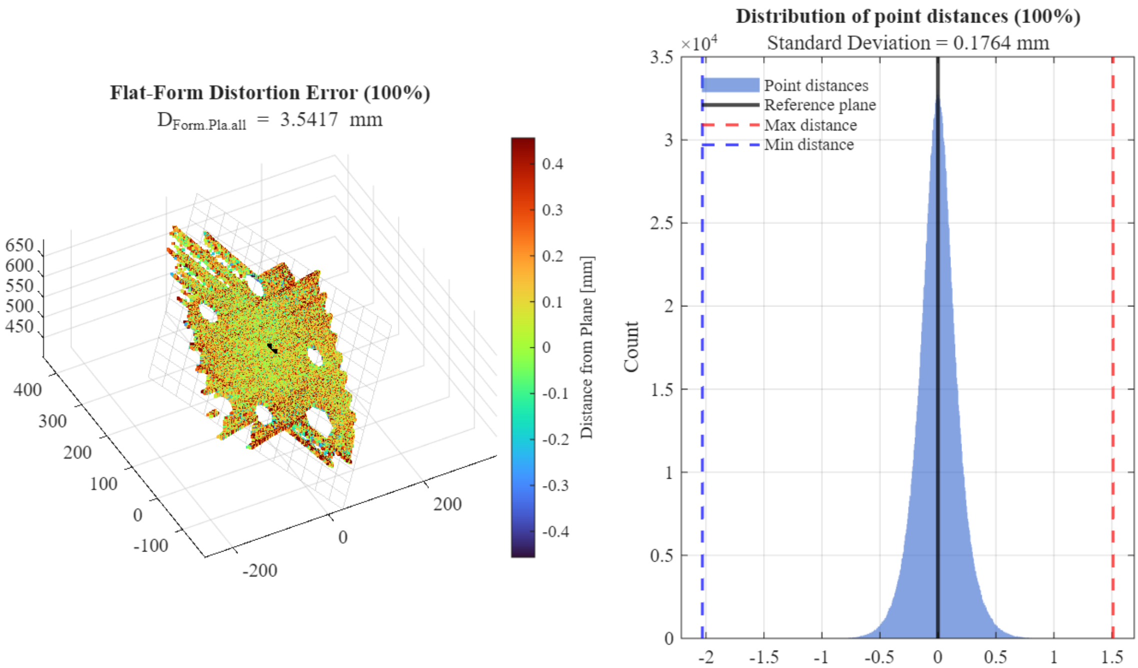

Figure 55. Maximum observed flat-form distortion error (100% of points), CMV.A strategy, position 2, x_tr direction, repetition 1. Left: colour map of point distances from the fitted reference plane. Right: histogram of the distance distribution, with the maximum (red) and minimum (blue) values indicated.

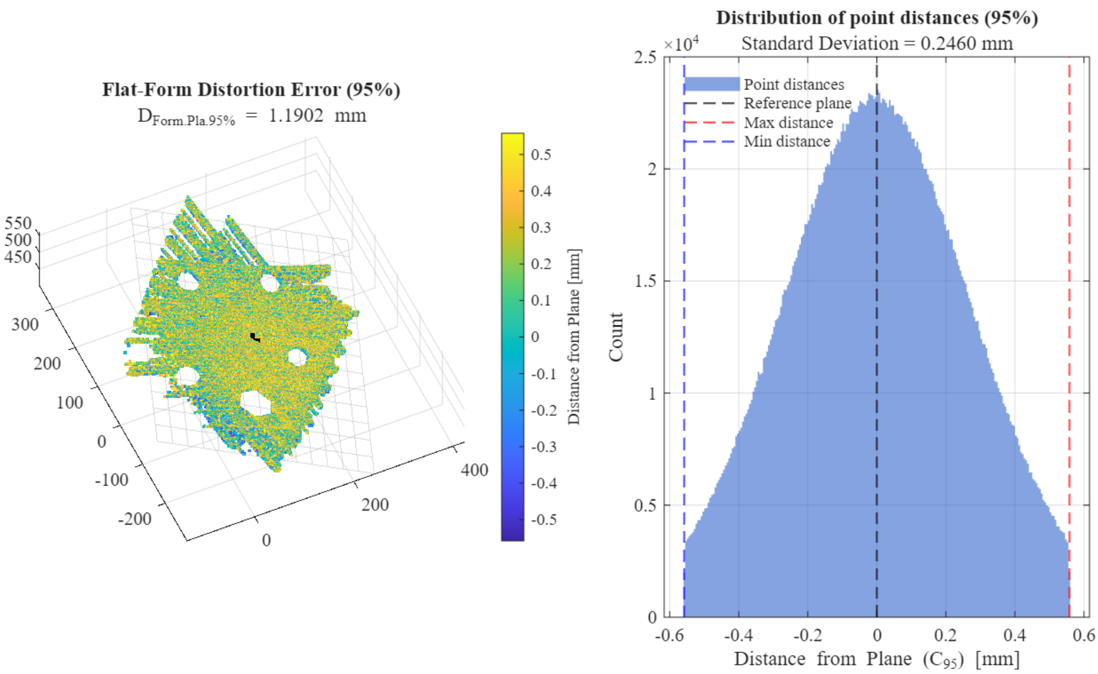

Figure 56. Maximum observed flat-form distortion error (95th percentile), CMV.A strategy, position 3, x_tr direction. Left: colour map of point distances from the fitted reference plane. Right: histogram of the distance distribution, with the maximum (red) and minimum (blue) values indicated.

Flat Form Distortion Errors - CMV.B (Multiple View)

Considering and fusing a single repetition across all the measured positions, three values are obtained for the "multiple-view" strategy, CMV.B.

Repetitions	$D_{Form.Pla.CMV.B.All:O3D}$ / mm	$D_{Form.Pla.CMV.B.D95\%:O3D}$ / mm
1	3.651	0.733
2	3.400	0.716
3	3.153	0.749

Table 31. Flat-Form Distortion Error values obtained for the CMV.B strategy

The maximum observed $D_{Form.Pla.CMV.B:All:O3D}$ is equal to 3.651 mm. As for the distortion and probing errors, the CMV.B result is consistent with, and only slightly larger than, the highest values recorded among the individual CMV.A positions (position 2 and 3), confirming that the fusion of the six single-view measurements does not introduce an additional systematic contribution beyond what is already present in the individual acquisitions, but rather reflects the least favourable local behaviour of the sensor across the whole measurement volume.

The maximum observed $D_{Form.Pla.CMV.B:D95\%:O3D}$ is equal to 0.749 mm, confirming that the 95% filtering reduces significantly the magnitude of the error and following the same trend already observed for the "All" percentile.

Flat Form Distortion Errors - CMV.C (Free Movement Measurements)

Three repeated measurements were performed with the CMV.C strategy, by moving the sensor freely around the granite reference plane. From these measurements the respective flat-form distortion errors are computed and reported in Table 32.

Repetitions	$D_{Form.Pla.CMV.C.All:O3D}$ / mm	$D_{Form.Pla.CMV.C.D95\%:O3D}$ / mm
1	1.671	0.045
2	1.463	0.060
3	1.447	0.059

Table 32. Flat-Form Distortion Error values obtained for the CMV.C strategy

The maximum observed value considering the 100% of points is equal to 1.671 mm, while the one evaluated on the 95th percentile is 0.060 mm. It can be noticed that the effect of the 95th percentile filtering largely reduces the flat-form errors in each repeated measurement; this indicates that the presence of outliers significantly affects the errors calculated in the complete point clouds.

From the comparison of these results with ones measured with the other strategies some quantitative observations can be made. Considering the 100th percentile, the CMV.C strategy shows better results (lower flat-form distortion errors) than the CMV.B, while they are comparable with the values obtained in closer positions of the CMV.A measurements. Considering the errors evaluated with the 95% filtering, the CMV.C results are lower than both the CMV.B and CMV.A. This behaviour is consistent with was already observed for the probing form errors

It can be noticed the $D_{Form.Pla.CMV.C:O3D}$ results are comparable to the values obtained with the CMV.A strategy in the closer positions of the measurement volume.

Compared to the CMV.A results, the CMV.C flat-form distortion error (95th percentile) is markedly lower, suggesting that the free-pathway strategy, covering the reference plane from multiple points of view, averages out localized systematic contributions in a similar way to what was observed for the probing form error. This is consistent with the free motion allowing the sensor to compensate for the noise amplification effects that typically affect fixed-direction acquisitions.

4.1.4 Volumetric Length Measurement Errors

The volumetric length measurement error E_{vol} was evaluated according to the procedure described in section 2.2.6 , using the calibrated ball beam equipped with all six metallic matte spheres. The measurements were performed following the CMV.D strategy at three working distances (Position 1, 2 and 3) and along both translation directions (x_tr and y_tr), with three repetitions each, for a total of 18 measurements. The errors of indication for each calibrated length are presented in Table 33 and Table 34, divided by position and translation movement direction. The maximum error of indication registered is equal to 0.265 mm, which was measured in the position 3 (corresponding to the highest working distance) with the x_tr translation direction.

Position	$\mathbf{E_{vol.CMVD.x:O3D}}$ / mm					
	l_{1-2} / mm	l_{1-3} / mm	l_{1-4} / mm	l_{1-5} / mm	l_{1-6} / mm	Max / mm
1	0.170	0.114	0.125	0.224	0.098	0.224
	0.166	0.112	0.119	0.226	0.103	0.226
	0.161	0.069	0.120	0.229	0.096	0.229
2	0.158	0.099	0.114	0.224	0.103	0.224
	0.167	0.106	0.124	0.233	0.106	0.233
	0.162	0.104	0.120	0.226	0.099	0.226
3	0.177	0.085	0.117	0.226	0.105	0.226
	0.167	0.099	0.120	0.244	0.111	0.244
	0.202	0.115	0.158	**0.265**	0.128	**0.265**

Table 33. E_{vol} values evaluated with the CMV.D strategy and with x_tr movement type

Position	$\mathbf{E_{vol.CMVD.y_{tr}:O3D}}$ / mm					
	l_{1-2} / mm	l_{1-3} / mm	l_{1-4} / mm	l_{1-5} / mm	l_{1-6} / mm	Max
1	0.170	0.113	0.138	0.229	0.099	0.229
	0.173	0.109	0.131	0.236	0.106	0.236
	0.161	0.101	0.126	0.238	0.104	0.238
2	0.168	0.120	0.134	0.243	0.116	0.243
	0.166	0.116	0.135	0.245	0.126	0.245
	0.164	0.119	0.134	0.244	0.115	0.244
3	0.174	0.100	0.119	0.234	0.116	0.234
	0.160	0.106	0.114	0.235	0.117	0.235
	0.172	0.111	0.114	0.232	0.125	0.232

Table 34.E_{vol} values evaluated with the CMV.D strategy and with y_tr movement type

The maximum errors across the 3 repetitions (following the logic of the worst-case scenarios) for each calibrated length and measurement position (working distance) are represented in Figure 57 and Figure 58 separately per translation direction of the movement.

It can be noticed that the trend is consistent between the two translation direction: the highest errors are consistently found for l_{1-5} (~800 mm) rather than at the longest calibrated distance l_{1-6} (~1000 mm), for all three working distances. This behaviour differs significantly from the trends typically observed, which are purely proportional; this suggests that the propagation of the registration and concatenation errors along the CMV.D strategy is not uniform along the length of the ball beam, but could be instead influenced by local effects of the live tracking system.

Another aspect which can be noticed is the effect of the working distance in the x_tr direction: the position 3 shows the largest errors across all calibrated lengths. However, this trend is less distinct for the y_tr direction, no clear subdivision between the positions appears.

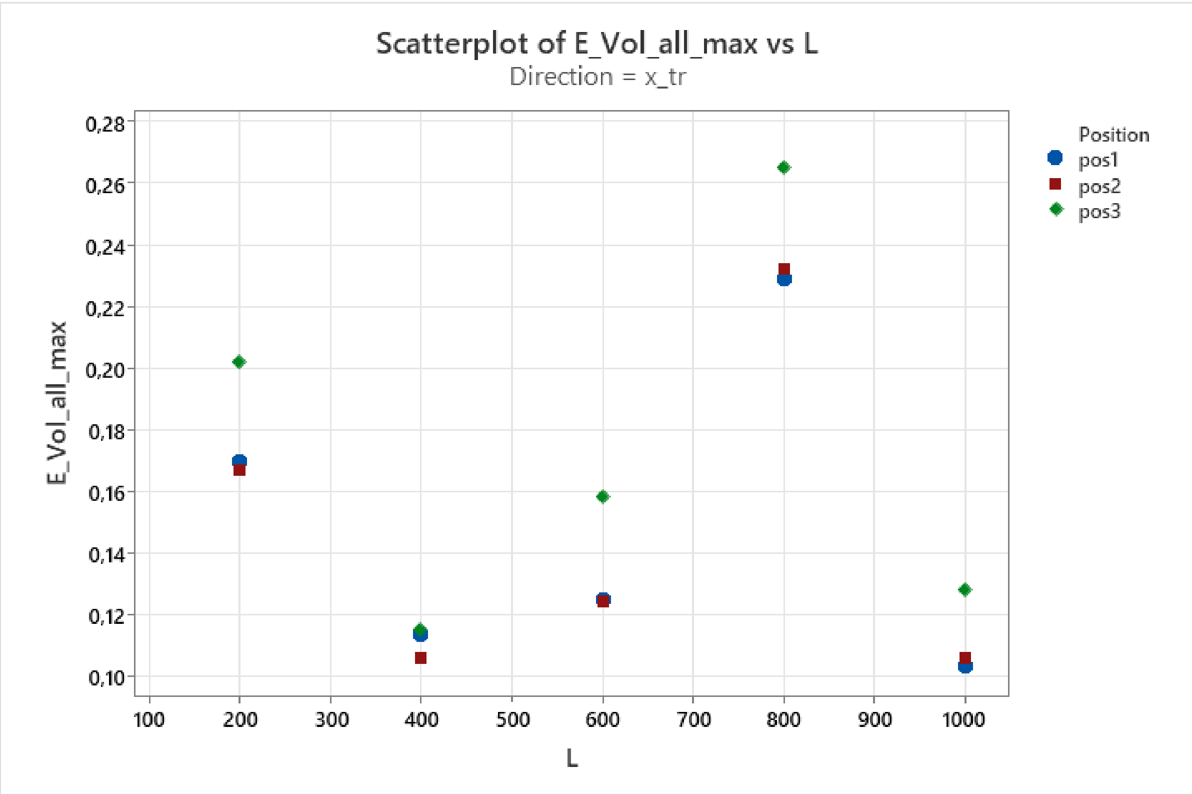

Figure 57. Scatterplot in which for each calibrated length (L) is plotted for each position the maximum observed error across the three repetitions performed with the x_tr movement

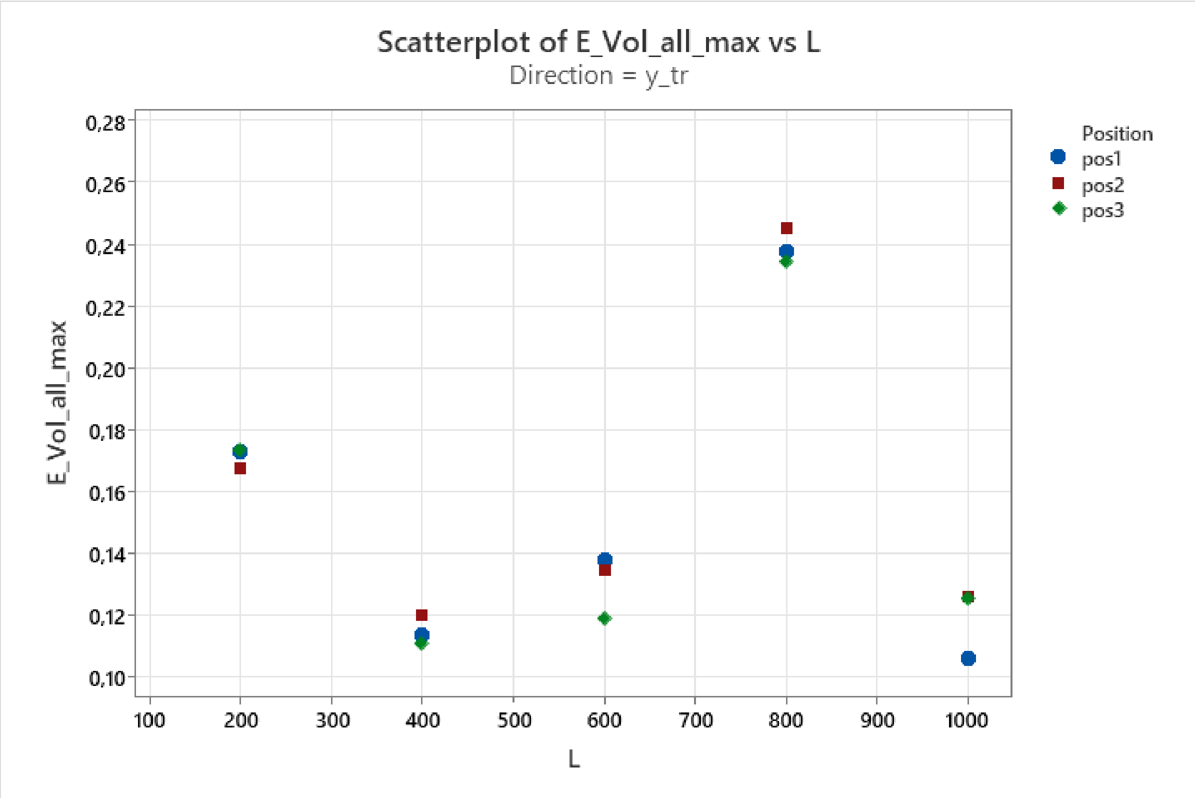

Figure 58. Scatterplot in which for each calibrated length (L) is plotted for each position the maximum observed error across the three repetitions performed with the y_tr movement

4.1.5 Performance Verification Summary

The previous sections presented the experimental results of the performance verification of the HandySCAN SILVER according to the methods proposed in section 2.2. Table 35 reports all the maximum observed values for each error and strategy, providing an overview of the sensor performance verification, which can then be compared with the manufacturers

Error	CMV.A / mm	CMV.B / mm	CMV.C / mm	CMV.D / mm
$D_{CC.k}$	+0.239	+0.187	+0.185	—
$P_{Size.Sph.j.All}$	−0.080	−0.013	+0.027	—
$P_{Size.Sph.j.D95\%}$	−0.085	−0.002	+0.027	—
$P_{Form.Sph.j.All}$	2.043	2.100	1.795	—
$P_{Form.Sph.j.D95\%}$	0.936	0.353	0.085	—
$D_{Form.Pla.j.All}$	3.542	3.542	1.671	—
$D_{Form.Pla.j.D95\%}$	1.190	0.749	0.060	—
$E_{vol.j}$	—	—	—	+ 0.265

Table 35. Summary table of the maximum observed values for each performance verification test; the errors are reported separately for each scanning strategy

From the comparison between the scanning strategies, some general observations can be made. First, the values obtained with the CMV.B strategy are consistent with those observed in the least favourable positions with the CMV.A, confirming that the point cloud fusion process, performed using the same pre-acquired targets shared across all the CMV.A measurements, does not introduce any additional contribution to the error being evaluated. In fact, the fusion process even shows an improvement of the maximum observed errors, as the larger number of points taken into consideration improves sphere fitting for the distortion and probing size errors, and the point distribution for the probing form and flat-form distortion errors considered at the 95th percentile. Secondly, the CMV.C strategy allows for a higher completeness of the data, due to the free movement of the sensor, this does not impact significantly the distortion and probing size errors, while it improves the probing form and flat-form distortion errors. Finally, the 95th percentile filtering significantly reduces the magnitude of the form errors (probing form and flat-form distortion errors) in all strategies, indicating that the maximum errors evaluated on the 100% of points are strongly affected by a limited number of outliers. This effect is particularly marked for the CMV.C strategy, which shows a largest difference between the *All* and *D95%* values among the three strategies.

A direct comparison between experimental results and the manufacturers declared specifications (Table 4) requires a premise. The Accuracy (up to 0.040 mm) and Volumetric accuracy (0.020 mm ± 0.1 mm/m) specifications reported by the manufacturer do not constitute a Maximum Permissible Error (MPE) as defined by the ISO 10360-13:2021 standard. In fact, they are not associated with the same methodological procedures. The following comparison should therefore be understood as a qualitative reference and not as a conformity check in the strict sense.

Accuracy (0.040 mm) is obtained by the manufacturer by measuring the diameter of single calibrated spheres; so it conceptually corresponds to the probing size error as defined in this thesis, which evaluates the error in the spheres size. Volumetric accur acy (0.020 mm + 0.1 mm/m) is obtained by measuring the centre-to-centre distance between two spheres of different lengths; it therefore corresponds to D_{CC} and E_{vol}. For $P_{Form.Sph}$ and $D_{Form.Pla}$ errors, the manufacturer does not provide any reference data.

Applying the Volumetric accuracy to the length l_{1-2} (199.858 mm) through (13), used for the D_{CC} evaluation, a limit of 0.020 + 0.1 × 0.19986 ≈ 0.040 mm is obtained. The maximum D_{cc} value observed in this work (0.239 mm, CMV.A) is therefore much higher than this reference. Similarly, applying the same formula to the length l_{1-5} (799.927 mm), used for the maximum observed E_{vol}, a limit of 0.020 + 0.1 × 0.79993 ≈ 0.100 mm is obtained, which is lower than the maximum measured E_{vol} value (0.265 mm). For the probing size error, the observed absolute maximum value (0.080 mm, CMV.A) is approximately double the declared Accuracy (0.040 mm).

These differences do not indicate non-compliance of the instrument with the manufacturers specifications, for two main reasons. First, the experimental conditions, i.e. the scanning strategies, used in this work are more severe than those used in the manufacturers acceptance tests. The CMV.A and CMV.D strategies isolate the sensors behaviour along a single translation direction, while in manufacturers test s, the instrument is moved by a robotic arm along specific trajectories. Second, the calibration certificate results (Table 5), obtained with a different procedure than the one proposed in this work, show that the instrument meets the declared specifications under its test conditions.

These results demonstrate the extent to which the kinematic scanning strategy influences the instruments actual metrological performance. This aspect is not contemplated in the manufacturers synthetic specifications and constitutes one of the motivations behind the adaptation of the ISO 10360-13 standard proposed in this work.

4.2 Shutter Speed Optimization Results

In this section the experimental results of the shutter speed optimization campaign are reported and described. Firstly, the mattifying coating thickness characterization over the half-sprayed silicon wafer is presented, in order to better interpret the results obtained for the mattified sphere. Then, for all the four conditions represented by the spheres listed in Table 8, the dependence of the performance metrics on the shutter speed t_{SH} are presented, together with the optimal shutter speed range found for a specific priority combination which prioritizes the probing errors reduction. Specifically, the optimal shutter speed in this thesis is evaluated using the probing form and probing size errors evaluated on the 95th percentile, both with priority equal to I (corresponding to weight factor equal to 0.375) and the coverage with a priority equal to II (corresponding to a weight factor equal to 0.250).

4.2.1 Thickness of the mattifying coating

The thickness of the mattifying sprayed layer was estimated over the half-coated silicon wafer described in section 3.1.2 , using the Sensofar S Neox with the confocal microscopy method and the 20× lens (Figure 59).

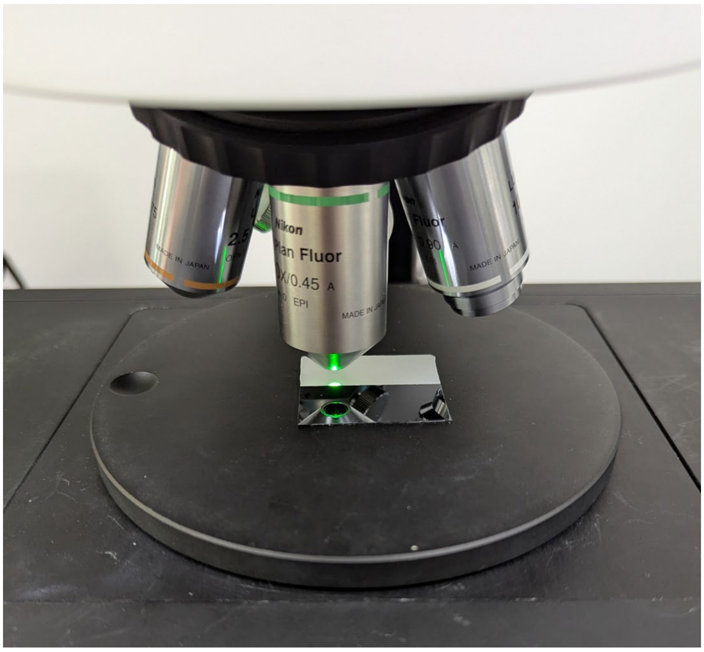

Figure 59. Coating thickness measurement by confocal microscopy (Sensofar S Neox, 20× objective)

On the height maps acquired, the thickness was evaluated as the step height measured in correspondence of the separation lines between the coated and uncoated regions [23]. In each height map an analysis band (area) crossing both regions was defined, the software (SensoView) automatically individuates a portion in each region and computes a mean height difference.

The thickness was measured in 3 different positions along the separation line (Figure 60), with 3 repetitions per position, for a total of 9 measurements. For each measurement, an area of 1.54 × 3.14 mm was acquired, obtained by stitching a 2 × 6 grid with 25% overlap. Before the step height calculation, for each height map planar form removal was performed as shown in Figure 61. The results of the step height measurements are reported in Table 36; as a summary value, the average calculated on all nine measurements is equal to 5.2 ± 0.6 μm.

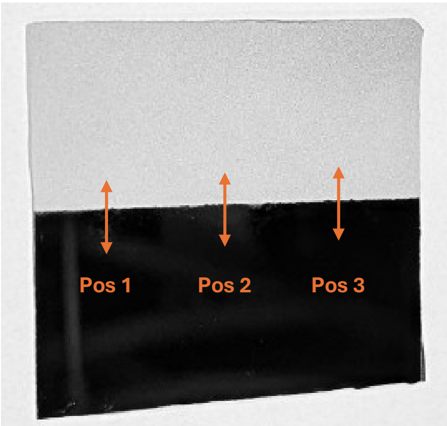

Figure 60. Confocal microscopy measurement positions over the half-coated silicon wafer; the white region corresponds to the half -coated zone while the darker one corresponds to the highly specular surface.

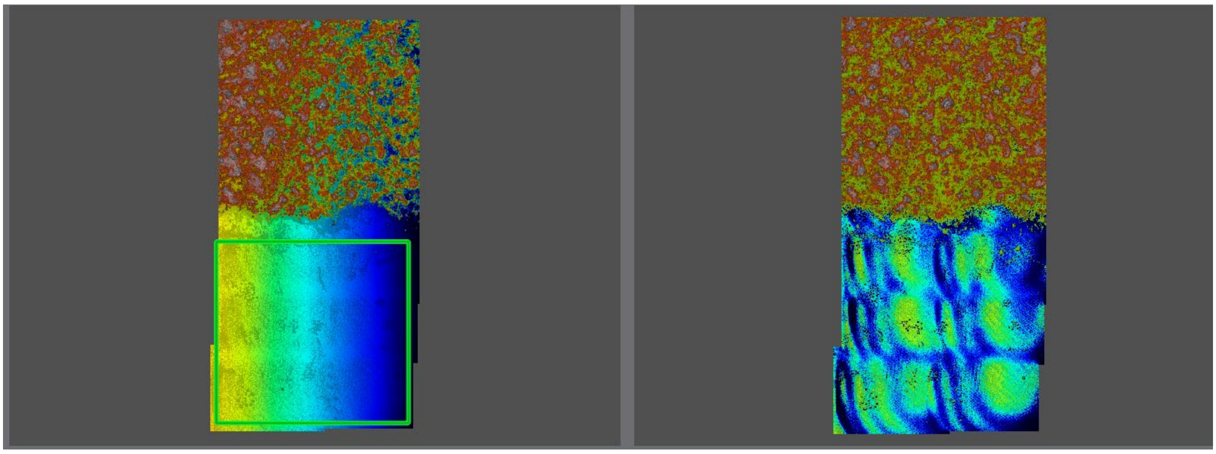

Figure 61. Plane form removal from an acquired height map

Positions	Repetitions	Step Height / µm	
1	1	5.86	5.97 ± 0.10
	2	6.02	
	3	6.03	
2	1	4.73	4.72 ± 0.01
	2	4.72	
	3	4.71	
3	1	4.86	4.84 ± 0.03
	2	4.81	
	3	4.83	
Overall mean		5.17± 0.60	

Table 36. Matting coating thickness measured by step height with the Sensofar S Neox profilometer, 20× objective, at three positions along the coating/substrate interface (3 repetitions per position; for each position the mean thickness and the standard deviation is reported.

Before the surface topography measurements, the suitability of the available silicon wafer sample was confirmed through a set of flatness measurements performed with the Chromatic confocal sensor (O-Inspect 3/2/2), evaluated on the entire surface prior to coating application (Figure 62).

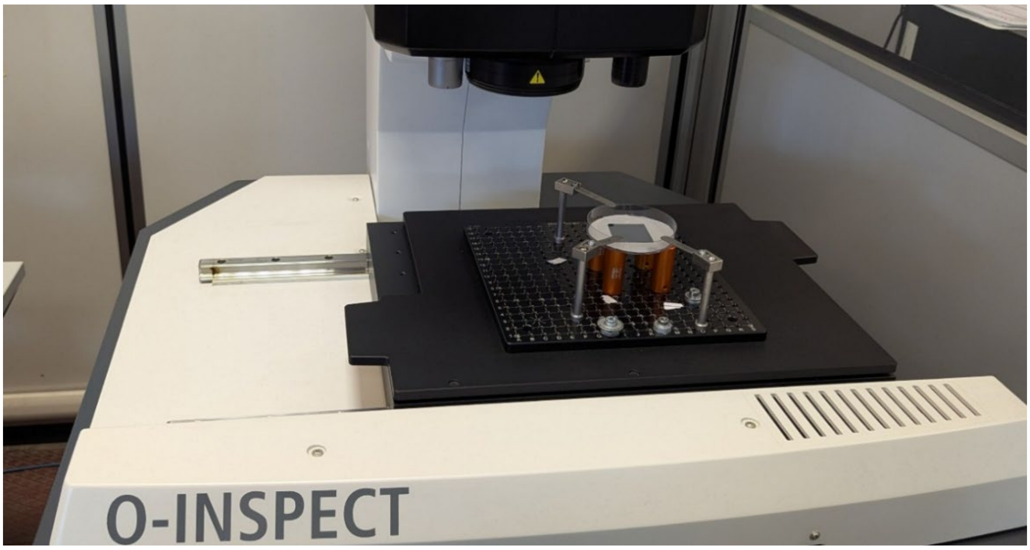

Figure 62. Flatness measurements of the uncoated silicon wafer sample

A set of 5 repeated measurements yielded a flatness of 1.196 ± 0.470 µm, well below the MPE of the instrument.

4.2.2 Metallic Matte Sphere

The first sphere considered for the shutter speed optimization is the metallic matte sphere, corresponding to sphere 20240409-01. This was measured following the procedure described in section 3.2.1 for a total of 50 individual point clouds, corresponding to 5 repeated scans for each of the 10 shutter speed levels. For each point cloud, the probing size and form errors ($i = 95\%$) together with the surface coverage and point density (kNN-based method) were computed. In Table 37 the mean and the standard deviation, for each evaluation metric at each shutter speed level t_{SH}, are reported. As it can be easily noticed in the resulting graphs the obtained results for each shutter speed level are generally characterized by a high dispersion. This aspect makes more complex the evaluation of possible trends.

t_{SH} / ms	$P_{Size.Sph.D95\%}$ / mm	$P_{Form.Sph.D95\%}$ / mm	Coverage / %	Point Density / pt/mm^2
0.10	0.038 ± 0.010	0.080 ± 0.016	58.21 ± 3.00	21.72 ± 0.13
0.15	0.031 ± 0.013	0.0921 ± 0.023	57.72 ± 8.72	21.58 ± 0.23
0.20	0.035 ± 0.012	0.0733 ± 0.004	65.13 ± 2.34	21.84 ± 0.06
0.30	0.029 ± 0.012	0.0684 ± 0.007	65.24 ± 2.99	21.82 ± 0.09
0.40	0.033 ± 0.009	0.0696 ± 0.012	67.16 ± 2.15	21.87 ± 0.07
0.50	0.034 ± 0.012	0.0670 ± 0.009	67.43 ± 3.55	21.88 ± 0.06
1.25	0.038 ± 0.005	0.0662 ± 0.007	71.22 ± 1.85	21.92 ± 0.03
2.00	0.035 ± 0.006	0.0625 ± 0.011	68.89 ± 2.84	21.90 ± 0.08
5.00	0.038 ± 0.013	0.0731 ± 0.024	63.90 ± 8.46	21.79 ± 0.27
8.00	0.043 ± 0.015	0.0680 ± 0.013	66.56 ± 4.12	21.90 ± 0.02

Table 37. Metallic matte sphere: performance metrics in function of the shutter speed (mean ± st. dev., n = 5).

The probing size error $P_{Size.Sph.D95\%}$ presents the lowest average value for t_{SH} equal to 0.30 ms, the trend does not show a clear linear pattern but suggests a slight increase of the error at the lowest level and at the higher t_{SH} values. Overall, the probing size errors remain low and stable across the whole t_{SH} range, suggesting that the sphere diameter is correctly acquired for all shutter speed conditions; it can be noticed that all the values of the probing size error are positive indicating a systematic overestimation of the sphere diameter. The probing form error $P_{Form.Sph.D95\%}$ (Figure 64) shows instead its minimum average value for a higher value of t_{SH}, which is equal to 2 ms. The trend in this case is slightly more accentuated, with a decrease of the encompassing shell thickness from 0.10 ms to 2 ms and then a small increase at the higher levels.

On the other hand, the coverage trend is much more evident: it can be seen how it increases rapidly from about 58% at the lowest shutter speeds to 71% at 1.25 ms, followed then by a slight decrease. The average point density shows the same pattern but with a much smaller relative variation. In Figure 66 the two measures taken at two different shutter speeds levels are presented and confronted: the shape of the acquired point clouds reflects the movement of the scanner which was kept always perpendicular to the surface and moved following a semicircular trajectory, it can be noticed how the shutter speed influences the ability of the instrument to acquire points in high slope regions. From this images it can be also seen that the local point density is almost constant everywhere, besides the bounding regions of the point cloud.

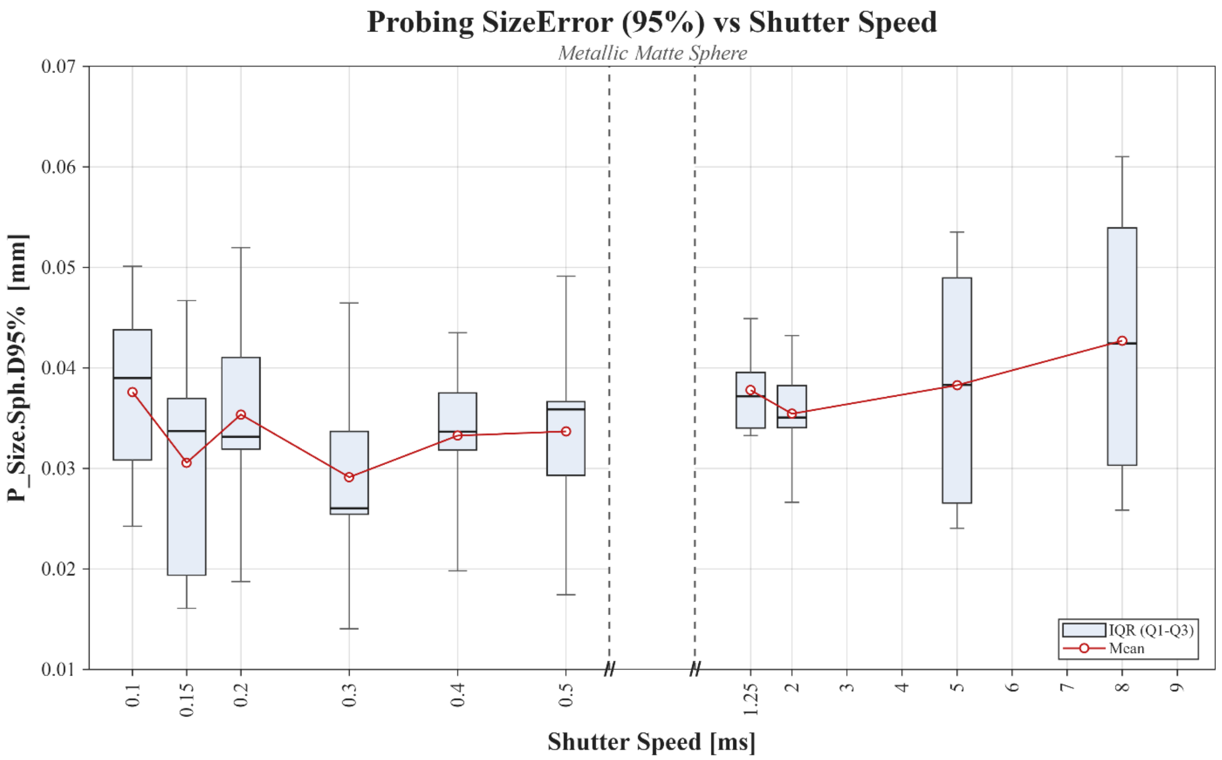

Figure 63. Metallic matte sphere: $P_{Size.Sph.D95\%}$. as a function of shutter speed, box plot with mean values (red line) and split x-axis.

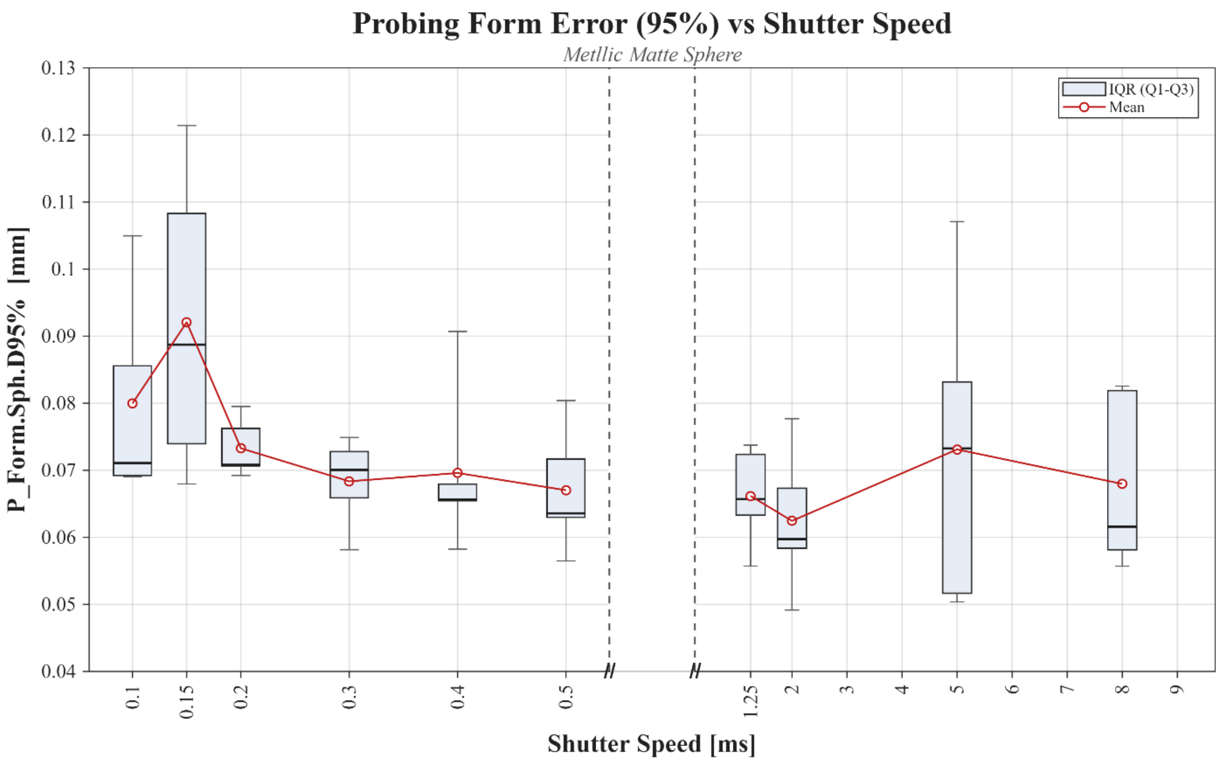

Figure 64. Metallic matte sphere: $P_{Form.Sph.D95\%}$. as a function of shutter speed, box plot with mean values (red line) and split x-axis.

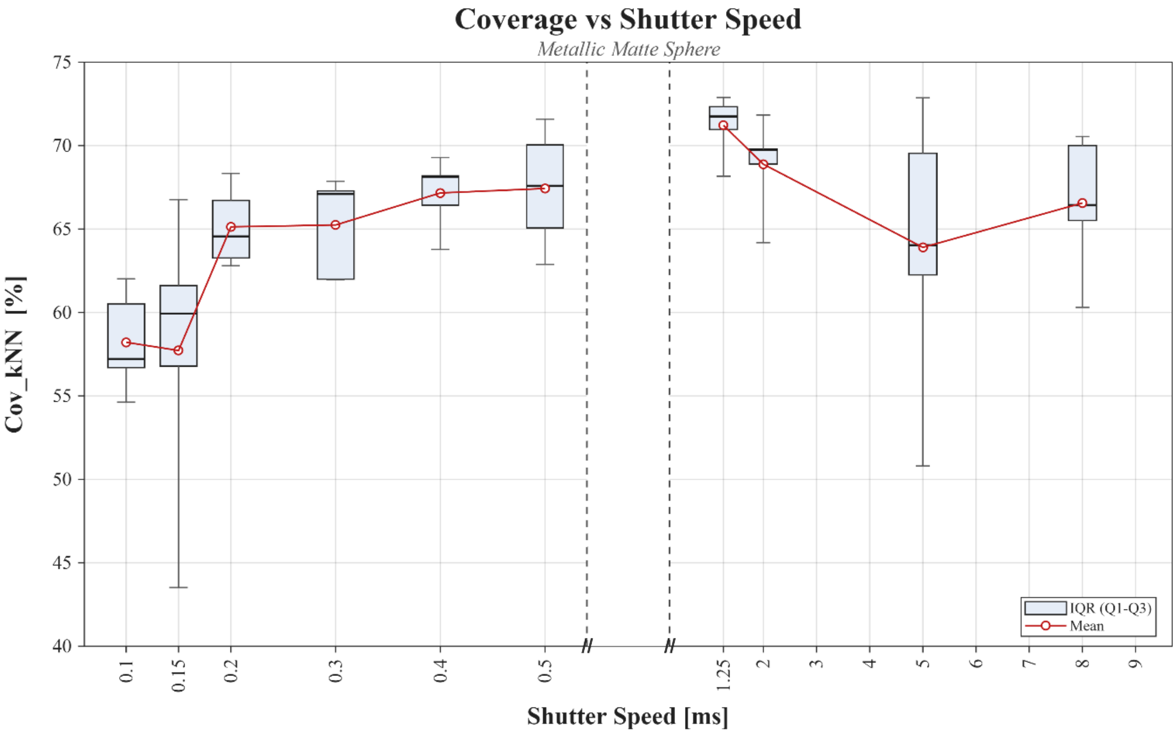

Figure 65. Metallic matte sphere: Coverage (kNN method) as a function of shutter speed, box plot with mean values (red line) and split x-axis.

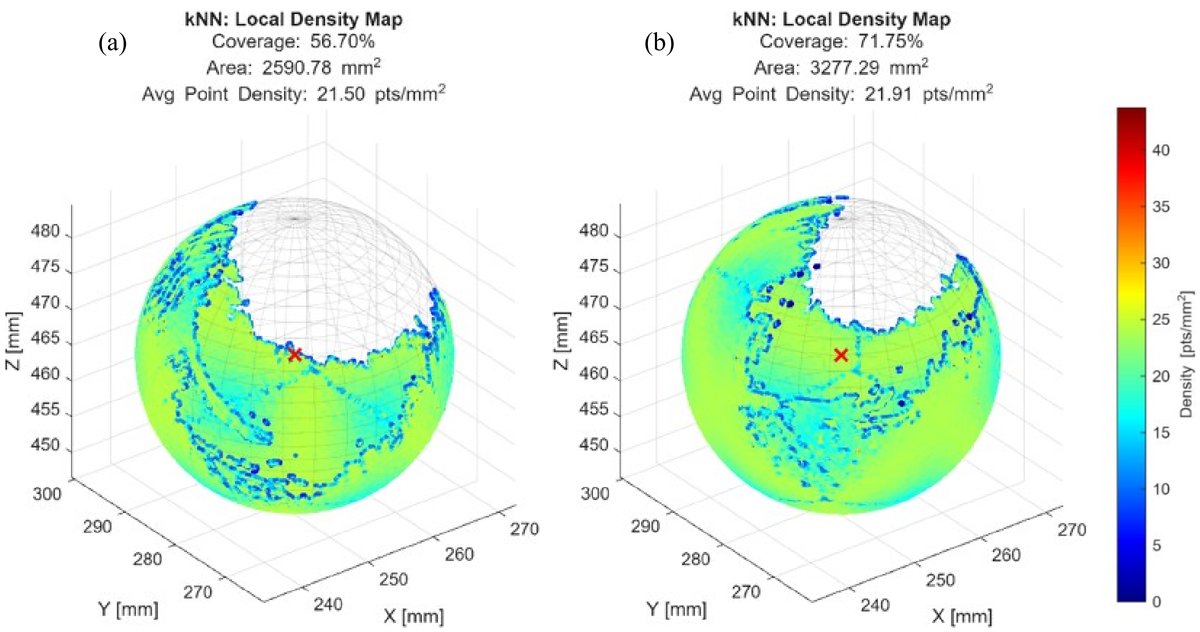

Figure 66. Point density and surface coverage on the metallic matte sphere (kNN approach): (a) $t_{SH} = 0.10\ ms$; (b) $t_{SH} = 1.25\ ms$.

The values of the probing form and size errors and coverage metrics for each shutter speed level are used to compute the Score curve (Figure 67), following the procedure described in section 3.2.4 . The resulting quadratic fit on the metallic matte sphere is concave, with the vertex inside the tested range at $t_{SH}^{*} = 3.18\ ms$. The Optimal Range, defined as the region where the fitted Score stays within 0.05 points from its maximum, extends to [1.17, 5.18] ms.

The maximum Score value reached by the fit (0.696) is relatively low, and the curve shows a weak curvature across the entire tested range: this is reflected in the wide Optimal Range, which spans over 4 ms. The highest individually measured Score (at 0.30 ms) lies above the fitted curve, suggesting that the quadratic model does not fully capture the trend in the lower shutter speed region, where the dispersion between the 5 repetitions (error bars) is also wider. To assess how much this dispersion affects the identification of the optimum, a Monte Carlo simulation is performed, repeating the parabolic fit 1000 times on synthetic Score values resampled around the experimental mean and standard deviation at each level. Only 628 out of 1000 iterations produce a valid concave fit with the vertex inside the tested range, a relatively low number that confirms the peak is not sharply defined for this surface condition. From these valid simulations, the median optimal shutter speed is $t_{SH,MC}^{*} = 3.506\ ms$ with a 68% confidence interval, corresponding to ± one standard deviation around the median, of [2.27, 4.91] ms.

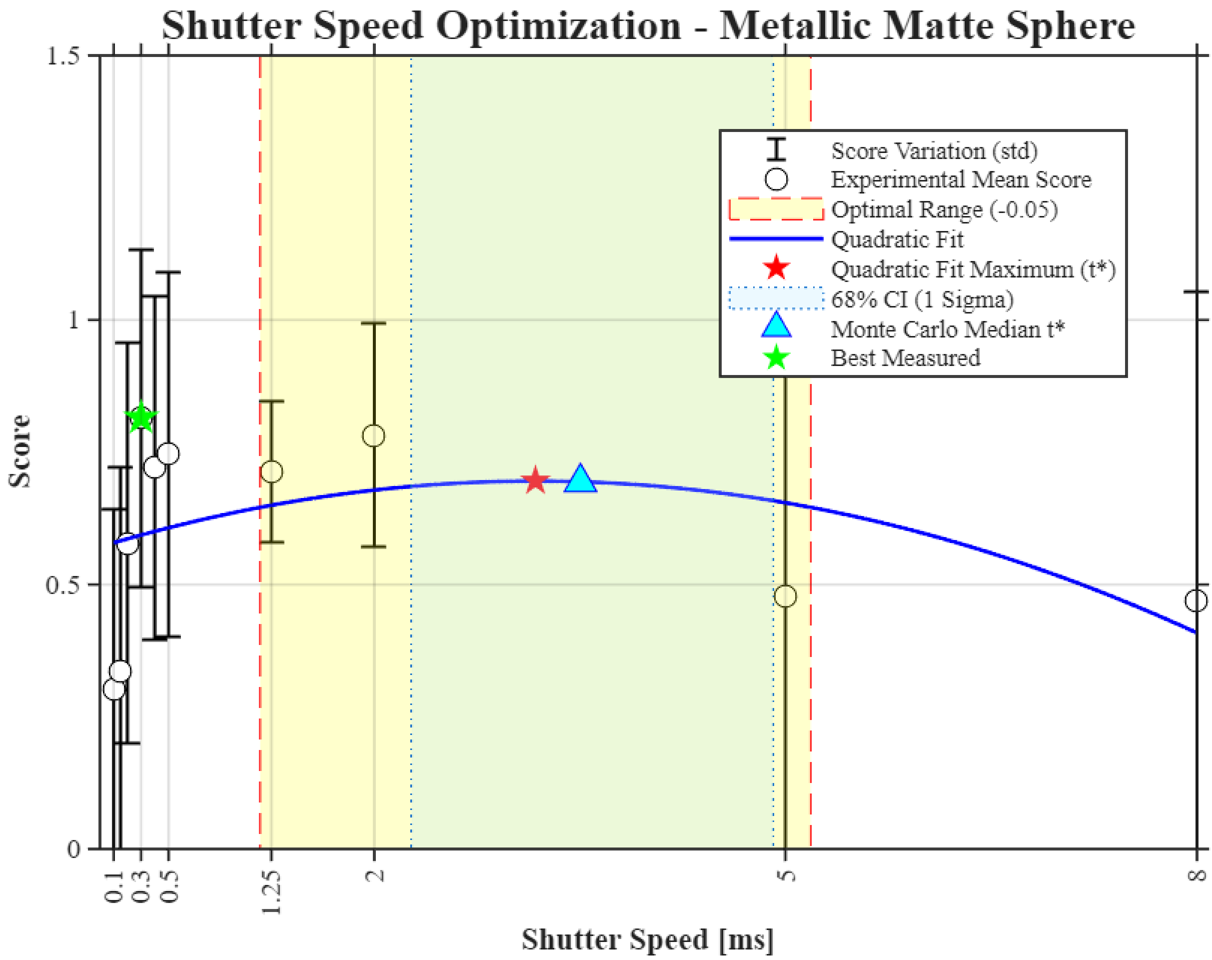

Figure 67. Score curve in function of shutter speed for the Metallic Matte Sphere (20240409-01), with quadratic fit, Monte Carlo median $(t^*_{SH,MC})$ *and 68% confidence interval.*

4.2.3 Metallic Shiny Sphere

The second sphere considered for the shutter speed optimization is the metallic shiny sphere S/N AZ140, which presents a highly polished surface strongly specular. This sphere also was measured following the procedure described in the section 3.2.1 , for a total of 50 individual point clouds, corresponding to 5 repeated scans for each of the 10 shutter speed levels. Table 38 reports the means and standard deviations of the four performance metrics for each level.

t_{SH} / ms	$P_{Size.Sph.D95\%}$ / mm	$P_{Form.Sph.D95\%}$ / mm	Coverage / %	Point Density / pt/mm²
0.10	0.046 ± 0.023	0.267 ± 0.017	3.93 ± 1.83	19.15 ± 0.86
0.15	0.035 ± 0.041	0.276 ± 0.039	7.13 ± 2.30	19.69 ± 0.48
0.20	0.052 ± 0.040	0.220 ± 0.035	13.31 ± 1.93	20.88 ± 0.33
0.30	0.060 ± 0.026	0.188 ± 0.048	19.29 ± 3.58	20.99 ± 0.17
0.40	0.056 ± 0.010	0.172 ± 0.031	27.83 ± 1.26	21.31 ± 0.08
0.50	0.066 ± 0.021	0.154 ± 0.012	30.53 ± 2.30	21.27 ± 0.06
1.25	0.057 ± 0.008	0.118 ± 0.025	50.73 ± 2.96	21.58 ± 0.09
2.00	0.051 ± 0.014	0.117 ± 0.052	54.31 ± 3.78	21.76 ± 0.12
5.00	0.051 ± 0.014	0.106 ± 0.020	57.35 ± 2.95	21.77 ± 0.13
8.00	0.055 ± 0.013	0.127 ± 0.044	57.54 ± 3.34	21.80 ± 0.15

Table 38. Metallic shiny sphere: performance metrics in function of the shutter speed (mean ± st. dev., n = 5).

Compared to the matte metal sphere, this surface type exhibits much more marked dependence on the shutter speed.

The trend of the means, represented in Figure 68, shows that the probing form error $P_{Form.Sph.D95\%}$ follows a clearly decreasing trend, from a maximum of 0.276 mm at t_{SH} of 0.15ms to a minimum of 0.106 mm at t_{SH} of 5ms. However, it is worth noting that at the t_{SH} levels of 1.25 ms and 2.00 ms the deviation is relatively high due to the presence of a single outlier, and that the trend of the medians has a minimum at the 2 ms level. On the other hand, the probing size error $P_{Size.Sph:D95\%}$ does not show a strong dependence on t_{SH} compared with its variability; the lower shutter levels are associated with higher standard deviations indicating that the values of the fitted diameters are less stable probably due to the small and inconsistent number of points acquired on the sphere. All the values are positive indicating an overestimation of the measured diameter

The coverage and point density metrics exhibit an even more marked dependence on the shutter speed: they both follow the same monotonically increasing trend across the entire range, resembling a saturating growth curve. The magnitude of the increase is particularly high in the first region, while it progressively decreases into a plateau for the higher shutter speed values. Specifically, the coverage mean value rises from 3.93% at 0.1 ms to 50.73% at 2 ms, and then progressively stabilizes at 57-58% for t_{SH} of 5 and 8 ms. The point density metrics increases from 19.15 to 21.80 pt/mm², following the same trend but with a much smaller relative variation, in line with what was already observed for the metallic matte sphere. This behaviour is well represented in Figure 71, in which is highlighted the difficulty of the scanner in acquiring points at low shutter speeds and the difference in coverage between the two extreme shutter speed levels.

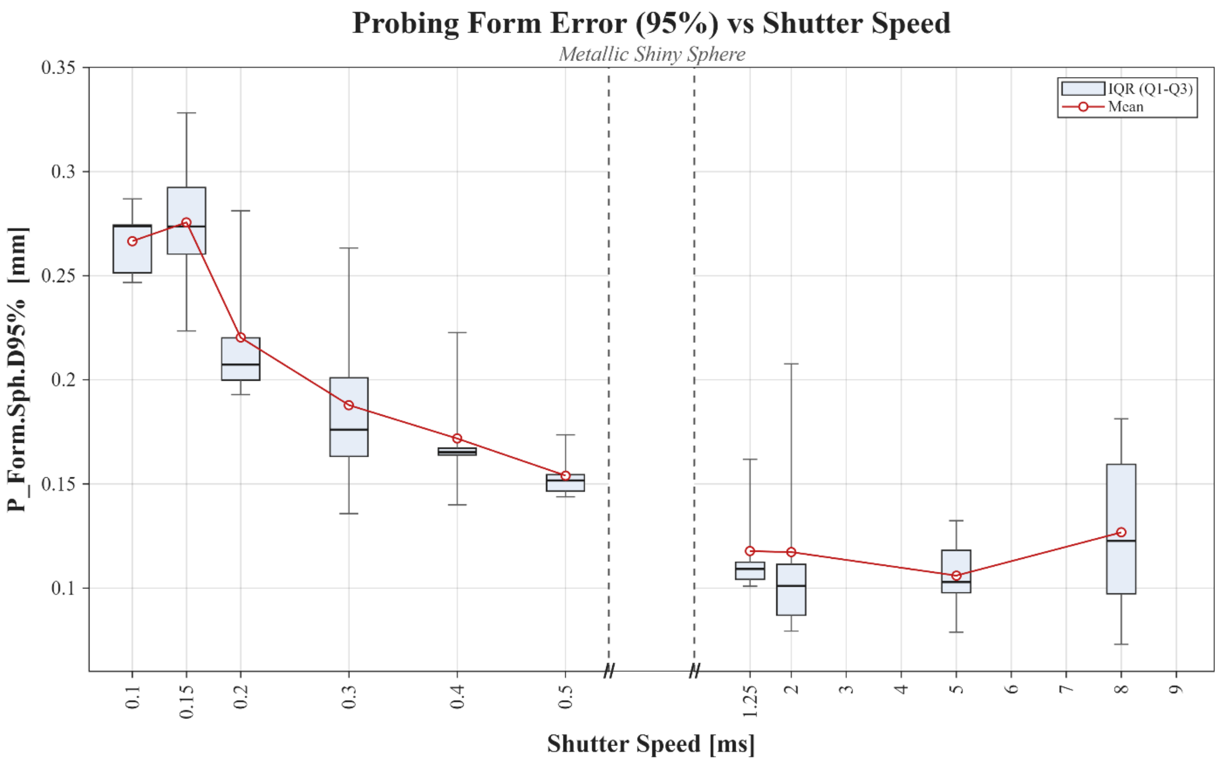

Figure 68. Metallic shiny sphere: $P_{Form.Sph.D95\%}$. as a function of shutter speed, box plot with mean values (red line) and split x-axis.

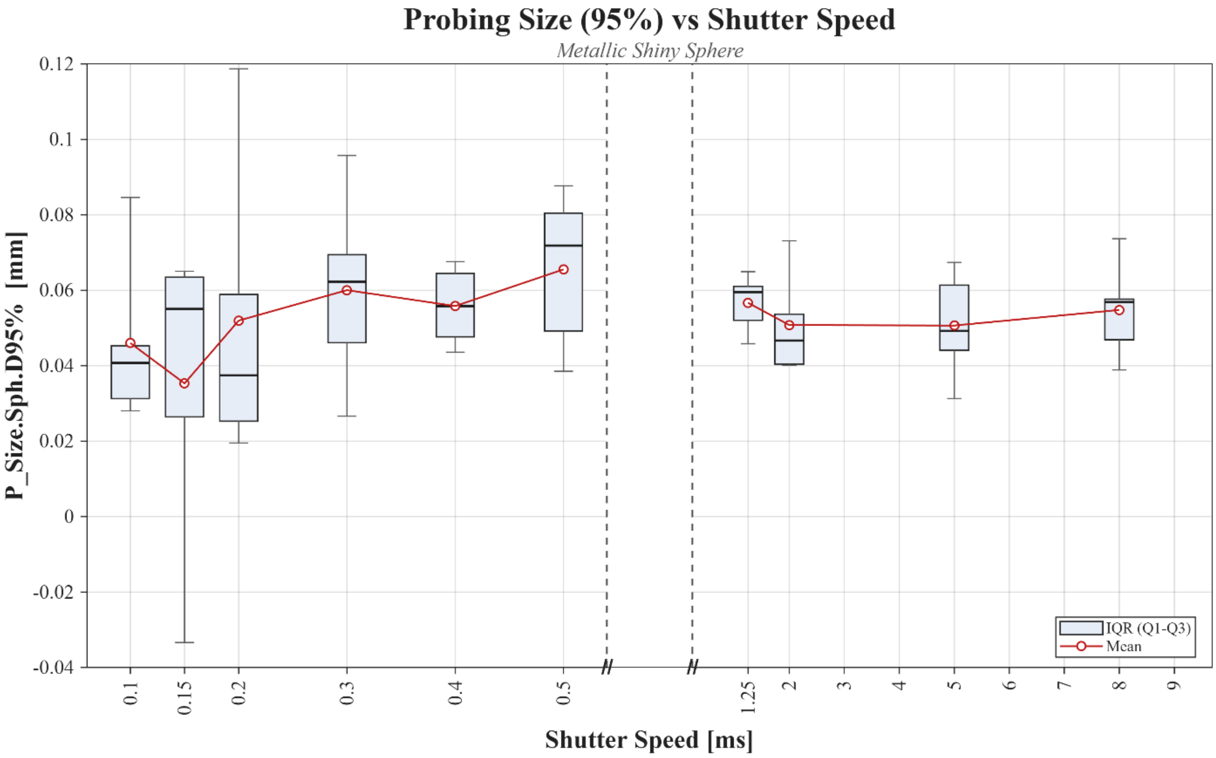

Figure 69. Metallic matte sphere: $P_{Size.Sph.D95\%}$. as a function of shutter speed, box plot with mean values (red line) and split x-axis.

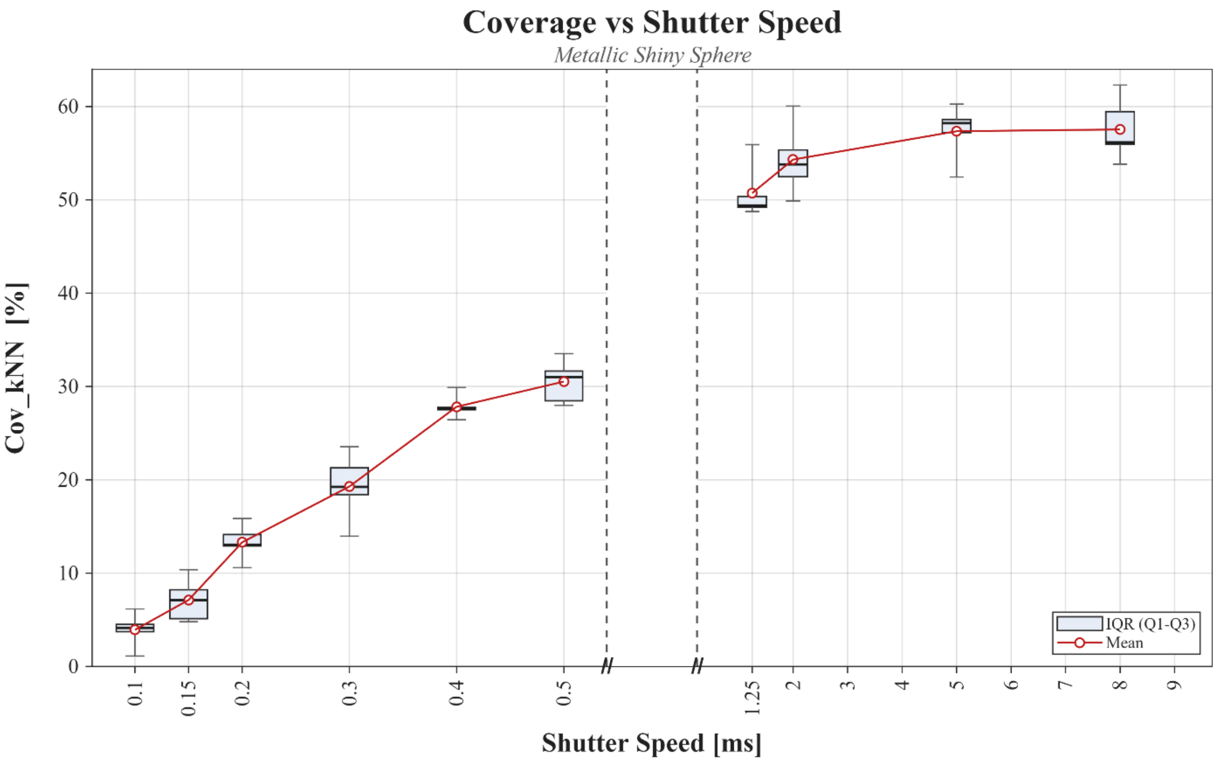

Figure 70. Metallic Shiny Sphere: Coverage (kNN method) as a function of shutter speed, box plot with mean values (red line) and split x-axis.

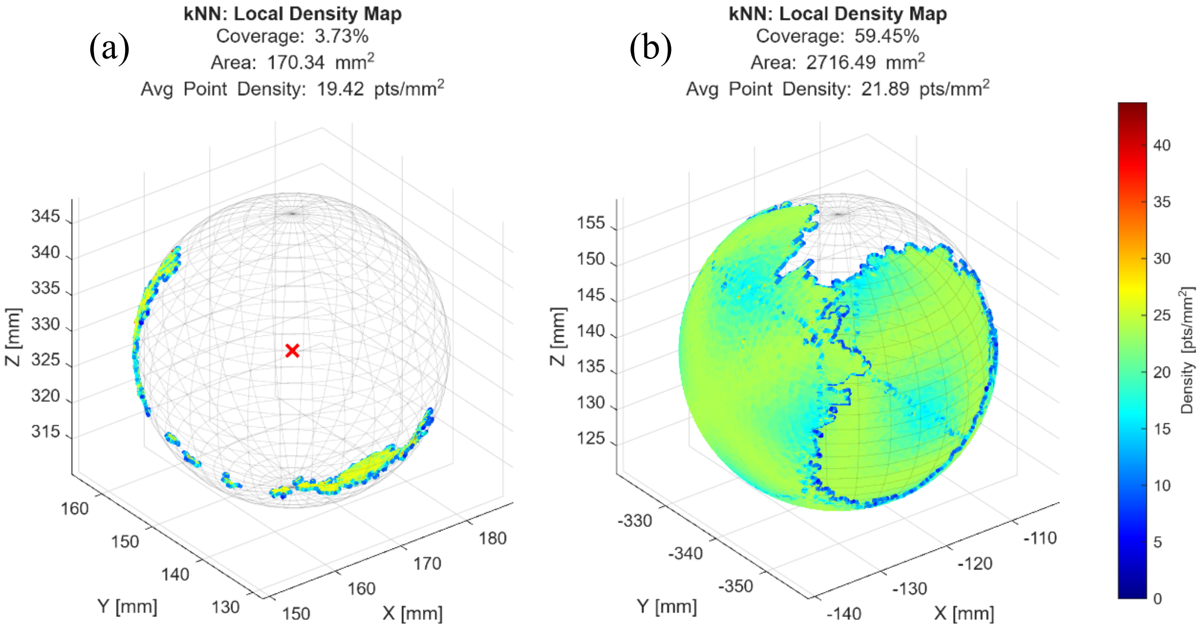

Figure 71. Metallic shiny sphere: Local point density and surface coverage on the metallic shiny sphere (kNN approach): (a) $t_{SH} = 0.10\ ms$*; (b)* $t_{SH} = 8\ ms$*.*

The values of the probing errors and coverage metrics for each shutter speed level are combined into the Score (Figure 72), following the procedure described in section 3.2.4 . The resulting quadratic fit is concave and shows the best theoretical shutter speed at $t_{SH}^{*} = 4.92\ ms$, with an optimal range of [3.564, 6.268] ms, which is defined as the region inside which the fitted score does not drop more than 0.05. The Monte Carlo simulation confirms a well-identified peak (874/1000 valid simulations), with median $t_{SH,MC}^{*} =$ 4.871 ms and a 68% confidence interval (± 1 standard deviation) of [4.066, 5.879] ms.

The identified optimal shutter speed range falls in the upper values of the HandySCAN range; this shows that highly specular metallic surfaces require longer exposure times to increase the number of points acquired and to reduce the $P_{Form.Sph.D95\%}$. The width of the Optimal Range (about 2.7 ms) indicates a moderate curvature of the parabola: the performance remains good over a relatively wide range around the peak. The high number of valid Monte Carlo simulations (874/1000) and the good correspondence between t_{SH}^{*} confirm that these results are robust to the observed experimental noise.

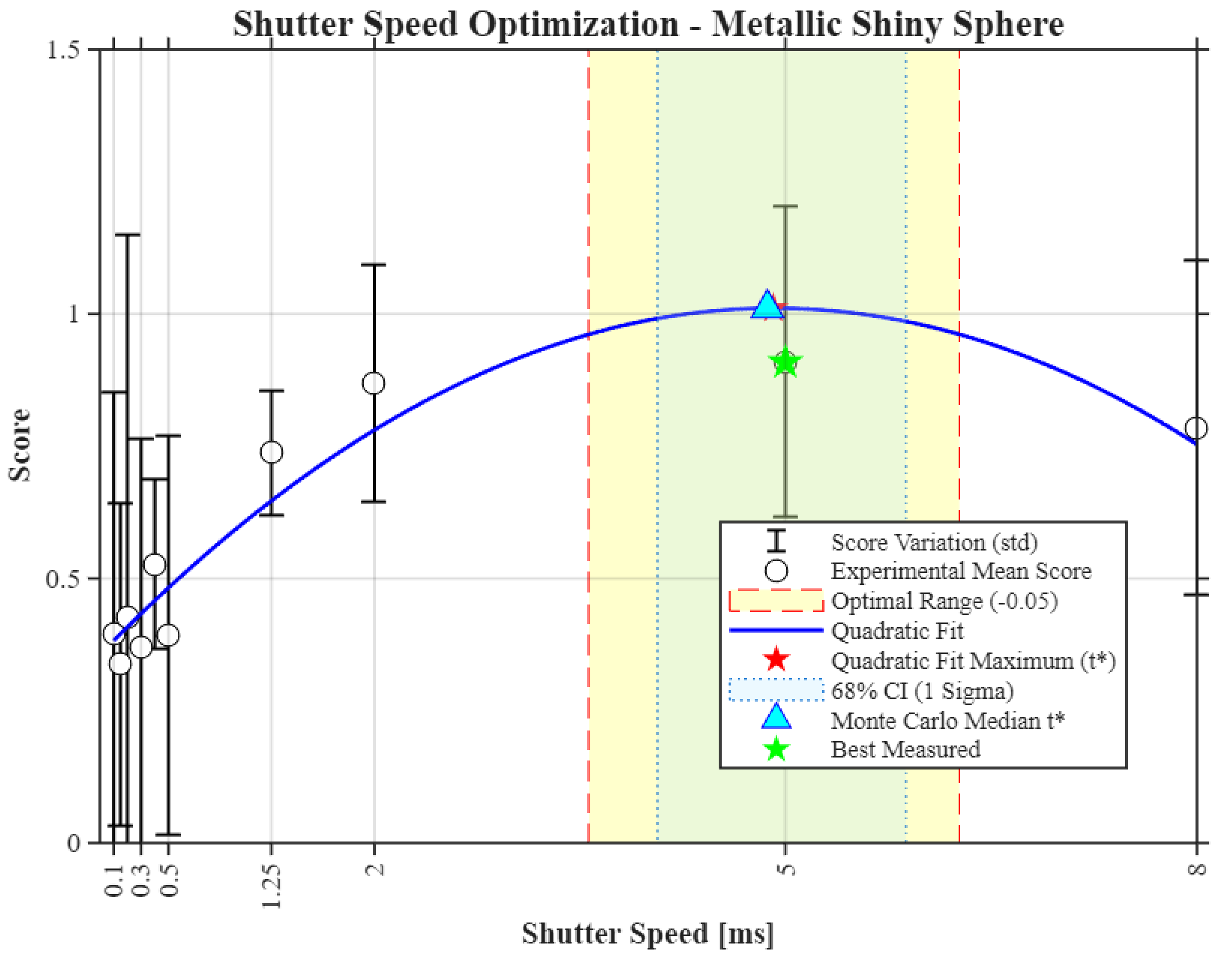

Figure 72. Score curve in function of shutter speed for the Metallic Shiny Sphere (AZ140), with quadratic fit, Monte Carlo median $(t^*_{SH,MC})$ *and 68% confidence interval.*

4.2.4 Billiard Glossy Sphere

The third sphere considered for the shutter optimization is the billiard glossy sphere, corresponding at sphere 1 of the billiard ball beam described in 3.1.1 . A total of 50 measurements were performed on this sphere, corresponding to 5 repeated measurements for each of the 10 shutter speed levels, according to the procedure described in section 3.2.1 . The performance metrics results for each level (mean ± standard deviation) are reported in Table 39.

t_{SH} / ms	$P_{Size.Sph.D95\%}$ / mm	$P_{Form.Sph.D95\%}$ / mm	Coverage / %	Point Density / pt/mm^2
0.10	-0.062 ± 0.009	0.080 ± 0.006	61.05 ± 3.93	21.77 ± 0.11
0.15	-0.056 ± 0.010	0.078 ± 0.006	65.26 ± 3.16	21.87 ± 0.04
0.20	-0.056 ± 0.011	0.073 ± 0.003	66.00 ± 2.18	21.91 ± 0.06
0.30	-0.053 ± 0.012	0.073 ± 0.004	68.31 ± 1.99	21.93 ± 0.04
0.40	-0.048 ± 0.010	0.076 ± 0.007	71.69 ± 10.91	21.96 ± 0.04
0.50	-0.057 ± 0.013	0.073 ± 0.003	69.12 ± 2.65	21.95 ± 0.05
1.25	-0.049 ± 0.015	0.075 ± 0.007	70.93 ± 2.70	21.93 ± 0.06
2.00	-0.066 ± 0.010	0.104 ± 0.007	69.39 ± 2.52	21.89 ± 0.06
5.00	-0.060 ± 0.015	0.149 ± 0.013	52.08 ± 20.61	20.42 ± 0.65
8.00	-0.024 ± 0.018	0.222 ± 0.036	13.16 ± 10.23	18.49 ± 0.60

Table 39.Billiard glossy sphere: performance metrics in function of the shutter speed (mean ± st. dev., n = 5)

The probing size error $P_{Size.Sph.D95\%}$ is consistently negative in the whole t_{SH} range, indicating a systematic underestimation of the sphere diameter. Its value remains relatively stable, between 0.1 ms and 5 ms, ranging between -0.048 and -0.066 mm, and improves at t_{SH} equal to 8 ms where it drops to -0.024 mm, as it is shown in Figure 73. The probing form error $P_{Form.Sph.D95\%}$ follows instead a much clearer trend: it presents low and stable values, between 0.073 and 0.080 mm, in the range between 0.1 and 1.25 ms, and then it rapidly increases, following a monotonic trend, until reaching a value of 0.222 mm at the highest shutter speed. This behaviour indicates that excessively high values of shutter speeds, i.e. exposure times, affect the measurements of highly reflective glossy surface by introducing additional noise.

The coverage and point cloud density metrics exhibit a completely different behaviour with respect the metallic shiny sphere. The coverage presents a rapid monotonic increase from 61.05% at 0.10 ms to a maximum value of 70.93% at 1.25 ms, then for higher shutter speed this metric follows a progressive decrease reaching a mean value of 13.16% at t_{SH} of 8 ms.

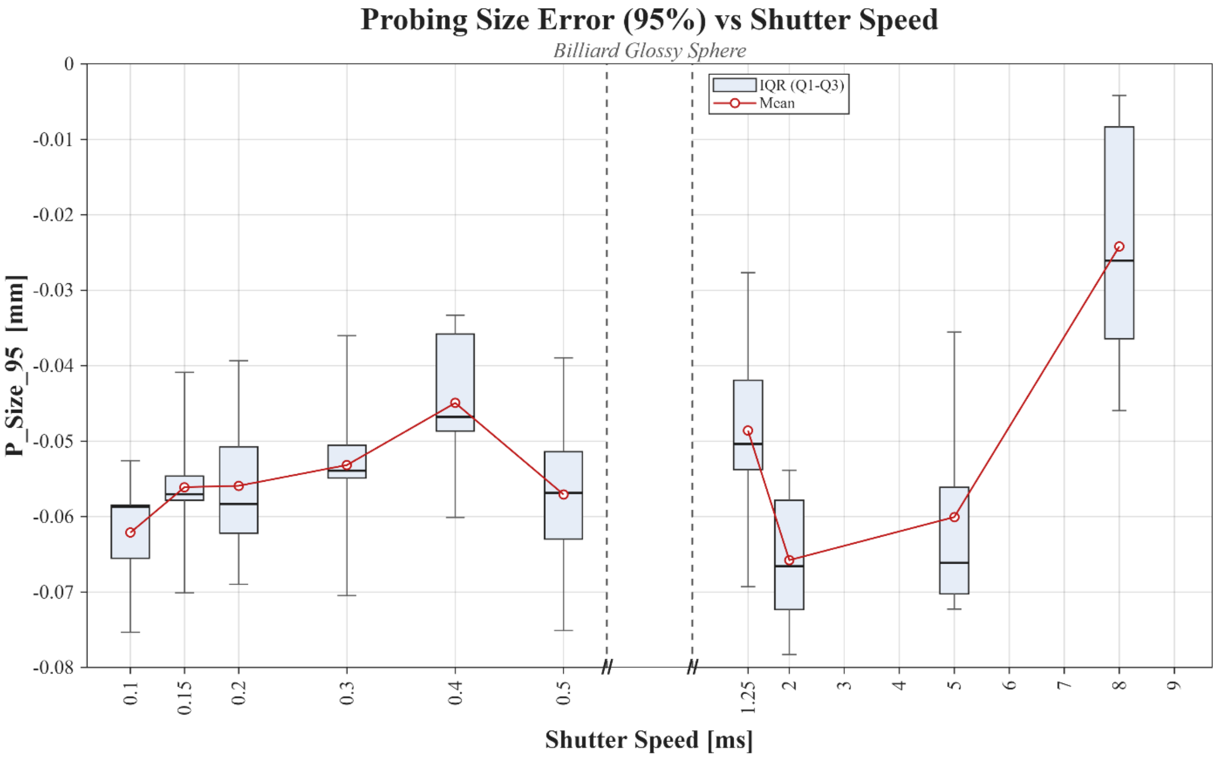

Figure 73. Billiard glossy sphere: $P_{Size.Sph.D95\%}$. as a function of shutter speed, box plot with mean values (red line) and split x-axis.

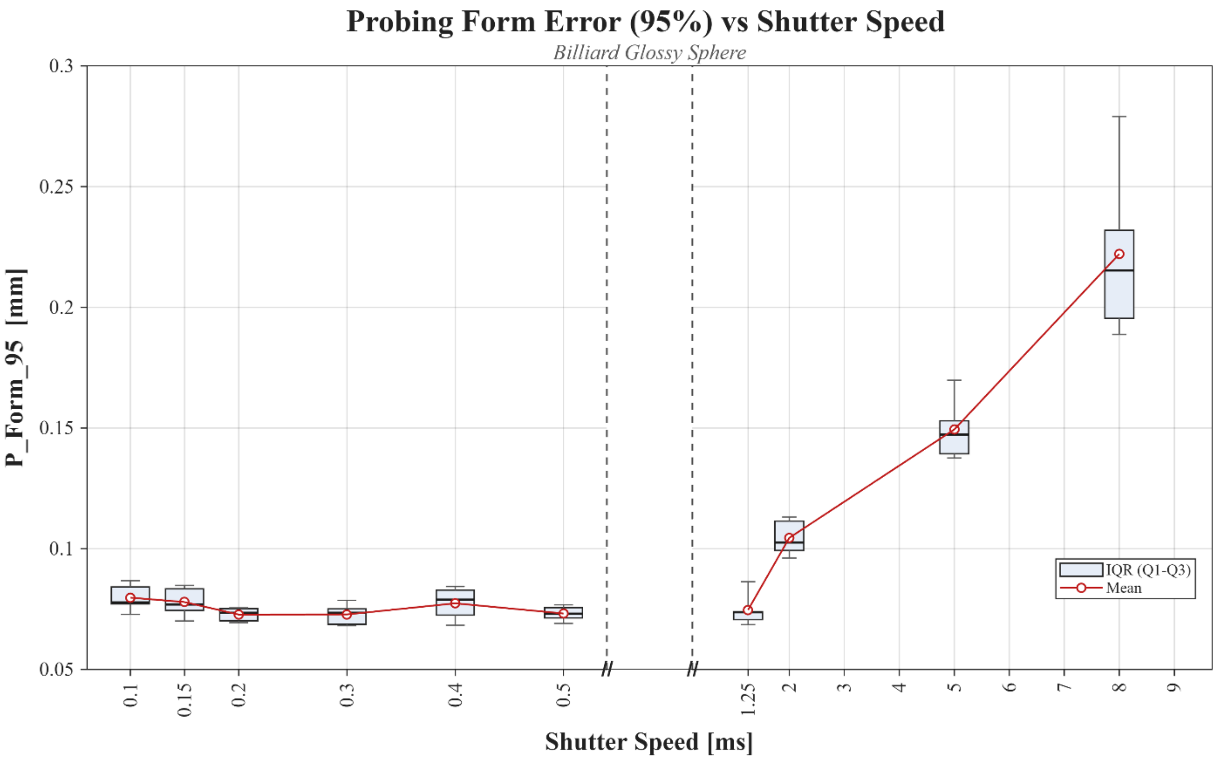

Figure 74. Billiard glossy sphere: $P_{Form.Sph.D95\%}$. as a function of shutter speed, box plot with mean values (red line) and split x-axis.

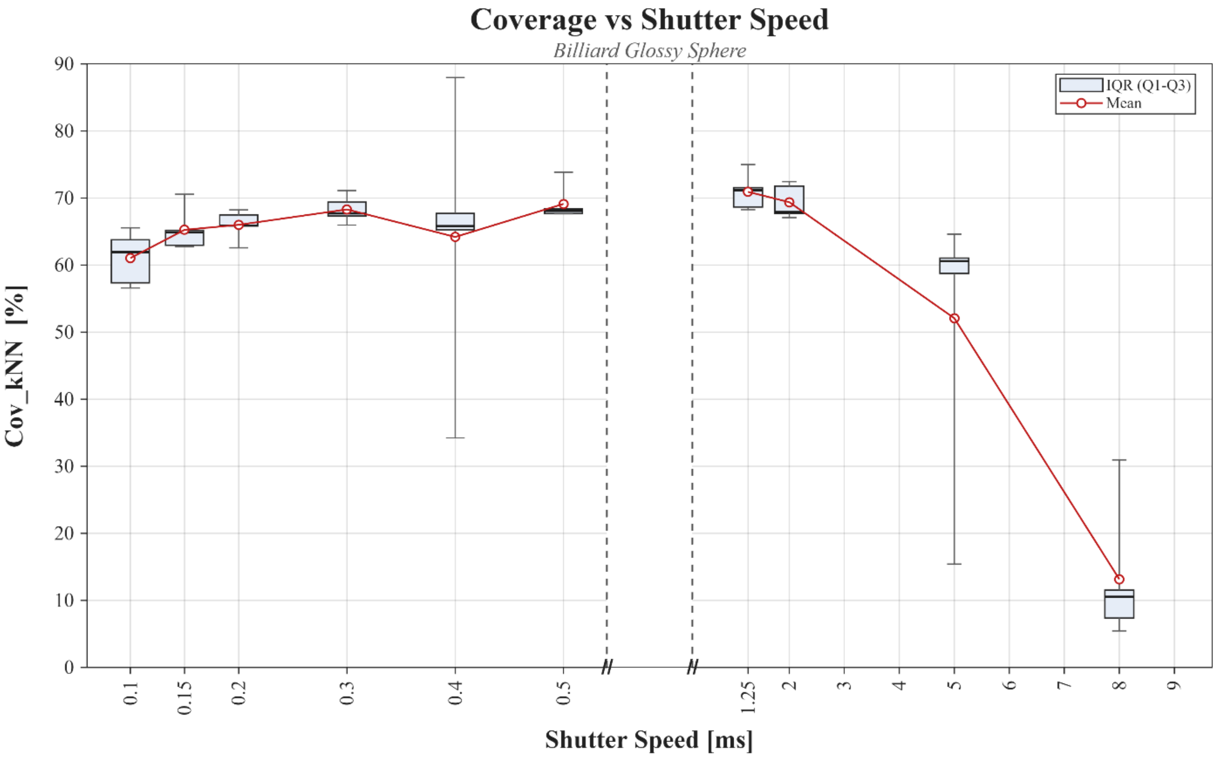

Figure 75. Billiard glossy sphere: Coverage as a function of shutter speed, box plot with mean values (red line) and split x-axis.

As for the other analysed spheres, the probing errors and coverage results are combined to evaluate a score value for each shutter speed level, over which a representative score curve is fitted (Figure 76), following the procedure in section 3.2.4 . Differently from the other cases previously discussed, the quadratic fit produces a convex parabola, which consequently cannot identify a peak.

As described in section 3.2.4 , the highest Score mean score observed is therefore reported as the best operating point, corresponding to t_{SH} = 1.25 ms (Score = 0.775), closely followed by t_{SH} = 0.40 ms (Score = 0.772); the difference between the two values is not statically significant given the experimental dispersion, this suggest there is an interval of good performance rather that a clear optimum shutter speed.

The Monte Carlo simulation was performed using the same procedure as for the other cases, and it showed coherent results with this analysis. Only 76 iterations out of 1000 yield a valid concave fit with the vertex inside the tested range, this number is considerably lower than the analysis performed on the metallic spheres. The low number of valid simulations indicates that the score peak is not clearly identifiable from the collected data, due to the experimental dispersion with respect to the curvature of the parabola. From the valid simulated curves, the median optimal shutter speed $t^*_{SH,MC}$ is found to be equal to 1.242 ms, with a level of confidence of 68% within interval of [0.501, 1.920] ms. The low number of valid simulations, combined with the wide confidence interval, is itself a significant result: it indicates that the Score curve for the glossy billiard ball does not exhibit a single, sharply defined optimum, but rather a region of comparable performance extending from approximately 0.3 ms to 1.25 ms, with a clear worsening just for high shutter speed values.

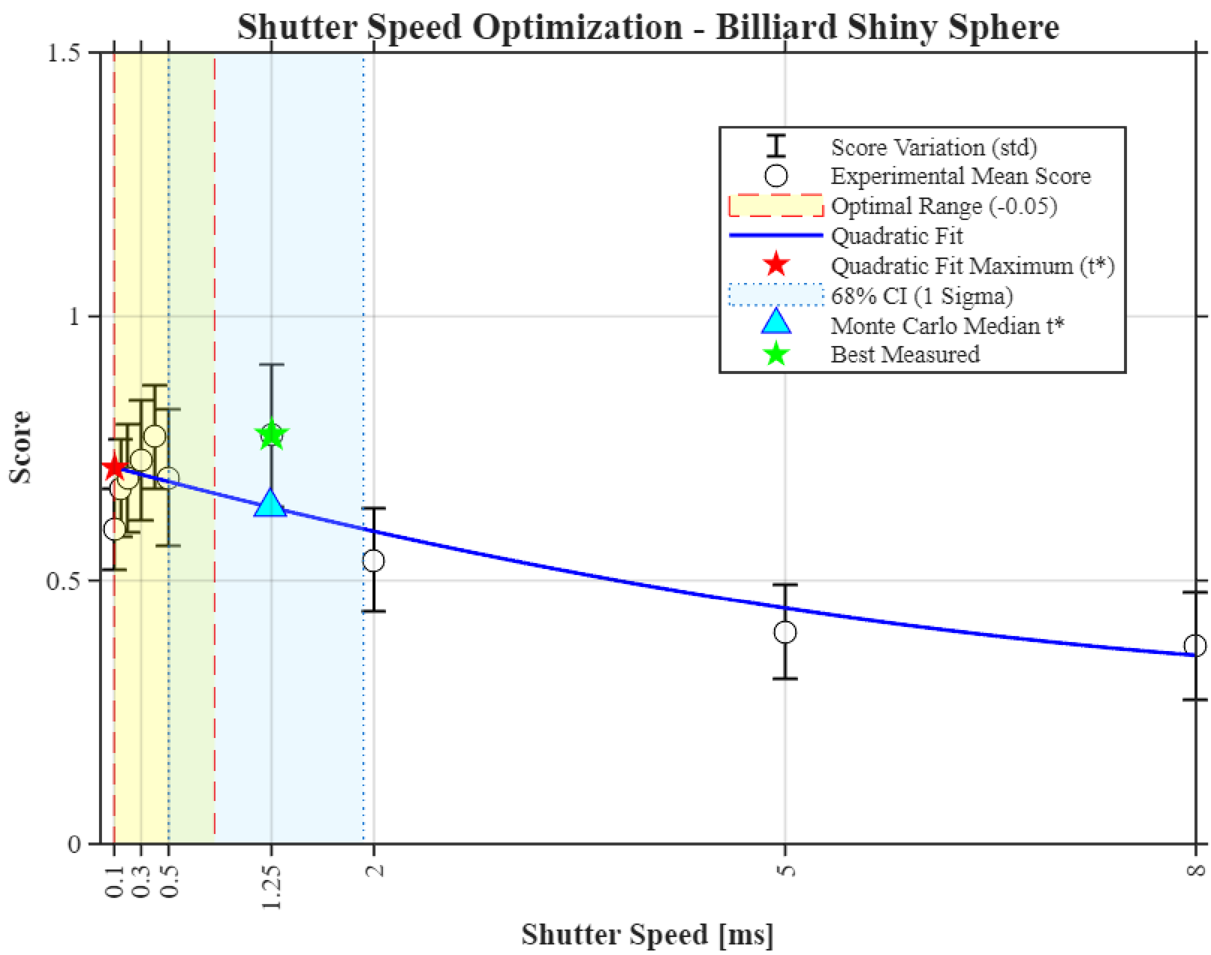

Figure 76. Score curve in function of shutter speed for the Billiard Glossy Sphere, with quadratic fit, Monte Carlo median ($t^*_{SH,MC}$) and 68% confidence interval.

4.2.5 Billiard Mattified Sphere

The last case considered for the shutter speed optimization is the mattified billiard sphere, obtained applying a mattifying coating on the same glossy billiard ball described in the previous section. The sphere was measured following the procedure described in section 3.2.1 , for a total of 50 individual point clouds, corresponding at 5 scans for each of the 10 shutter speed levels. Table 40 reports the average value and the standard deviation of the 4 considered performance metrics for each level. During the analysis of the point clouds, the first repetitions at the shutter speed levels of 0.15, 0.20, 0.30, 0.40, 2.00, 5.00 and 8.00 ms were identified as an outlier, showing a probing form error or probing size error one to two orders of magnitude higher than the other repetitions at the same level; the deviation map shown in Figure 77 is an example of an excluded measurement (specifically the first repetition for shutter speed 0.20 ms), while all other conditions being unchanged. These seven measurements were therefore excluded from the dataset, resulting in n = 4 at the affected levels and n = 5 at the remaining ones. Table 40 reports the average value and the standard deviation of the 4 considered performance metrics for each level, computed on the cleaned dataset.

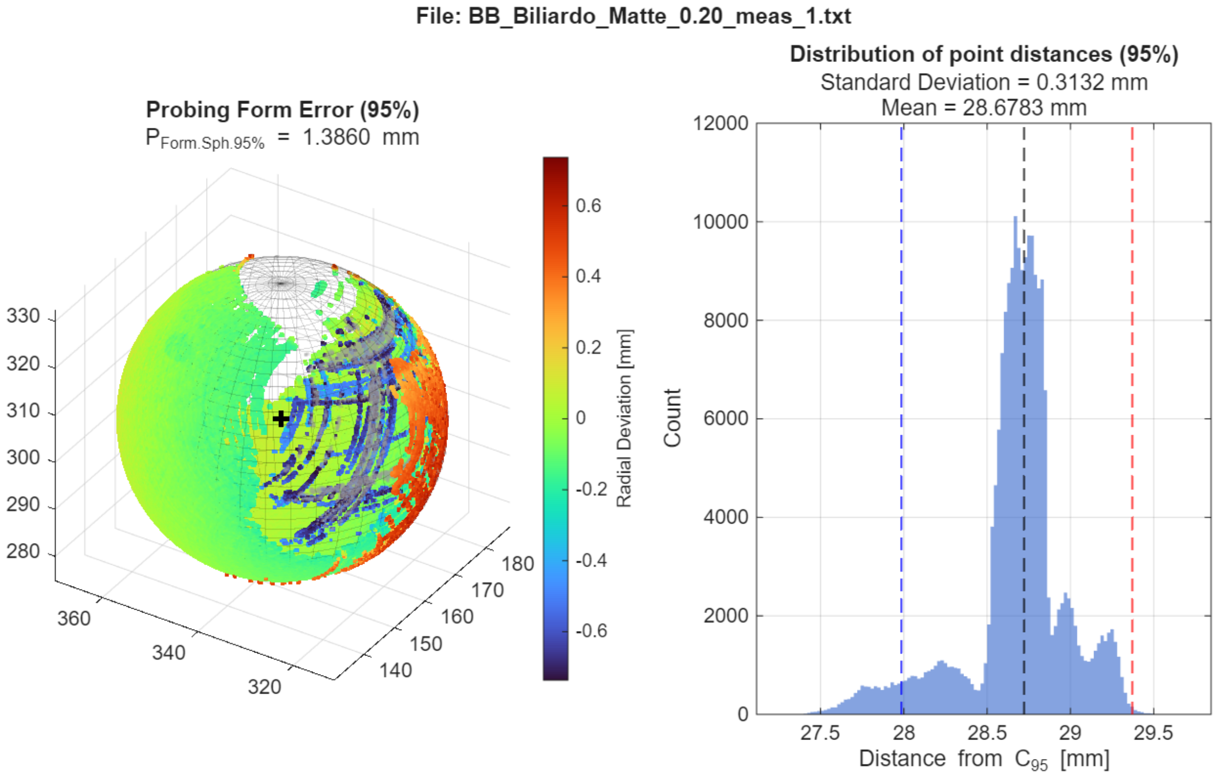

Figure 77. Form deviation map and point distance distribution for the excluded repetition at t_{SH} = 0.20 ms (first measurement), showing scanning artefacts responsible for the anomalous probing form error.

t_{SH} / ms	$P_{Size.Sph.D95\%}$ / mm	$P_{Form.Sph.D95\%}$ / mm	Coverage / %	Point Density / pt/mm^2
0.10	0.034 ± 0.010	0.063 ± 0.004	64.88 ± 1.65	21.93 ± 0.05
0.15	0.028 ± 0.008	0.065 ± 0.003	67.22 ± 1.84	21.96 ± 0.04
0.20	0.035 ± 0.004	0.063 ± 0.004	67.92 ± 2.34	21.96 ± 0.05
0.30	0.031 ± 0.008	0.063 ± 0.002	68.34 ± 0.79	21.94 ± 0.04
0.40	0.041 ± 0.010	0.066 ± 0.006	68.35 ± 1.02	21.96 ± 0.05
0.50	0.034 ± 0.004	0.062 ± 0.004	68.94 ± 2.56	21.95 ± 0.09
1.25	0.036 ± 0.004	0.080 ± 0.028	69.66 ± 0.88	21.97 ± 0.07
2.00	0.036 ± 0.003	0.078 ± 0.009	69.64 ± 1.49	21.90 ± 0.02
5.00	0.034 ± 0.009	0.109 ± 0.009	64.94 ± 7.86	21.45 ± 0.32
8.00	0.041 ± 0.013	0.122 ± 0.011	35.54 ± 19.25	20.04 ± 1.14

Table 40. Billiard mattified sphere: performance metrics in function of the shutter speed (mean ± st. dev., n = 5, n = 4 at 0.15, 0.20, 0.30, 0.40, 2.00, 5.00 and 8.00 ms)

The probing size error $P_{Size.Sph.D95\%}$ (Figure 78) remains low and close to zero for most shutter speed levels, with values ranging from 0.028 mm to 0.041 mm, without showing a clearly monotonic trend, and remains positive across the entire shutter speed range. This trend is consistent with what was observed for the glossy billiard ball, where the probing size error also remains relatively stable up to 5 ms and then shows a more marked variation at the extreme level.

After removing the outlier repetitions, the probing form error $P_{Form.Sph.D95\%}$ shows a much more consistent behaviour than in the raw dataset. As it can be seen in Figure 79, it remains low and stable, between 0.062 mm and 0.080 mm, for all shutter speed levels between 0.10 and 2.00 ms. Only at 5.00 and 8.00 ms does the error increase, reaching 0.109 mm and 0.122 mm respectively, together with a moderate increase in the standard deviation. This behaviour is consistent with what was already observed for the glossy billiard sphere, where excessively high shutter speed values were found to worsen the measurement quality on reflective surfaces;

the mattifying coating appears to shift this degradation to somewhat higher shutter speed values, without removing it entirely.

The coverage and point density metrics follow instead a more regular trend across most of the tested range. In particular, the coverage increases from 64.88% at 0.10 ms up to values around 68-70% between 0.30 and 2.00 ms, remaining substantially stable in this region; it then decreases to 64.94% at 5.00 ms and drops sharply to 35.54% at 8.00 ms, with a very high standard deviation (19.25%) that reflects the poor repeatability of the acquisitions at this level. The point density follows the same qualitative trend, but with a much smaller relative variation, in line with what was already observed for the other spheres: it remains close to 21.9 pt/mm² for almost all levels, then drops to 20.04 pt/mm² at 8.00 ms.

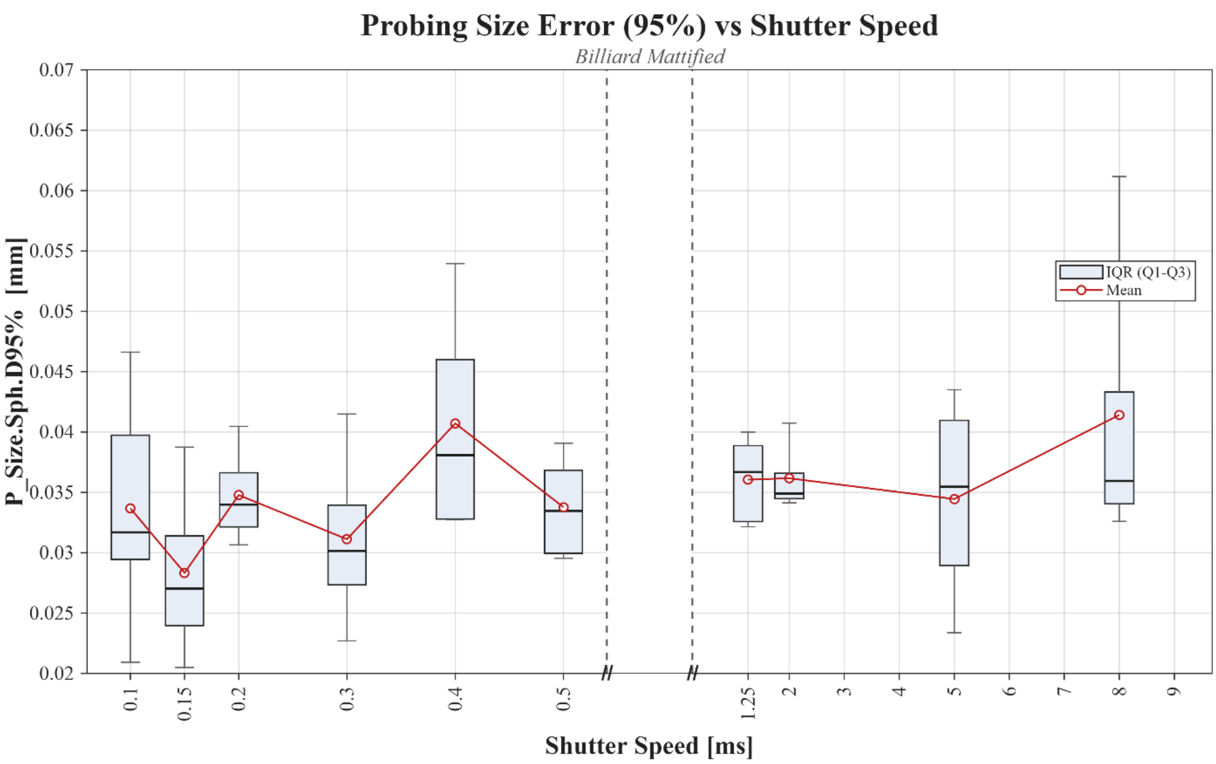

Figure 78. Billiard mattified sphere: $P_{Size.Sph.D95\%}$. as a function of shutter speed, box plot with mean values (red line) and split x-axis.

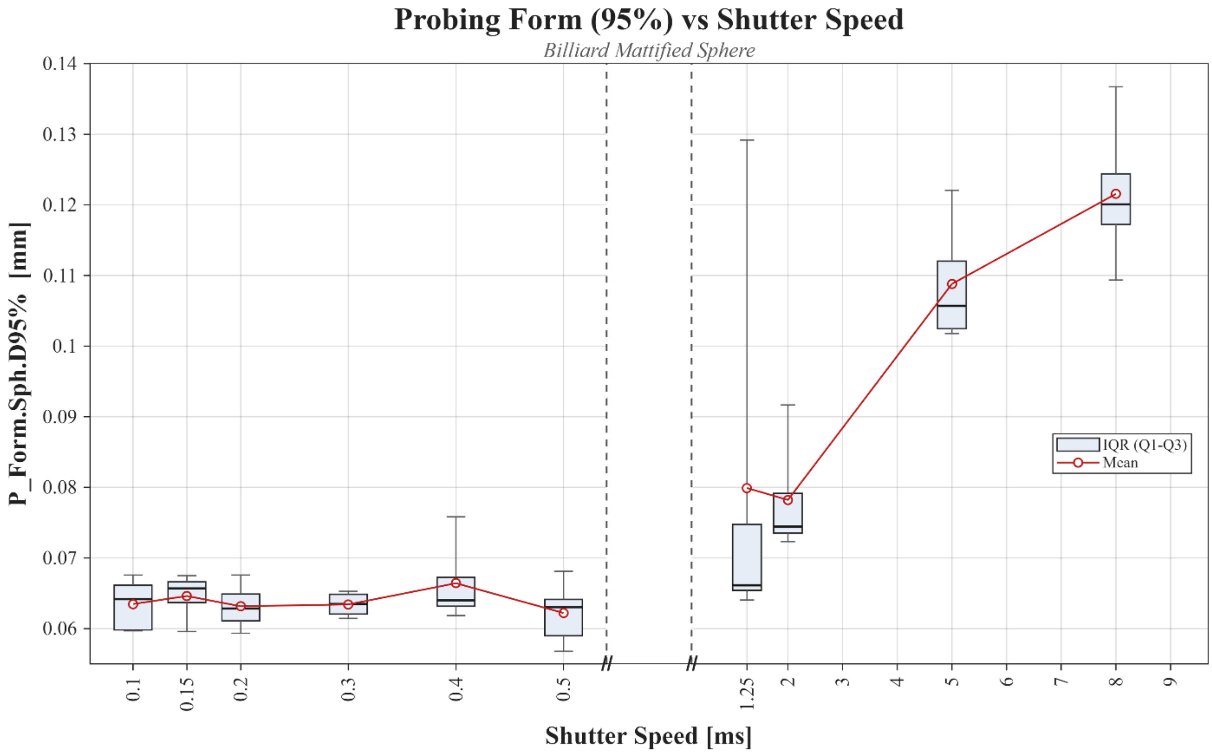

Figure 79. Billiard mattified sphere: $P_{Form.Sph.D95\%}$. as a function of shutter speed, box plot with mean values (red line) and split x-axis.

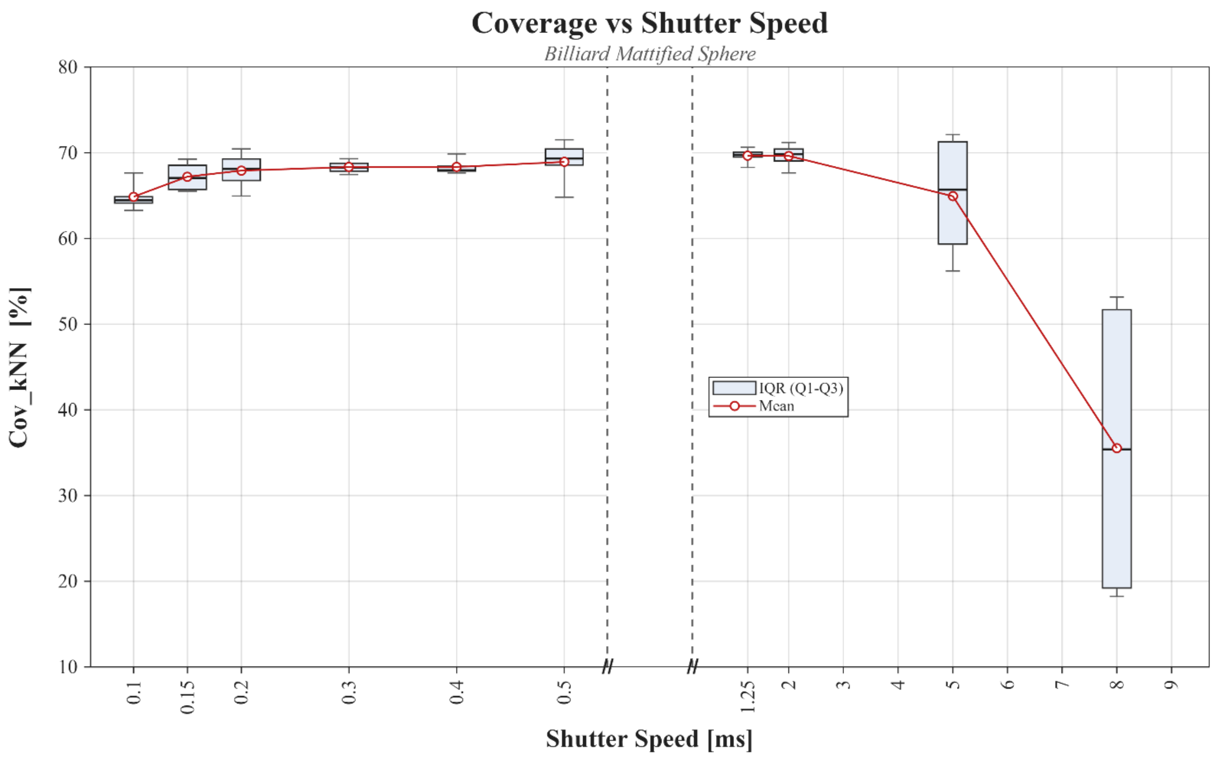

Figure 80. Billiard mattified sphere: Coverage (kNN method) as a function of shutter speed, box plot with mean values (red line) and split x-axis.

The values of the probing errors and of the coverage metric for each shutter speed level are combined to compute the Score curve (Figure 81), following the procedure described in section 3.2.4. The quadratic fitting results in a concave parabola, but its theoretical vertex is outside the HandySCAN possible range, which means it does not identify a peak.

As described in section 3.2.4 , the best available operating point is therefore reported as the shutter speed level with the highest observed Score, corresponding to t_{SH} = 0.10 ms (Score = 0.818). The Optimal Range, defined as the region where the fitted Score stays within 0.05 points from its maximum, extends from 0.10 to 1.00 ms, indicating that good performance is maintained over the lower portion of the tested range rather than being concentrated around a single value.

The Monte Carlo simulation, performed following the same procedure described in section 3.2.4, is consistent with this result: only 303 iterations out of 1000 produce a valid concave fit with the vertex inside the tested range, a relatively low number that confirms the absence of a sharply defined peak for this surface condition. From the valid simulations, the median optimal shutter speed is $t^*_{SH,MC}$ = .90 ms, with a 68% confidence interval of [0.80, 2.63] ms. As for the billiard glossy sphere, the low number of valid simulations, together with the fact that the median falls outside the deterministic Optimal Range, suggests that the $t^*_{SH,MC}$ value should be interpreted as a robustness indicator rather than a reliable estimate of the optimal shutter speed. Combined with the concave shape of the deterministic fit, these results indicate that the mattified sphere maintains good performance over a broad range of low-to-intermediate shutter speed values, without a single, sharply defined optimum

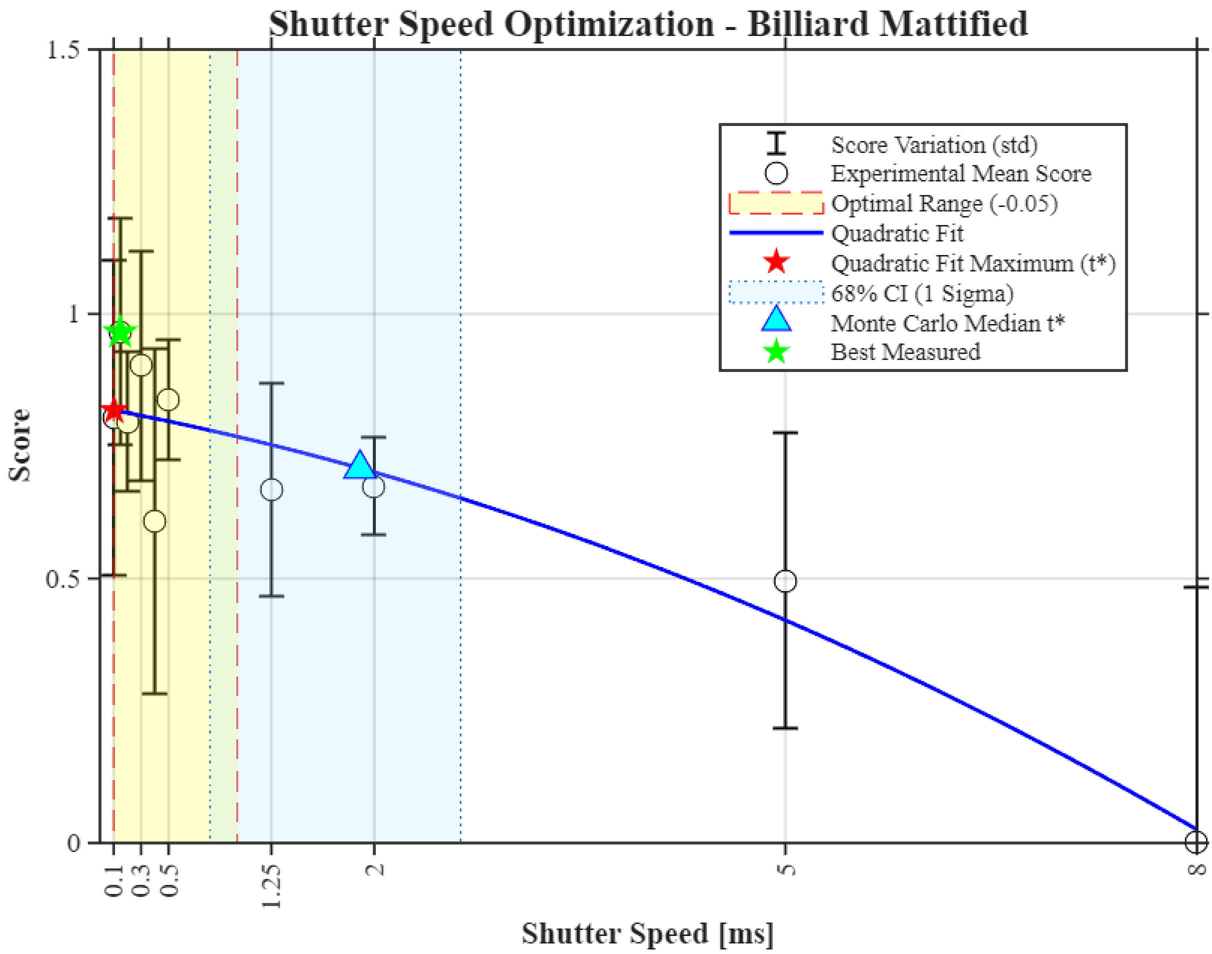

Figure 81. Score curve in function of shutter speed for the Billiard Mattified Sphere, with quadratic fit, Monte Carlo median and 68% confidence interval

4.2.6 Comparison and Discussion

For the shutter speed optimization four different surface cases were measured at different shutter speed (t_{SH}) levels: two metallic spheres, one of which with matte (cooperative surface) and one shiny (non-cooperative surface with high specular reflection), and one billiard sphere, measured both without any coating (highly reflective and slightly translucent) and after the application of a matte white spray coating. From the measurement data, at each shutter speed level, and for each case separately, a score is evaluated using as metrics the probing errors with priority I (corresponding to weight 0.375) and the coverage evaluated through the kNN method, with assigned priority II (corresponding to weight 0.250).

For the two metallic spheres, matte and shiny, the quadratic fit (performed on the score values in function of t_{SH}) is concave and it identifies a well-defined optimal shutter speed t_{SH}^*, at 3.18 ms and 4.92 ms respectively. The billiard mattified sphere shows also a concave quadratic fitting, but, as the theoretical vertex falls outside the shutter speed range, for the optimal shutter speed is reached at t_{SH}^* = 0.10 ms. On the other hand, the billiard glossy sphere presents a convex fit with no peak, so that its best available operating point is also reported at the lowest tested shutter speed level t_{SH}^* = 0.10 m, but for a different reason. The main results of the shutter speed optimization for the four surface conditions are summarized in Table 41.

Sphere	Optimal t_{SH}^* / ms	Optimal t_{SH} Range / ms	Valid Monte Carlo curves (n/1000)	$t_{SH,MC}^*$ (median) / ms	68% CI / ms
Metallic Matte	3.18	[1.17, 5.18]	628	3.51	[2.27, 4.91]
Metallic Shiny	4.92	[3.56, 6.27]	874	4.87	[4.07, 5.88]
Billiard Glossy	0.10	[0.10, 0.83]	74	1.26	[0.65, 2.03]
Billiard Mattified	0.10	[0.10, 1.00]	303	1.90	[0.80, 2.63]

Table 41. Summary of the shutter speed optimization results for the four surface conditions

The Monte Carlo results show that the degree of definition of the peak depends on more than just the concave-versus-convex distinction. It also depends on how close the fitted vertex is to the tested range. The number of valid iterations is high for the two metallic spheres (628 and 874 out of 1000), where the vertex lies well inside the tested interval. It drops sharply for the billiard glossy sphere (74 out of 1000), which is convex, and for the billiard mattified sphere (303 out of 1000), which is concave but with the vertex located outside the tested range. A low number of valid simulations therefore signals a poorly constrained optimum, whether this is caused by the absence of an internal vertex or by its closeness to the edge of the tested range.

It is important to notice that the quadratic model in some cases struggles to follow the observed Score trends. A quadratic fit was chosen for its simplicity and because it gives a direct analytical estimate of the optimum. Future work could test alternative fitting strategies, such as higher-order polynomials, spline-based or non-parametric regression, or robust fitting methods less sensitive to outliers, and check whether these methods are better representing the observed Score trends, giving a more reliable estimate of the optimal shutter speed range.

A comparison of the probing error trends across the four surface conditions further clarifies the different behaviour of metallic and billiard surfaces with respect to shutter speed.

The probing size error shows a clear sign pattern linked to the surface type. It is positive for both metallic spheres, negative for the uncoated billiard sphere, and also positive, though smaller in magnitude, for the mattified sphere. This suggests that the systematic underestimation of the diameter on the glossy surface is related to its specular reflection, and that the mattifying coating removes this systematic offset, bringing the probing size error back to values close to those of the metallic spheres. The probing form error reaches its minimum at very different shutter speed values depending on the surface: at intermediate-to-high t_{SH} for the metallic spheres, and at low t_{SH} for both billiard spheres. This mirrors the same pattern already seen for the position of the Score optimum.

The coverage trend follows two distinct patterns across the four surface conditions. For the metallic spheres, coverage increases monotonically and progressively saturates towards a plateau: for the metallic shiny sphere this increase is particularly steep, rising from 3.93% at 0.10 ms to 57.54% at 8.00 ms, while for the metallic matte sphere the same trend is present but much less pronounced, since coverage is already relatively high at the lowest shutter speed level (58.21%) and reaches a plateau around 67-71% already at intermediate t_{SH} values. For the billiard spheres, both glossy and mattified, coverage instead follows a non-monotonic trend: it increases rapidly at low shutter speed, reaches a maximum around 0.40-1.25 ms, and then decreases sharply at the highest levels, dropping to 13.16% at 8.00 ms for the uncoated sphere and to 35.54% for the mattified one.

A possible explanation for this different behaviour can be related to the working principle of the laser triangulation sensor, which acquires a point only where a sufficient amount of reflected light reaches the sensor. On the metallic spheres, characterized by a relatively small radius and consequently a rapidly varying surface slope with respect to the scanner line of sight, the amount of light collected decreases quickly moving away from the region facing the sensor; at low shutter speed, the exposure time may therefore be too short to collect enough signal from the more inclined regions of the surface, resulting in a lower coverage, which then increases with shutter speed as more light is progressively integrated. On the billiard spheres, on the other hand, the lighter surface colour is likely associated with a higher diffuse reflectivity, which could explain why a high coverage is already reached at low shutter speed; the subsequent drop observed at the highest shutter speed levels would then be consistent with sensor saturation caused by an excessive amount of collected light, leading to a loss of usable points in the overexposed regions.

It should be noted that this interpretation, based on general considerations on the acquisition principle of the sensor, has not been directly verified within this work, and other factors related to the surface finish, such as the difference in surface roughness between the two sphere types, likely also play a role in the observed coverage trends. A dedicated experimental campaign, for example based on reflectivity or BRDF measurements of the tested surfaces combined with a systematic variation of the shutter speed, would be needed to isolate and confirm the individual contribution of surface slope, diffuse reflectivity, and overexposure to the observed coverage behaviour, and is left as a possible direction for future work.

The mattifying coating changes the shape of the Score curve from convex, as observed for the uncoated glossy sphere, to concave, although with a vertex located outside the lower boundary of the tested range. It also improves the overall performance, with the maximum fitted Score observed for the mattified sphere (0.818) markedly higher than for the uncoated glossy sphere (0.714), and the best individually measured Score following the same pattern (0.818 against 0.775, both close to their respective fitted maxima). The degradation at high shutter speed values is comparable in shape between the two conditions but shifted to somewhat higher values for the mattified sphere. This confirms that the mattifying spray is effective in reducing the specular reflection responsible for the higher probing form error observed on the uncoated glossy surface, without introducing a substantially different sensitivity to shutter speed. This finding is also consistent with the sign of the probing size error discussed above, which shifts from systematically negative on the glossy sphere to close-to-zero, alternating in sign, on the mattified one.

Point Density, introduced in section 3.2.3 as a completeness metric complementary to Coverage, was not included in the Score computation (section 3.2.4). Across all four surface conditions tested, Point Density shows a strong positive correlation with Coverage as a function of shutter speed, with Pearson correlation coefficients ranging between 0.88 and 0.98, while showing a much smaller relative variation. This behaviour is a direct consequence of the fact that the HandySCAN outputs a triangulated mesh at a resolution set by the user, rather than a raw point cloud of variable density: the local point density is therefore constrained by the mesh resolution itself and remains nearly constant over the acquired surface, except at the boundary regions of the point cloud, while it is Coverage that actually reflects how much of the sphere is reconstructed at a given shutter speed level. Including Point Density in the Score would therefore introduce information that is largely redundant with Coverage, without adding real discriminating power between shutter speed levels. This consideration is specific to the class of instruments to which the HandySCAN belongs, and would not necessarily extend to sensors that natively output a non-uniform point cloud, for which Point Density could constitute an independent and informative completeness metric.

Overall, these results indicate that the optimal shutter speed range strongly depends on the surface finish of the measured object: cooperative and moderately reflective surfaces, such as the metallic matte and metallic shiny spheres, benefit from an intermediate-to-high shutter speed to minimize the probing errors, while highly specular non-cooperative surfaces, such as the uncoated billiard sphere and its mattified counterpart, perform best at low-to-intermediate shutter speed values, with a marked degradation only at the highest levels tested. This confirms that a single fixed shutter speed value cannot be recommended for all surface conditions, and that the choice should instead be adapted to the reflectivity of the object being measured.

Chapter 5: Conclusions and Future Outlooks

This thesis aims to address two distinct objectives. The first is the proposal of a rigorous adaptation for the ISO 10360-13:2021 standard to evaluate the metrological performances of a *handheld multi-line laser-based sensor*, a class of instruments for which no dedicated international standard exists; the proposed methods are then effectively applied in the performance verification of a HandySCAN SILVER. The second objective focuses on the study of the *shutter speed*, an acquisition parameter of the instrument just introduced that regulates the exposure time of sensors, and how it influences the quality of the acquired data on both cooperative and non-cooperative surfaces.

To meet these objectives, the work was divided in two phases:

- The definitions of four new scanning strategies, CMV.A, CMV.B, CMV.C and CMV.D, in order to adapt the measurement methods presented in the ISO10360-13:2021 to the dynamic behaviour of handheld laser-line scanners, and then the subsequent evaluation of the distortion error, the probing size and form errors, the flat-form distortion errors and the volumetric length measurement errors (Chapter 2:);
- A single-factor Design of Experiment for shutter speed optimization on four different surface conditions, represented by four different spheres, through the definition of the Score, evaluated from a set of performance metrics, and its interpolation via quadratic fitting (Chapter 3:).

The lack of dedicated standards for the acceptance and reverification test of handheld laser scanners forces the manufacturers to rely on procedures designed for other optical coordinate measuring systems (CMSs), such as the ISO 10360-13 and the withdrawn VDI/VDE 2634 part 3. ISO 10360-13 explicitly excludes handheld laser-lines type scanners from its scope, but allows for their application by mutual agreement between manufacturers and customers; this statement is the starting point for the first objective of this thesis.

As handheld line laser-based sensors cannot deliver static measurements, differently from the optical CMSs for which the standard was conceived, it was not possible to directly apply the measurements strategies presented in the standard and based on the concepts of Single View (SMV.SV) and Multiple View Sensor Measurement Volumes, and Concatenated Measurement

Volume (CMV.MV). The proposed strategies CMV.A, CMV.B and CMV.D aim to replicate these principles, while CMV.C is a newly introduced strategy:

- CMV.A constrains the movement of the sensor along a single translation direction, to replace SMV.SV;
- CMV.B is based on the registration and fusion of the CMV.A measurements acquired from different positions through the instrument's positioning and registration system, to replace SMV.MV;
- CMV.C instead involves a free and continuous scanning mode around the object, more representative of the common measurement practice with these instruments;
- CMV.D was developed as a practical implementation of the concatenated measuring volume (CMV.MV) required by the standard for the evaluation of volumetric length measurement error.

These strategies were therefore used in the measurement acquisition of calibrated artefacts with the HandySCAN SILVER, from which a set of errors was evaluated consistently with the ISO 10360-13. The obtained results showed a coherent behaviour across the scanning strategies: the values obtained from the CMV.B fusion are generally comparable with the worst CMV.A observed errors, confirming that the registration process does not introduce significant additional errors contributions. Furthermore, the CMV.C showed a general improvement in the form errors (probing form and flat-form distortion errors) evaluated with the 95th percentile filtering, while considering the 100% of points the improvement observed was much smaller, and could be related on the way the software constructs the mesh from which the point cloud was extracted. The comparison with the manufacturers specifications was limited to the errors for which reference values were available, and it revealed significant differences. The maximum observed errors are higher than the declared values, which can be explained by the more stringent experimental conditions adopted compared to factory testing. This confirms how the kinematic scanning strategy influences the instruments actual metrological performance, an aspect not covered by the manufacturers synthetic specifications.

To address the second objective, a single-factor Design of Experiment with ten different shutter speed levels was structured and performed independently on four surface conditions: a matte and a shiny metallic sphere, a glossy billiard ball, and the same sphere after the application of a spray matting coating. From the four performance metrics evaluated on each acquisition, i.e. the probing form and size errors with the 95th percentile filtering and the coverage and average point density metrics (estimated using the k-nearest-neighbours approach), the first three were combined into an aggregate index, the Score, using the Modified Digital Logic method.

For each surface, the Score vs shutter speed curve was interpolated with a quadratic fit, and an optimal shutter speed and an optimal shutter speed range; a preliminary validation of the results for each surface was performed through a Monte Carlo simulation. The results show clearly distinct behaviour between the metal and billiard surfaces. The metallic spheres exhibit a well-defined peak at 3.18 ms (matte surface) and 4.92 ms (shiny surface), and the Monte Carlo simulations confirms these peaks. On the other hand, the billiard spheres both indicate 0.10 ms (the minimum available value) as the best available operating point, but for two different reasons: a convex fit for the glossy sphere that consequentially does not show a peak, and a concave fit with a vertex outside the range for the mattified one. In both cases, the number of valid Monte Carlo simulations is low, and the individuated peak does not align with the optimal observed one. The mattifying spray, however, proved effective in the improvement of the performance metrics. It corrected the dimensional probing error, which is systematically negative on the glossy sphere due to specular reflection, bringing it back to values close to zero. It also made the coverage much more stable at extreme shutter speeds, which on the glossy sphere drops to 13% while on the matte one it remains above 35%.

The work presented in this thesis presented some limitations and challenges, which are discussed in the following together with possible future outlooks.

Regarding the performance verification campaign two methodological issues were encountered. The calibrated length used for the CMV.A distortion error, equal to 199.858 mm, does not fully meet the dimensional requirement set by adapting the standard, in the absence of a calibrated artefact of intermediate length compatible with the instruments measurement volume. When evaluating the probing errors using the CMV.A strategy the ball beam was not always positioned as required by the standard, but in some acquisitions the two spheres occupied inverted positions (voxels); to ensure a consistent identification of the calibrated sphere across the twelve positions, the probing errors evaluation was restricted to only sphere 20240409-01. This choice, however, prevented the characterization of voxel 3 with the CMV.A strategy, and the remaining voxels were evaluated with an uneven number of repetitions. A total of 132 individual measurements were performed, considering all the repetitions and scanning strategies and type of errors; these, despite being necessary to adapt the ISO 10360-13 to the dynamic behaviour of the scanner, are considerably more than the measurements suggested in the standard, and could be limiting from an industrial application standpoint, suggesting the need to identify in the future a representative subset of measurements. A further challenge arises from manual movement of the scanner during the measurements: on one side, this aspect brings the verification procedure closer to real operating practice; on the other hand, it introduces variability related to the operators ab ility to maintain a constant scanning speed and trajectory, less controllable than with a motorized or robotic system.

For the shutter speed experimental campaign, the main limitation is the quadratic fit adopted to interpolate the Score values. It was chosen for its simplicity and for allowing a direct analytical estimate of the optimum, but it does not always follow the experimental data closely, especially for the glossy and mattified billiard spheres, as shown by the Monte Carlo simulations. For the mattified billiard sphere, the first repetition at 0.15, 0.20, 0.30, 0.40, 2.00, 5.00 and 8.00 ms was identified as an outlier and excluded, reducing to four the repetitions available at the affected levels.

Building on the limitations discussed above, several directions for future work can be identified. For the performance verification campaign, a first step is completing the voxel 3 characterization through a dedicated campaign. A second step is reducing the number of required measurements, to make the protocol more practical for industrial use.

For the shutter speed optimization campaign, the Design of Experiment could be extended to a multi-factor design, including surface roughness, material colour, and working distance. Alternative fitting models, such as a higher-order polynomial, a spline-based fit, or a robust regression, could also be tested for the Score curve. A further step, common to both campaigns, is reducing the variability introduced by the manual movement of the scanner. The role of point density in the Score calculation also remains open: it was excluded in this work, but it could be informative for sensors with a variable-density output rather than a fixed-resolution mesh.

A particularly promising direction is the evolution of the MATLAB GUI developed in this work into a digital twin of the scanner. The GUI already implements the Score calculation, the quadratic fit, the Monte Carlo simulation, outlier filtering based on the interquartile range, and minimum coverage thresholds. These functionalities are the building blocks of a broader system. Such a system could, in principle, take the surface conditions detected during acquisition as input, and return a shutter speed recommendation in real time. This system should not aim at full closed-loop automation, without supervision. The quadratic fit adopted in this work does not always describe the experimental trend faithfully, and the variability between repetitions is in some cases high, as shown by the limited number of valid Monte Carlo simulations for some of the tested surfaces. The natural development is therefore a human-in-the-loop digital twin. The system provides a recommendation, based on historical data and the implemented statistical model. The operator validates the final shutter speed choice before acquisition, drawing on experience and specific knowledge of the part to be measured. This approach combines the systems ability to synthesize information quickly with human oversight of the final decision. This is a particularly relevant aspect in industrial contexts, where the consequences of a wrong shutter speed choice can directly affect inspection quality.

Finally, validating the proposed verification protocol on other multi-line handheld laser scanners available on the market would help assess the generalizability of the CMV.A, CMV.B, CMV.C, and CMV.D scanning strategies, beyond the specific instrument used in this thesis.

References

[1] VDI/VDE 2634 Part 3:2008 Optical 3D measuring systems - Multiple view systems based on area scanning, Verein Deutscher Ingenieure, Düsseldorf, n.d.

[2] ISO 10360-13:2021 Geometrical product specifications (GPS) — Acceptance and reverification tests for coordinate measuring systems (CMS) — Part 13: Optical 3D CMS, International Organization for Standardization, Geneva, n.d.

[3] JCGM 200:2012 International vocabulary of metrology — Basic and general concepts and associated terms (VIM), Joint Committee for Guides in Metrology, Sèvres, n.d.

[4] Bureau International des Poids et Mesures, Le Système International d'Unités (SI), Bureau International des Poids et Mesures, Sèvres, France, 2019.

[5] S. Catalucci, A. Thompson, S. Piano, D.T. Branson, R. Leach, Optical metrology for digital manufacturing: a review, Int. J. Adv. Manuf. Technol. 120 (2022) 4271–4290. https://doi.org/10.1007/s00170-022-09084-5.

[6] W. Hartmann, A. Weckenmann, B6.1 - Function-Oriented Dimensional Metrology – More than Determining Size and Shape, in: Proc. Sens. 2013, AMA Service GmbH, Von-Münchhausen-Str. 49, 31515 Wunstorf, Germany, Nürnberg, 2013: pp. 285–290. https://doi.org/10.5162/sensor2013/B6.1.

[7] L. De Chiffre, H.N. Hansen, J.L. Andreasen, E. Savio, S. Carmignato, Geometrical Metrology and Machine Testing, DTU, 2015.

[8] S. Catalucci, A. Thompson, J. Eastwood, Z.M. Zhang, D.T. Branson Iii, R. Leach, S. Piano, Smart optical coordinate and surface metrology, Meas. Sci. Technol. 34 (2023) 012001. https://doi.org/10.1088/1361-6501/ac9544.

[9] JCGM100-2008 Evaluation of measurement data — Guide to the expression of uncertainty in measurement, Joint Committee for Guides in Metrology, Sèvres, n.d.

[10] ISO 14253-3:2011 Geometrical product specifications (GPS) — Inspection by measurement of workpieces and measuring equipment — Part 3: Guidelines for achieving agreements on measurement uncertainty statements, Geneva, n.d.

[11] ISO 15530-3:2011, ISO (n.d.). https://www.iso.org/standard/53627.html (accessed May 2, 2026).

[12] ISO/TS 15530-4:2008 Geometrical Product Specifications (GPS) — Coordinate measuring machines (CMM): Technique for determining the uncertainty of measurement — Part 4: Evaluating task-specific measurement uncertainty using simulation, International Organization for Standardization, Geneva, n.d.

[13] Y. Liu, N. Pears, P.L. Rosin, P. Huber, eds., 3D Imaging, Analysis and Applications, Springer International Publishing, Cham, 2020. https://doi.org/10.1007/978-3-030-44070-1.

[14] R. Leach, Advances in Optical Form and Coordinate Metrology, IOP Publishing Ltd, 2020. https://doi.org/10.1088/978-0-7503-2524-0.

[15] S.M. Sze, K.K. Ng, Physics of semiconductor devices, 3rd ed, Wiley-Interscience, Hoboken, N.J, 2007.

[16] Y. Wang, H.-Y. Feng, Modeling outlier formation in scanning reflective surfaces using a laser stripe scanner, Measurement 57 (2014) 108–121. https://doi.org/10.1016/j.measurement.2014.08.010.

[17] N. Vukašinović, J. Duhovnik, Advanced CAD Modeling: Explicit, Parametric, Free-Form CAD and Re-engineering, Springer International Publishing, Cham, 2019. https://doi.org/10.1007/978-3-030-02399-7.

[18] Interactions at the surface - examples for light interactions of different materials, (n.d.). https://www.vision-doctor.com/en/lighting/ill-t3/interactions-at-surface.html (accessed September 3, 2026).

[19] F.E. Nicodemus, J.C. Richmond, J.J. Hsia, I.W. Ginsberg, T. Limperis, Geometrical considerations and nomenclature for reflectance, 0 ed., National Bureau of Standards, Gaithersburg, MD, 1977. https://doi.org/10.6028/NBS.MONO.160.

[20] Y. Wang, H.-Y. Feng, Modeling outlier formation in scanning reflective surfaces using a laser stripe scanner, Measurement 57 (2014) 108–121. https://doi.org/10.1016/j.measurement.2014.08.010.

[21] Z. Tao, Z. Hou, Y. Deng, D. Zhang, J. Qi, Quantitative evaluation of pyramid belt wear using light-reflection characteristic of agglomerate coating and image processing, Measurement 242 (2025) 116048. https://doi.org/10.1016/j.measurement.2024.116048.

[22] M. Raimundo, O. Gama, P. Santos, A. Pinto, S. Gomes, N. Silva, P. Monteiro, Identification of at Distance Materials Using Laser Signals and Deep Learning, Sensors 22 (2022) 7726. https://doi.org/10.3390/s22207726.

[23] S. Catalucci, T. Koutecký, N. Senin, S. Piano, Investigation on the effects of the application of a sublimating matte coating in optical coordinate measurement of additively manufactured parts, Int. J. Adv. Manuf. Technol. 140 (2025) 2749–2775. https://doi.org/10.1007/s00170-025-16378-x.

[24] D. Palousek, M. Omasta, D. Koutny, J. Bednar, T. Koutecky, F. Dokoupil, Effect of matte coating on 3D optical measurement accuracy, Opt. Mater. 40 (2015) 1–9. https://doi.org/10.1016/j.optmat.2014.11.020.

[25] D. Hruboš, T. Koutecký, D. Paloušek, An experimental study for determination of an application method and TiO2 powder to ensure the thinnest matte coating layer for 3D optical scanning, Measurement 136 (2019) 42–49. https://doi.org/10.1016/j.measurement.2018.12.058.

[26] D. Owczarek, K. Ostrowska, M. Jedynak, M. Krawczyk, A. Gąska, Evaluation of the influence of the surface dulling process on the result of optical coordinate measurement, Meas. Sens. 38 (2025) 101778. https://doi.org/10.1016/j.measen.2024.101778.

[27] ISO 14638:2015 Geometrical product specifications (GPS) — Matrix model, International Organization for Standardization, Geneva, n.d.

[28] ISO 10360-1:2001 Geometrical product specifications (GPS). Acceptance and reverification tests for coordinate measuring machines (CMM). Vocabulary, International Organization for Standardization, Geneva, Switzerland, n.d.

[29] ISO 10360-2:2009 Geometrical product specifications (GPS) — Acceptance and reverification tests for coordinate measuring machines (CMM) — Part 2: CMMs used for measuring linear dimensions, n.d.

[30] ISO 10360-8:2013 Geometrical product specifications (GPS) — Acceptance and reverification tests for coordinate measuring systems (CMS) — Part 8: CMMs with optical distance sensors, International Organization for Standardization, n.d.

[31] D.M. Fabris, P. Brambilla, C. Conese, M.M. Maspes, R. Sala, M. Tarabini, METROLOGICAL CHARACTERIZATION OF OPTICAL 3D COORDINATE MEASUREMENT SYSTEMS – COMPARISON OF ALTERNATIVE HARDWARE DESIGNS AS PER ISO 10360, Int. Arch. Photogramm. Remote Sens. Spat. Inf. Sci. XLVIII-2/W2-2022 (2022) 39–43. https://doi.org/10.5194/isprs-archives-XLVIII-2-W2-2022-39-2022.

[32] T.P. Kersten, H.-J. Przybilla, M. Lindstaedt, Investigations of the Geometrical Accuracy of Handheld 3D Scanning Systems, Photogramm. - Fernerkund. - Geoinformation 2016 (2016) 271–283. https://doi.org/10.1127/pfg/2016/0305.

[33] P. Kalinowski, J. Hindmarch, T. Luhmann, ACCURACY INVESTIGATIONS OF HAND-HELD SCANNING SYSTEMS USING DIFFERENT DUMBBELL ARTEFACTS, Int. Arch. Photogramm. Remote Sens. Spat. Inf. Sci. XLIII-B2-2022 (2022) 401–407. https://doi.org/10.5194/isprs-archives-XLIII-B2-2022-401-2022.

[34] O. Icasio-Hernández, A. Rocha De La Cruz, B. Muralikrishnan, V. Lee, W. Ren, J.-J. Gonzalez-Barbosa, VDI/VDE 2634-2 and ISO 10360-13 performance evaluation tests, and systematic errors in structured light systems, Precis. Eng. 88 (2024) 804–814. https://doi.org/10.1016/j.precisioneng.2024.04.015.

[35] M. Abe, From technical challenges pursued in development of performance evaluation of optical 3d CMS, Meas. Sens. 38 (2025) 101660. https://doi.org/10.1016/j.measen.2024.101660.

[36] W. Ameen, A. Al-Ahmari, S. Hammad Mian, Evaluation of Handheld Scanners for Automotive Applications, Appl. Sci. 8 (2018) 217. https://doi.org/10.3390/app8020217.

[37] V. Meana, P. Zapico, E. Cuesta, S. Giganto, S. Martinez-Pellitero, Laser Triangulation Sensors Performance in Scanning Different Materials and Finishes, Sensors 24 (2024) 2410. https://doi.org/10.3390/s24082410.

[38] creaform-adds-two-high-performance-scanners-handyscan-3d-silver-series, (n.d.). https://www.creaform3d.com/About-Us/Press-releases/creaform-adds-two-high-performance-scanners-handyscan-3d-silver-series (accessed September 3, 2026).

[39] ISO 1101:2017 Geometrical product specifications (GPS) — Geometrical tolerancing — Tolerances of form, orientation, location and run-out, International Organization for Standardization, Geneva, n.d.

[40] ISO 12781-1:2011 Geometrical product specifications (GPS) — Flatness — Part 1: Vocabulary and parameters of flatness, International Organization for Standardization, Geneva, n.d.

[41] ISO 12781-2:2011 Geometrical product specifications (GPS) — Flatness — Part 2: Specification operators, International Organization for Standardization, n.d.

[42] B. Dehghan-Manshadi, H. Mahmudi, A. Abedian, R. Mahmudi, A novel method for materials selection in mechanical design: Combination of non-linear normalization and a modified digital logic method, Mater. Des. 28 (2007) 8–15. https://doi.org/10.1016/j.matdes.2005.06.023.